GROUND MOTION SCALING IN ITALY AND GERMANY

Luca Malagnini, Dottore in Fisica

A Digest Submitted to the Faculty of the Graduate School
of Saint Louis University in Partial Fulfillment of
the Requirements for the Degree of
Doctor of Philosophy

1999

Digest

Ground motion scaling relationships at regional distances along peninsular Italy and Germany are quantified by performing regressions over two large datasets of broadband seismograms. The Italian dataset consists of 3000 three-component seismograms, collected for 446 events that occurred along the Apennines, whereas 1350 three-component recordings were obtained for 222 events (earthquakes and chemical explosions) recorded by the German Regional Seismic Network.

Logarithms of observed ground motion amplitudes (either peak values of bandpass filtered time histories, or Fourier spectral components), are modeled as the summation of excitation, site, and propagation terms. They represent, respectively, the excitation of the ground motion at a reference distance, the distortion due to the shallow geology at the recording sites, and the effects of the geometrical spreading and anelastic attenuation. The attenuation functional is modeled as a piece-wise linear function with several nodes. Regressions are independently carried out over the mentioned terms, at a discrete set of sampling frequencies.

Regression results for the attenuation functional are very similar to the ones obtained by using a simpler coda normalization technique. In a subsequent step, the empirical estimate of the functional is parameterized using a geometrical spreading function, a frequency-dependent Q, and a distance-dependent duration for the seismic signals. Random vibration theory (RVT) is used to create a predictive model.

Results are generally given in the (0.25-5.0 Hz) frequency band, although a small subset of data was available in Italy to confirm our results in the broader (0.5-16 Hz) frequency band. Results support the idea of a low-Q crust in the Apennines ($Q(f) = 130\,f^{0.10}$), implying that seismic hazard along the Apennines should be dominated by the local seismicity. Higher values of crustal Q are found in Germany, in the 0.5-16.0 Hz frequency range ($Q(f) = 400\,f^{0.42}$). The different geometrical spreading functions may reflect variations in the Moho depths between the two regions.

GROUND MOTION SCALING IN ITALY AND GERMANY

Luca Malagnini, Dottore in Fisica

A Dissertation Submitted to the Faculty of the Graduate School
of Saint Louis University in Partial Fulfillment of
the Requirements for the Degree of
Doctor of Philosophy

1999

COMMITTEE IN CHARGE OF CANDIDACY:

Professor Robert B. Herrmann,
       Chairperson and Advisor

Associate Professor Charles J. Ammon

Professor Brian J. Mitchell

Professor David J. Crossley

i

Acknowledgments

I dedicate this dissertation to my parents, who always supported and encouraged me in all the difficult and happy moments of my life. They have always been a bright example for me.

I want to thank the committee of candidacy for the help provided throughout this effort; A special recognition goes to my advisor, Robert B. Herrmann, for his friendship, his availability, the help he gave me on all the theoretical and practical issues, and for his always valuable suggestions. Charles J. Ammon also deserves a special recognition for the fruitful discussions we had in the last three years. His friendship was very important to me. Thanks to Brian J. Mitchell for his thorough review of the manuscript.

Thanks to Massimo Di Bona, who organized the Italian datasets and always had thoughtful comments on my work, and to Karl Koch, who carefully selected the German dataset: their contribution to this effort was very important. Thanks to Barbara Palombo for helping me so much in many situations.

Roberto Ortega was a constant source of humor, sometimes unintentional; without him it would have been much harder. Thanks to Sean-Thomas Morrissey for his quiet friendship, and for helping me so much when I arrived in St. Louis. Thanks to Enzo Boschi and to Antonio Rovelli for the support I had from them in the last three years, and from the *Istituto Nazionale di Geofisica*, the institution they represent.

I also want to thank all my other friends, in America as well as in Europe, and my brothers, just for being there. Their contribution to this effort was really important, even though they didn't do anything.

Finally, I am deeply thankful to Aybige Akinci for the support, help and affection she gave me in the last two years of my doctorate.

Table of Contents

List of Tables

List of Figures

xxii

1. Introduction

1.1 Objective

The focus of this study is on the quantitative description of the regional attenuation of the earthquake-induced ground motion in two regions of Europe: the Apennines (Italy) and Germany. This information is needed to obtain the so-called regional predictive relationships, used to quantify the ground motion expected at a certain site, given the location (distance) and size of the seismic source.

Once we create the ability to predict the ground motion anywhere in a certain region, a further step can be taken by integrating this information with some probabilistic considerations on the regional seismicity. This then leads, after merging historical and instrumental seismological catalogs, to the quantification of the distribution of the seismic hazard within the region.

A precise definition of the seismic hazard will be given in the following subsection; however, we intuitively understand that an advanced hazard map of a seismically active country is a very important achievement. Our contribution to this goal, for the moment, is in the reevaluation of the regional ground motion scaling relationships.

The definition of an empirical (and functional) form to describe the attenuation of seismic waves at regional distance finds other applications, besides seismic hazard assessment. Since the ground motion recorded at the free surface at a certain site is the result of the interaction between the

source excitation function and the path, site and instrument responses, the quantification and correction of the last three is needed to obtain undistorted source spectra to be used for specific source studies, and for the development of discrimination methods to exclude explosions from the earthquake population. The spectral correction is also needed to properly estimate the yield of a chemical, or nuclear, explosion.

1.2   The Assessment of Seismic Hazard

The assessment of seismic hazard is a very important issue in our research, and it is probably the most important contribution of seismology to our society. Seismic hazard is determined by the following three factors:

- the distribution, in time, space and size, of the regional seismicity;

- the attenuation of the seismic waves at increasing distances from the location of the earthquake;

- the action of the shallow geology in the distortion of the seismic signal

Given a quantitative description of these factors, we can produce a numerical evaluation of the distribution of the seismic hazard throughout a region.

The hazard of a site can be estimated in two different ways: by using a Probabilistic Seismic Hazard Analysis (PSHA, see Appendix A), or a Deterministic Seismic Hazard Analysis (DSHA, see Appendix B). The quantification of the hazard obtained with a PSHA is given by the probability

of exceedance, at the site of interest, of a parameter describing the seismic-induced ground motion (the Peak Horizontal Acceleration, for example - PHA), either *per annum* or in a specified period of time (a typical time window can be 50 years). To compute this probability, seismologists use two different tools, one calibrated over the region of interest and the other over the seismogenic zone(s). The first one, the so-called predictive relationship, is needed in order to predict the seismic-induced ground motion as a function of frequency, magnitude of the earthquake and epicentral distance.

A predictive relationship can be split in two distinct parts: a spectral model for the source, and a path term. The latter is the focus of this dissertation; it will take into account the effect of crustal structure on the seismic waves. Local perturbations to the predicted spectra, however, are also expected, due to the distortion induced by the shallow geology on the incoming waves. For this reason, predictive relationships need to be locally integrated by special terms that take into account these effects. The average site term, computed over a truly heterogeneous set made of all the available sites in a broad region, is likely to be zero. On the other hand, we sometimes face a situation in which the whole region shares a common, shallow geological environment. In this case, by forcing the average site effect to be null, we can bias our hazard estimates significantly.

The second tool is the recurrence law. It is used to compute the probability of annual exceedance of a given magnitude in a certain source zone. The recurrence law is generally well described at all magnitudes by the Gutenberg-Richter relationship. If discrepancies are found at high magnitudes in the recurrence law determined by using the seimological informa-

tion and the geological record, we can choose the characteristic earthquake model in order to estimate the maximum expected magnitude in the seismogenic area.

The recurrence law will be calibrated over the specific seismogenic zone(s) that can potentially affect our region of interest. It gives the number of events expected to exceed a given magnitude *per annum* for each source zone. If more than one seismogenic area is active in the region, each of them will need a calibrated recurrence relationship, since different zones may have different activity rates. Of course, the seismogenic zones must be precisely characterized in a previous stage, in terms of the spatial distribution of the seismicity and of the expected upper level for the magnitude range.

The seismic hazard can also be defined in a deterministic way, for example as the largest peak ground motion expected in a certain area. For a deterministic calculation we only need the estimate of the maximum magnitude expected in the region and the predictive relationships. The DSHA gives the most conservative estimate of the hazard, and it should be used to design critical facilities, like nuclear power plants.

1.3 Predicting Ground Motion

The prediction of seismic-induced ground motion has always been of primary interest for seismologists and structural engineers. One way to approach this prediction would be to examine every single ripple that is generated by an earthquake; the match in shape and amplitude of every single pulse in the seismograms can be done by using suitable mathe-

matical models for the seismic radiation at the source, and for the wave propagation through the medium. This point of view is very important in seismology, since it allows us to obtain important information about the source mechanics, location, geometry and size, as well as a quantitative description of the medium through which the energy propagates. Although the waveform modeling approach is widely and successfully used in global, long period seismology, and even at regional distances, a different approach must be used to describe the high-frequency ground motion at a short distance from the source, since the complexity of the physical system (i.e. the rupturing fault) goes beyond a critical level. Similar changes in point of view are very common in many branches of physics: for example, in the case of the kinetic theory of gases, the effect of an overwhelming number of mutual interactions occurring between the gas molecules and between the molecules and the confining walls is described, in a statistical sense, by macroscopic parameters (P, V, T) that completely characterize the system. In treating accelerograms we face a similar situation, and a statistical approach to the problem is needed. Instead of trying to reproduce the details of ground acceleration in the time domain, we use a suitable source model and our empirical scaling laws to prognosticate its spectral shape and amplitudes. Peak values in the time domain are predicted by exploiting the stochastic nature of the accelerograms. Our final product will be a map of either the probability of exceedance for a certain peak motion within a certain time window, or the maximum expected ground motion.

In our discussions we generally talk about ground acceleration, since it dominates both the high-frequency part of the seismic spectrum and the

behavior of most human-made structures. Engineers are also interested in ground velocity spectra, in order to study the intermediate-frequency seismic response of large objects (long bridges, tall buildings, etc.); they are generally much less interested in the characteristics of ground motion displacement, which dominates the low-frequency part of the seismic spectrum.

The complex aspect of ground-structure coupling is addressed by engineers on the basis of a set of ground motion parameters provided by seismologists. A simplistic, but still useful, description of the mechanical behavior of structures coupled with the ground at a specific site can be described in terms of the peak velocity response of slightly damped, single-degree-of-freedom oscillators (the pseudovelocity response spectrum).

The point of view that I just described, essentially represents the way engineers want seismologists to talk about the ground motion induced by an earthquake. Structural engineers need to know how to characterize the ground acceleration during an earthquake of a specified magnitude in a given area located at a given distance from the source, and within a predetermined time period, the length of which is linked to the projected lifetime of the particular structure. Structural engineers want estimates of the peak values for the ground acceleration, of its duration in time, and of its decay rate at increasing distances from the source. They want general relationships to link the ground acceleration to the earthquake magnitude, the distance from the fault, and the frequency, together with a reasonable estimate of the maximum magnitude that we should expect in the area of interest during the specific time window. By answering these needs in a complete and simple fashion, we build the necessary interface between

seismologists and structural engineers.

A precise evaluation of the duration of the ground motion at a specific site is extremely important for engineering purposes, since severe non-linear behavior is triggered in loose, water-saturated sediments at a relatively low level of peak ground motion (down to 0.1 g, see Kramer, 1996) by exceeding some critical value of duration.

Duration is a function of the fault size (the duration of the rupture) and of the dispersion that elastic waves experience along source-receiver paths. Scattering also contributes to the increase in duration at increasing distances from the source. Dispersion redistributes in time the frequency content of the radiated spectrum in a way that is deterministically predictable in theory if the structure of the medium is known. On the other hand, scattering redistributes the seismic energy in space and time, behind the wavefronts, during a stochastic process that is treated in a statistical fashion, even with diffusion equations if the scattering is strong enough. Again, we can see a clear analogy with the kinetic theory of gases, since mean free paths can be defined also for the elastic waves scattered through the Earth, as well as for the gas molecules confined at a certain pressure and temperature (Aki and Chouet, 1975; Wu, 1985; Hoshiba, 1991).

After giving a quantitative prediction of the characteristics of the earthquake-induced ground motion, we can proceed to a complete seismic hazard assessment. We do so by estimating the probability of exceedance of a specified peak ground motion *per annum*, or by estimating the largest expected peak ground acceleration. Both predictions will be given as a function of position.

To perform a PSHA, besides the predictive relationships, we need an

estimate of the likelihood of occurrence *per annum* for an earthquake of magnitude $M > m_0$, capable of exceeding the threshold peak ground motion. We want to integrate our distribution from m_0 up to an estimate of the maximum expected magnitude, m_{max}. The integration will be performed for each seismogenic zone also in the spatial domain (along r, the distance from the source), and the results obtained from different seismogenic zones will be summed together at each frequency, for each source-site distance bin. Kramer (1996) suggests five possible choices for the spatial variable r: i) the distance from the epicenter, ii) the distance from the hypocenter, iii) the distance from the zone of highest moment release, iv) the minimum distance from the fault, and, v) the minimum distance from the surface projection of the fault area. Definitions i) and v) are by far the most widely used; Kramer (1996) also mentioned that choice v) gives more stable results, and at the same time is more conservative.

If the historical record is sufficiently long and complete, the limits of integration that we need to use are relatively easy to define with respect to spatial and magnitude coordinates. Also, before integrating, we need to properly normalize the spatial distribution of the seismicity. By analyzing a long, complete dataset, we also have the opportunity to decide whether to use the Gutenberg-Richter law, or the characteristic earthquake model, in order to give the activity rate at the highest magnitude level for each seismogenic zone. The largest magnitude for a specific seismogenic area can be determined by studies in palaeoseismology.

At the end of the whole process, if we are interested in the peak ground acceleration, we will have a table of probabilities of exceedance of the specified peak ground acceleration (for example, 0.1 g) for each frequency and

site, either *per annum*, or within a given time window (generally 50 years). Each probability will take into account all the contributions given by different seismogenic areas. Alternatively, we can give the value of acceleration expected to be exceeded with a fixed probability in a given time window (for example: for a fixed level of likelihood of 2% in 50 years, we expect the peak ground acceleration to exceed 0.4 g at a certain site, but only 0.04 g at a safer location). The final product of both a PSHA or a DSHA will be a hazard map. The USGS computes maps of acceleration with a probability of exceedance of 10%, 5% and 2% in 50 years, corresponding to earthquake return periods of 475, 950 and 2375 years, respectively.

Because of obvious economical reasons, we want critical structures to be safer than residential buildings, as long as people do not get killed in their homes. But the definition of a critical structure in a land with a long history may differ from that for a relatively young country. Nuclear reactors, hospitals or dams are certainly critical facilities wherever we put them. Power plants, communication and transportation networks, bridges, critical govermental offices and defense facilities are more examples of critical structures, as well as the industrial areas of strategic importance for the economy of the region. In essence, the economical and environmental impact of the earthquake must be taken into account. Some historical monuments also need a special treatment (for example the Colosseum in Rome and the Church of Saint Francis in Assisi, both of which were badly damaged by earthquakes in historical and very recent times, respectively). Even though the results of a DSHA at these special locations should be preferred to a PSHA, the way we want to treat critical buildings versus ordinary houses in a PSHA is by choosing a lower probability of

exceedance in defining the construction or strengthening requirements in the building codes. All these issues reflect the need for some level of subjective evaluation of the impact of the earthquake that are beyond the sole discretion of seismologists and engineers.

A big difference between a Mediterranean country (Italy, for example) and the US concerns the construction characteristics for housing. In Italy, the bulk of the population in small historical cities live in buildings which were not designed to withstand any specific ground shaking. On the other hand, the number of earthquake-proof buildings in the US is comparatively very high. Nevertheless, a lot can be done to strengthen historical constructions, to protect people and, at the same time, to preserve history and art.

The process of finely calibrating earthquake hazard is critical. Even though the consequences of a severe, and even moderate underestimate of hazard are obvious, hazard evaluations that are too conservative give rise to serious problems, leading to excessively expensive and possibly unaffordable construction requirements.

It is now clear that priorities need to be defined everywhere, in the US as well as in Europe, with the help of detailed hazard maps. One of the goals of seismologists is to provide these maps; engineers are expected to translate the seismic hazard into building codes. Local and central (federal) governments are expected to define priorities.

1.3.1 Quantitative Modeling

The far-field spectral characteristics of the ground motion can be predicted by using available spectral models for the earthquake source and

for earthquake spectral scaling (see Brune, 1970, 1971; Boore, 1983, 1986; Atkinson and Boore, 1995, 1998; Atkinson and Silva, 1997; Boore and Joyner, 1997). Spectral amplitudes can then be propagated to different distances by using the regional scaling relationships.

A statistical tool, called Random Vibration Theory (RVT, see Chapter 2), developed by Cartwright and Longuet-Higgins (1956) to treat a random time series of tide levels, allows us to estimate the peak ground acceleration at a site, given its Fourier spectral amplitude (see Appendix C) and its duration in time. Estimates of the duration of the signals as a function of distance from the source can be obtained empirically from the data, providing an unambiguous definition of the duration itself.

In order to give a definition of the duration of the ground motion, Atkinson and Boore (1995): i) specified an earthquake model; ii) specified the geometrical spreading and the anelastic attenuation; iii) found the duration that matches the peak ground motion, for each time history (i.e. for each distance); iv) plotted the obtained duration-distance pairs to find a functional form to describe their distribution.

Raoof et al., (1998) used the duration of the time window that contained the 5% - 75% fraction of the seismic energy that follows the S-waves. This window was chosen since the peak motion in it was related to the Fourier spectrum within the window through RVT. This definition is preferred to that of Atkinson and Boore (1995) since it is based solely on observed data without using a theoretical predictive model.

The quantitative definition of the duration of the seismic signals has very important, practical implications. Since studies of ground motion scaling require a very large number of time histories, we need to develop

fully automated procedures that include proper signal windowing in the time domain.

1.3.2 Predictive Relationships

A regression on a set of data containing the peak values of the ground motion at many different source-receiver distances will provide the regional ground motion scaling for that specific physical quantity. The same process can be carried out to obtain the ground motion scaling of the Fourier amplitudes at a discrete set of sampling frequencies.

Predictive relationships are obtained by multiplying the theoretical spectra at different magnitudes, computed at short distance from the fault, with the empirical estimate of the regional scaling function. They will provide the expected spectra of the ground motion as a function of distance and magnitude (in the proper distance and magnitude ranges of engineering interest). Given a quantitative description of the duration of seismic signals as a function of distance, the use of the RVT will then allow the computation of the predictive relationships for the peak ground motion. The process can be carried out for each frequency separately for the whole band of engineering interest.

Once we provide an estimate of the duration of the significant seismic signal as a function of the distance from the source, and a suitable set of parameters for the earthquake model, another way to proceed would be to make use of the RVT to produce synthetic time histories that reflect the characteristics of the actual ground motion in the area. By averaging over many pseudo-random acceleration waveforms, we obtain the statistical parameters of the distribution of the peak acceleration as a function of

frequency, magnitude and distance from the fault. An additional term will describe the spectral distortion induced by the shallow geology.

Given the coefficients of the regional predictive relationships, we will also be able to estimate the minimum magnitude, m_0, capable of exceeding a given threshold of peak ground motion at a given site.

Previous observations tell us that (Kramer, 1996):

- peak values of strong ground motion are approximately lognormally distributed (i.e. the logarithm of the parameter is normally distributed);

- earthquake magnitude is proportional to peak values;

- most common geometrical spreadings are: $(1/r; \ 1/\sqrt{r})$;

- the area of the fault rupture increases with the magnitude of the event: the ground motion is partially produced by waves generated at distance r, partially at larger distances because of fault dimensions. The effective distance will then be greater than r;

- the material damping decreases the ground motion amplitudes exponentially with r;

- source and site parameters can strongly affect the ground motion.

On the basis of the aforementioned observations, we expect a general predictive relationship to have the following form:

$$\ln A = C_1 + C_2 M + C_3 M^{C_4} + C_5 \ln\left[r + C_6 \exp(C_7 M)\right] + C_8 r + f(source) + f(site)$$

where A is the peak or spectral value; C_i are the coefficients of the predictive relation; r is the distance from the seismogenic area; M is the magnitude of the earthquake; $f(source)$ and $f(site)$ take into account the source spectral characteristics and the effects on the ground motion due to the shallow geology at the recording site, respectively.

If $\sigma_{\ln A}$ is the standard deviation associated with the distribution of $\ln A$, the probability at a given magnitude $M = m$ that the ground motion will exceed a value A^* will be:

$$P(A > A^* | M = m) = 1 - F_Z(z^*)$$

$F_Z(z^*)$ is the value of the standard cumulative distribution function at:

$$z^* = \frac{(\ln A^* - \ln A)}{\sigma_{\ln A}}$$

(Kramer, 1996).

2. Approach to the Problem

2.1 Introduction

In the previous chapter we discussed the importance of a precise definition of the functional that describes the regional attenuation of the earthquake-induced ground motion. We will now see how to quantify this concept.

What is generally available for the seismological research are time series of ground velocity recorded by a number of different seismometric stations during earthquakes charaterized by different sizes and locations. Ground acceleration time series are very useful for the ground motion studies, although less common than velocity recordings, since accelerograms are generally recorded during large events. As an example, for this dissertation we will use just a few tens of three-component acceleration time histories, recorded in the Umbria-Marche region (Central Apennines) during two events of magnitude $M_w = 5.7$ and $M_w = 6.0$. The accelerograms will be used to integrate a dataset of more than 3,000 three-component seismograms recorded along the Apennines, in order to provide information at a magnitude level higher than that of the background seismicity.

For what follows, we will assume that each time series represents the actual ground motion (velocity), retrieved from the original data by carefully removing the distortion introduced by the recording system. Removing the instrument response is a very delicate step in most seismological

studies, especially in studies on ground motion scaling, but we will not describe the details of this stage of the data processing in this context.

As discussed in Chapter 3, we sometimes need to merge sets of data collected during different experiments, carried out in areas that we assume to be representative of a "homogeneous" larger region. This was the case of the Apennines, where data recorded by five independent seismic networks operating along the mountain belt were assumed to sample different portions of a regionally homogeneous crustal structure. The data from the different networks were merged together in a large, regional set that was used for investigating the ground motion scaling.

The action of merging separate datasets is very delicate, since the final results of a regression are biased by the average behavior of the network. A large regional network of permanent stations can average out differences in the crustal structure that exist within the covered region, better than a set of portable networks (i.e. a single, itinerant portable network), for the same number of seismograms.

The quantities of engineering interest that characterize each time series are:

- the Fourier spectrum;

- the distance from the source;

- the peak amplitude;

- the duration of the significant part of the earthquake-induced ground motion.

In what follows, we will use a phenomenological model in order to describe the attenuation of the ground motion peaks at a discrete set of frequencies, as a function of frequency and hypocentral distance. This functional form will rely on a very small set of parameters, and will be of easy practical use for the engineering community.

2.2 Filtered Time Series

We can relate the time-domain integral of the square of a time series to the frequency-domain integral of the square of its Fourier amplitude spectrum, via the Parseval's equality:

$$\int_{-\infty}^{+\infty} |a(t)|^2 dt = \int_{-\infty}^{+\infty} |\hat{a}(f)|^2 df$$

Given this result, we can relate the RMS value of a windowed time series to its Fourier spectrum:

$$a_{RMS} = \sqrt{\frac{\int_0^T |a(t)|^2 dt}{T}} \approx \sqrt{\frac{\int_{-\infty}^{+\infty} |\hat{a}(f)|^2 df}{T}}$$

This relationship will be used with the results of Random Vibration Theory; the approximation sign is used in the formula above because we did not take into account the distortion of the seismic spectrum due to time domain windowing. In practical applications, however, we compute the Fourier spectrum over the same, finite time window, $(0, T)$, and for this reason the equal sign could be used.

If the amplitude spectrum of the time series is nonzero only within a certain frequency window, say between f_1 and f_2 then

$$\sqrt{\int_{-\infty}^{+\infty} |a(t)|^2 dt} = \sqrt{2 \int_{f_1}^{f_2} |\hat{a}(f)|^2 df}$$

Finally, for a windowed time series that has been narrowly bandpass filtered between f_1 and f_2 (for which $(0, T)$ is the time window where $a(t)$ is significantly different from zero):

$$\sqrt{\frac{\int_0^T |a(t)|^2 dt}{T}} \approx \sqrt{\frac{2 \int_{f_1}^{f_2} |\hat{a}(f)|^2 df}{T}}$$

2.2.1 Duration of Ground Motion and Characteristics of the Bandpass Filters

The following are the specifications for the characteristics of the bandpass filters used throughout this work: each consists of a lowpass 8-pole Butterworth filter with corner frequency at $\left(f_0/\sqrt{2}\right)$ Hz, followed by a 8-pole highpass Butterworth filter with corner frequency at $\sqrt{2}f_0$ Hz.

Figure 2.1 describes the process chosen to automatically compute the duration of a seismic signal. It also describes our definition of the duration itself. The figure is relative to a seismogram recorded in southern Italy on October 10, 1996; the waveform is bandpass filtered around a central frequency $f_0 = 1.0$ Hz.

The filtered seismogram is squared and integrated, starting from the onset of the S-waves. At the time when the integral reaches a plateau, the integrated energy is normalized to unit value. The duration of the significant part of the seismogram, T, relative to the central frequency, f_0, is then defined as the time window bracketing the $5\% - 75\%$ of the integrated energy. Duration is referred to the portion of the time series that follows the S-wave onset.

In the next paragraph we will describe Random Vibration Theory, a tool that can be used to connect the peak value of a time series to the RMS
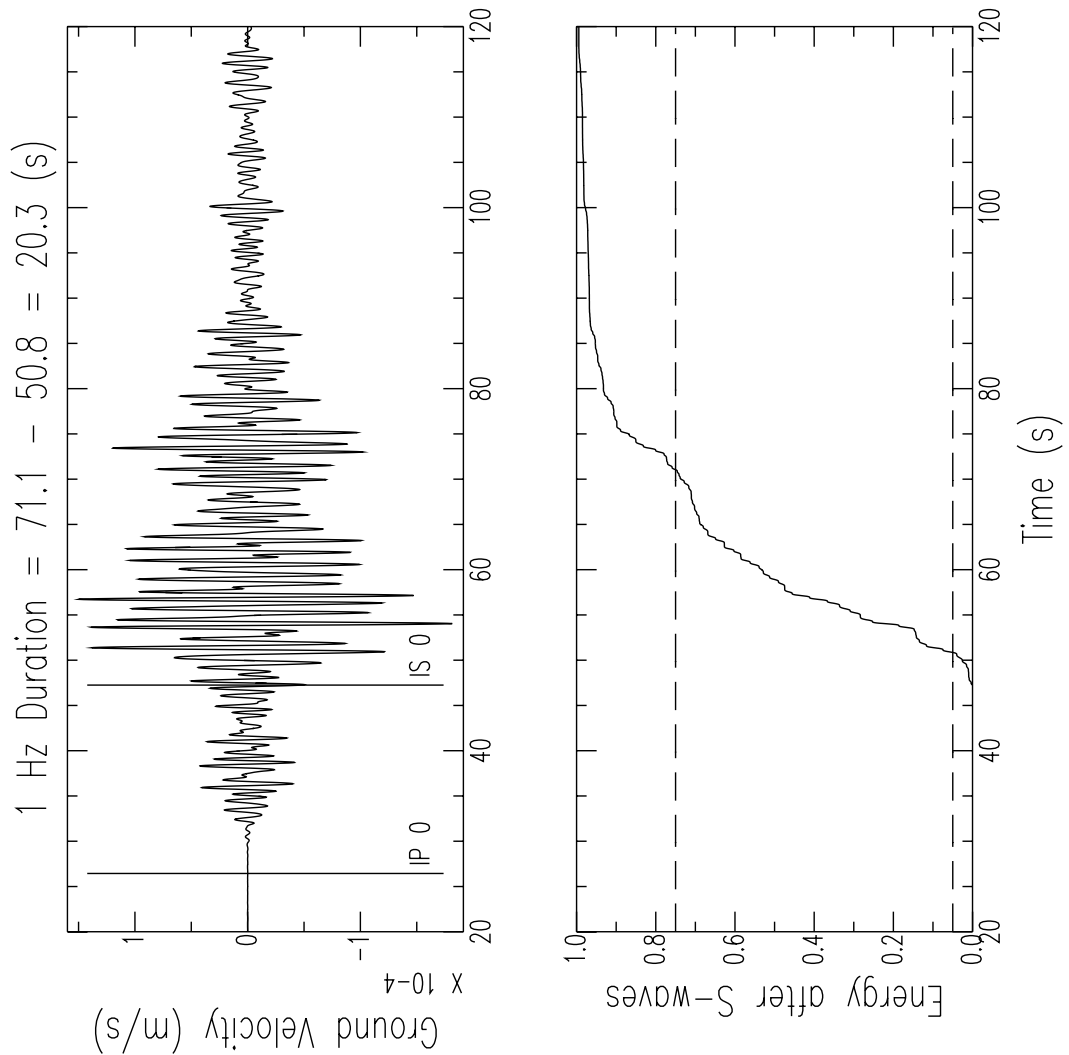
Figure 2.1: The plot describes how the procedure for the automatic computation of the duration of the significant portion of the ground motion works. The example shown in this picture is from an event recorded in southern Italy on October 10, 1996. The waveform has been bandpass filtered around a central frequency $f_c = 1$ Hz, by using a 8-pole highpass Butterworth filter with a corner at 0.707 Hz, followed by a lowpass, 8-pole Butterworth filter with a corner at 1.414 Hz. The energy (the squared velocity) following the onset of the S-waves is integrated and the time when it reaches a plateau is computed. The integrated energy is then normalized to the energy level at the plateau, and the times when it reaches the 5% and the 75% of that value are computed (indicated by the dashed lines in the lower frame) are the two levels of normalized energy). The time window of length T that is limited by these two times is defined as the duration of the specific seismogram at the frequency of 1 Hz.

average of its Fourier amplitude spectrum through duration.

The convolution theorem can be used on the Fourier spectrum of a seismogram to separate the contribution of source, crustal propagation and site; we now assume that an equivalent equation can be written also for the logarithm of the peak value of a seismogram that has been bandpass filtered narrowly around f_0:

$$PEAK(f_0) = SRC(f_0) + D(r, f_0) + SITE(f_0)$$

The action of a multiple-frequency bandpass filter is the key for exploiting such a convenient relationship in a very effective way. If a set of central frequencies is chosen for a multiple bandpass filtering action, a linear relationship like the one given above can be written for the peak amplitude of each seismogram, for each filtering frequency, given the duration of each filtered signal. We will have then a large system of linear equations that can be inverted for source, site and attenuation terms.

2.2.2   Random Vibration Theory (RVT) Equations

Given the RMS value of a windowed random time history, its peak value is a function of the number of maxima present in the time window (Cartwright and Longuet-Higgins, 1956). Using the Parseval's theorem, we can obtain the RMS value of a windowed time function from its squared spectral amplitude. If the time series is characterized by a dominant frequency (i.e., if the signal is filtered in a narrow frequency band centered at a particular frequency f_0), the number of peaks in the time history, N, is two times the duration T times the central frequency:

$$N = 2f_0 T$$

Cartwright and Longuet-Higgins (1956) demonstrated that:

$$a_{peak} = \eta_{max} a_{RMS}$$

where:

$$\eta_{max} = \int_{-\infty}^{+\infty} \eta \frac{d}{d\eta} \left[1 - q(\eta)\right]^N d\eta$$

$q(\eta)$ is the cumulative probability of η exceeding a given value; η_{max} is the expected peak value for the time history. In general, N depends on the spectral moments, as well as does the probability distribution of the peaks:

$$p(\eta) = \frac{d}{d\eta} \left[1 - q(\eta)\right]^N$$

The k-th spectral moment can be written as:

$$m_k = \frac{1}{\pi} \int_0^{\infty} \omega^k \left|A(\omega)\right|^2 d\omega$$

The spectral moments can also be used to estimate the dominant frequency of a time history and consequently N, the number of extrema (Cartwright and Longuet-Higgins, 1956):

$$f_0 = \frac{1}{2\pi} \left(m_4/m_2\right)^{\frac{1}{2}}$$

$$N = 2T \frac{1}{2\pi} \left(m_4/m_2\right)^{\frac{1}{2}}$$

Also, note that:

$$a_{RMS} = \left(\frac{m_0}{T}\right)^{\frac{1}{2}}$$

2.3 Fourier Amplitude Spectra

Each time a bandpass filter is applied, the duration T relative to that specific central frequency is evaluated. The Fourier spectrum is then computed on the original seismogram, on a time window of length T, starting at the onset of the S-waves. The RMS average of the spectral amplitude is computed within the frequency band bracketed by the two corner frequencies of the bandpass filter. At this point the RVT can be used to compute a prediction of the peak value, to be compared to the observed peak of the filtered seismogram. This check is done for understanding whether or not the duration has been properly evaluated in each case.

Excessive values of duration are computed when the noise characteristics prevent the energy integral to reach a stable plateau. This phenomenon is most common at low frequencies (well below 1 Hz), due to the presence of the microseisms.

The RMS average of the Fourier amplitude spectrum that is logarithmically centered at the frequency f_0 is used as our observed spectral amplitude at that frequency:

$$O(f) = \log \left[\sqrt{\frac{2 \int_{f_1}^{f_2} |\hat{a}(f)|^2 df}{f_1 - f_2}} \right]$$

$$O(f) = SRC(f) + D(r, f) + SITE(f)$$

In the equation above: $f_1 = f_0/\sqrt{2}$; $f_2 = \sqrt{2} f_0$.

2.4 Regressions

A general form for a predictive relationship is the following:

$$\log A(M, r, f) = SOURCE(M, f) + D(r, f) + SITE(f)$$

We use this relationship to describe all our observations, and invert the resulting linear system to obtain source, path (attenuation) and site terms. $D(r, f)$ contains both the geometrical spreading and the anelastic attenuation experienced by the seismic waves all along their paths:

$$D(r, f) = \log\left[g(r)\exp(-\pi\kappa_0 f)\exp(-\pi f r/Q(f)V)\right]$$

Researchers often pre-define $g(r)$ on the basis of considerations about the crustal structure of the region of interest: Atkinson (1993) used a trilinear geometrical spreading. The approach used here is the one described by Raoof et al. (1999), who used a piece-wise continuous function to describe the path term, $D(r, f)$, in their regressions. They chose a set of distance bins, assumed a linear interpolation between the fixed distance points, and inverted for the values of the function $D(r, f)$ at each transition distance. This approach does not require any *a priori* assumption on the functional form of the geometrical spreading, and allows a more detailed description of it, especially in the transitional zone between body- (r^{-1}) and surface-wave ($r^{-1/2}$) behavior. At a later stage of the processing, an appropriate functional form for the geometrical spreading and the anelasticity parameters can be inferred by a trial-and-error procedure. The parameter κ_0 was defined by Anderson and Hough (1984).

Following Yazd (1993), we describe $D(r, f)$ with a piecewise continuous function:

$$D(r, f) = \sum_{j=1}^{n} L_j(r) D_j(f)$$

where $L_j(r)$ is defined as

$$L_j(r) = \frac{r - r_{j-1}}{r_j - r_{j-1}} \quad if \ \ r_{j-1} \le r \le r_j \ \text{ and } \ j = 2, 3, ..., n$$

$$L_j(r) = \frac{r_{j+1} - r}{r_{j+1} - r_j} \quad if \ \ r_j \le r \le r_{j+1} \ \text{ and } \ j = 1, 2, ..., n - 1$$

$$L_j(r) = 0 \ , \quad \text{otherwise}$$

$D_j(f)$ are node values such that $D(r_j, f) = D_j(f)$; the m coefficients $D_j(f)$ are determined by the inversion. A smoothness constraint can be applied to $D(r, f)$ by requiring:

$$D_{j-1}(f) - 2D_j(f) + D_{j+1}(f) = 0$$

If the spatial sampling provided by the set of $\{r_j\}$ were even, the equation above would have described a minimum roughness constraint, where the second derivative of the model is kept small.

2.4.1 Effects due to the Shallow Geology:

It is well known that the local geology can substantially distort the seismic spectra. Since we focus our attention on the regional attenuation terms, spurious effects due to the site conditions should be properly evaluated.

Numerous studies have been published on the effect of the local geology on the ground motion, specifically on the amplification phenomena induced by the presence of sedimentary coverages (Wood, 1908; Kanai, 1952; Gutenberg, 1957; Idriss and Seed, 1968; Seed and Idriss, 1969; Borcherdt, 1970; Trifunac and Brady, 1975, 1976; Johnson and Silva, 1981; Sanchez-Sesma, 1985; Bard and Bouchon, 1985; Moczo and Bard, 1993). Nonlinear effects of the ground motion on loose sediments have also been studied in some details (Idriss and Seed, 1968; Joyner and Chen, 1975, Beresnev et al., 1998). The total effect of the shallow geology on the ground motion is given by the balance between the amplification due to the strong impedance contrasts existing near the free surface, and the exponential attenuation at high frequency due to the anelastic behavior of the shallow materials (either loose sediments or weathered rocks). Resonance phenomena are commonly observed at sites covered by shallow sediments.

In recent times, the effect of the weathered layer at rock sites has been investigated (Boore, 1986; Silva and Darragh, 1995; Steidl et al., 1996; Boore and Joyner, 1997). Rock outcrops might distort the spectra of the seismic waves because of the impedance contrast generated by the weathered layer. As part of the National Earthquake Hazard Reduction Program (NEHRP), a rock site classification has been given (see BSSC, 1994), together with a soil site classification. The basic criterion chosen to classify different sites was the average shear velocity in the first 30 m. A rock site is so classified if it is underlain by no more than 4-5 m of soil. Rock sites are divided into two categories, rock and very hard rock ones, depending on the average shear-wave velocity value observed in the first 30 m from the free-surface (BSSC, 1994). Soil sites are classified as being either stiff or

soft ones.

Rock sites are generally characterized by strong velocity gradients in the first few tens of meters in depth. Strong scattering phenomena are also expected to take place within the weathered rock layer. Very hard rock sites are common at temperate latitudes, that experienced glaciation in recent geological times (for example in the eastern and western US and Canada). The scouring action of the moving ice removed the weathered rock layer and exposed a very hard, unfractured basement.

The frequency-dependent factor $SITE_i(f)$ used in this study gives a phenomenological description of the effect of shallow geology on the ground motion at the i-th site. The increased attenuation at shallow depths can be built-in into the site term, or it can be described by a distinct term of the form: $\exp(-\pi\kappa_0 f)$, effectively separating in this way resonance effects from anelasticity. We prefer the second option, and include a regional estimate of the term $\exp(-\pi\kappa_0 f)$ in the propagation term $D(r, f)$. In doing so, we lump into the $SITE_i(f)$ terms the description of the effects induced by the impedance contrasts, and the attenuation term relative to the local deviation from the regional κ_0.

Empirical relationships can be established to couple the value of κ_0 with the average shear-wave velocity in the weathered layer. As the average velocity decreases, κ_0 is expected to increase (Atkinson and Boore, 1995). Soil sites must be characterized by similar relationships, although the phenomena are expected to be smoother than for rock sites.

The importance of the effect of the exponential term $\exp(-\pi\kappa_0 f)$ on the spectra has been pointed out by Boore and Joyner (1997) in their Figure 8, where they describe the behavior of a rock site affected by a "generic rock

amplification" for different values of κ_0. The same behavior is expected for soil sites. Soil sites will be characterized by a higher value of κ_0.

Although it is not emphasized enough in the present literature, it is clear that a severe dissipation of elastic energy by thick sediments can substantially reduce the expected ground shaking, even though strong nonlinear phenomena like liquefaction can take place when the ground shaking exceeds certain limits.

Linear dissipative effects are expected to dominate at high frequencies, and consequently to decrease the seismic hazard. On the other hand, the contribution of liquefaction to seismic hazard is substantial. It is good to keep in mind, however, that about 90% of the economic loss during a large earthquake occurs outside the nonlinear zone (Rogers et al., 1985). A good example of a deep sedimentary area in the US is the New Madrid Seismic Zone (NMSZ). In Italy a good example is the Po River valley.

2.4.2 Constraints on the Inversion

In order to reduce the number of degrees of freedom of the system, in addition to a "minimum roughness" constraint on the attenuation term $D(r, f)$, we want to fix the value of the functional at some distance at zero:

$$D(r = r_{ref}, f) = 0$$

and at the same time we try to minimize fluctuations of the site terms:

$$\sum_i SITE(f)_i = 0$$

It is clear that the behavior of the constrained system will strongly influence the source terms if systematic effects are present in the whole dataset, or even in some parts of it.

The first constraint will push the inversion to define an "excitation" term at the reference distance, r_{ref}, rather than a "source" term. If systematic effects exist at all sites, the constraint on the site terms will force the average site term at each frequency onto the excitation term during the inversion. Systematic effects arise, for example, when all stations are deployed on shallow, or deep, sediments, as in the case of the New Madrid Seismic Zone network. In such a case, all stations would experience a common effect of amplification (or deamplification) due to the shallow geology. By applying both of the described constraints to this hypothetical dataset, we would force the common site amplification to bias each excitation term. Each dataset must be carefully analysed for this kind of behavior before interpreting the results of the regressions, and different constraints, more suitable for the specific situation, can be applied accordingly. The correct interpretation of the excitation term is that it represents the expected network average motion at the reference distance, for the given earthquake. A different option would be to force a specific site term to be zero if we know it to refer to a hard rock location.

2.4.3   The Coda Normalization Technique: Description and Implementation

To obtain an initial estimate of $D(r, f)$, we use the coda normalization technique (Aki, 1980; Frankel et al, 1990). The time-domain RMS amplitudes of narrow bandpass filtered time histories, in windows centered on a total lapse time τ and running along the seismic coda, can be represented as:

$$\log a_C(f, \tau) = SOURCE_{Coda}(f) + C(f, \tau) + SITE_{Coda}(f)$$

$a_C(f, \tau)$ is the RMS value computed over a moving window centered in at time τ, for a time history filtered at frequency f. Alternatively, $a_C(f, \tau)$ could represent the RMS average of the Fourier spectrum calculated over the same moving window, computed between the two corner frequencies of the bandpass filter.

By using the coda normalization method (Aki, 1980; Frankel et al., 1990), the functional $C(f, \tau)$ is empirically determined. The RMS coda level for each seismogram at a reference lapse time τ_{ref} is then computed, together with the ratio:

$$a_{reduced}(r, f) = a_S(r, f)/a_C(f, \tau_{ref})$$

where $a_S(r, f)$ is the peak amplitude for the filtered time history, following the S-wave arrival. The essence of this method is that the ratio mathematically eliminates the source and site terms (if source and site terms for the coda are linearly proportional to the ones for the S-waves):

$$\log[a_{reduced}(r, f)] = D(r, f) - C(f, \tau_{ref})$$

The choice for τ_{ref} is arbitrary. By forcing $D(r_{ref}, f) = 0$ we remove the arbitrariness in the choice of τ_{ref} and obtain a first-order estimate of the scaling law in the region. Since a "site term" includes the effect of instrument response, we should be able to define $D(r, f)$ by this technique, even for poorly calibrated (or non calibrated) instruments.

The reference distance is usually chosen at the center of the data distribution. For the regional Italian data set described in Chapter 3, we chose $r_{ref} = 40$ km. For the study of the high-frequency attenuation in the Central Apennines (Chapter 4) we chose $r_{ref} = 10$ km. Finally, in order to ob-

tain the attenuation functional in the German region, we chose $r_{ref} = 100$ km.

Since the distribution of reduced amplitudes in most cases is strongly affected by the presence of outliers, a L_1-norm (FORTRAN code CL1, Bartels and Conn, 1980) is preferred for the minimization of the residuals.

The logarithm of each reduced amplitude (indicated by $A_i(r)$ in what follows) represents a sample of the attenuation term, $D(r, f)$, taken at a different hypocentral distance, r.

Recall that:

$$D(r, f) = \sum_{j=1}^{n} L_j(r)D_j(f)$$

and

$$D_j(f) = D(r = r_j, f)$$

Each reduced amplitude, characterized by a hypocentral distance

$$r_j \leq r \leq r_{j+1}$$

can be written

$$A_i(r) = L_j(r)D_j + L_{j+1}D_{j+1} - C(f, \tau_{ref})$$

Also, since the contribution to two adjacent nodes is computed by linear interpolation, we can write

$$A_i(r) = pD_j + (1 - p)D_{j+1} - C(f, \tau_{ref}).$$

where

$$p \leq 1$$

What follows indicates the way in which the linear system defined by all our observations (the reduced amplitudes) can be expressed in matrix

form. The last rows of the matrix equation, below the first dotted line, implement the smoothing constraint (down to the second dotted line), as well as the constraint:

$$D(r = r_{ref}, f) = 0$$

forced on the system in the last row of the matrix. The role of the constraint is that it eliminates the term $C(f, \tau_{ref})$ from the equation above, and consequently from the matrix. w is a weight, a large number in this case, used to force the constraints more effectively. The matrix applies to data from a single frequency. Each frequency is treated separately in this approach.

An L_1 norm minimization algorithm was preferred to a L_2 (least-squares) norm because of the presence of large outliers. Since an L_1 minimization does not allow the computation of any variance on the model parameters, a least-squares regression was also performed on the same linear system, in order to compute an estimate of the uncertainties to be associated to the inverted parameters. The least squares inversion was carried out through a Singular Value Decomposition (SVD) algorithm (Lawson and Hanson, 1974; Russell, 1987), applied on the following system:

$$\mathbf{A}_{\{n+m+1\}\times 1} = \mathbf{B}_{\{n+m+1\}\times m}\mathbf{D}_{m\times 1}$$

$$
\begin{pmatrix} A_1 \\ A_2 \\ \vdots \\ \vdots \\ A_n \\ \cdots \\ 0 \\ \vdots \\ \vdots \\ \vdots \\ 0 \\ \cdots \\ 0 \end{pmatrix} = \begin{pmatrix} 0 & p & 1-p & 0 & \cdots & 0 \\ p & 1-p & 0 & 0 & \cdots & 0 \\ \vdots & & \vdots & & & \vdots \\ \vdots & & \vdots & & & \vdots \\ 0 & 0 & p & 1-p & \cdots & 0 \\ \cdots\cdots\cdots\cdots\cdots\cdots\cdots\cdots\cdots\cdots \\ -2w & w & 0 & 0 & \cdots & 0 \\ w & -2w & w & 0 & \cdots & 0 \\ \vdots & & \ddots & & & \vdots \\ \vdots & & \vdots & \ddots & & \vdots \\ \vdots & & \vdots & & \ddots & \vdots \\ 0 & 0 & 0 & \cdots & w & -2w \\ \cdots\cdots\cdots\cdots\cdots\cdots\cdots\cdots\cdots\cdots \\ 0 & 0 & w & 0 & \cdots & 0 \end{pmatrix} \times \begin{pmatrix} D_1 \\ D_2 \\ D_3 \\ \vdots \\ \vdots \\ \vdots \\ \vdots \\ \vdots \\ \vdots \\ D_{ndist} \end{pmatrix}
$$

In the matrix equation above, dotted lines are used to separate the section of the matrix rows that are relative to the data, from the rows used to implement the constraints. Within the rows that implement the constraints, the ones relative to the smoothing constraint are separated by another dotted line from the one that forces the attenuation functional to zero at the reference distance.

2.4.4 Implementing the General Regression

The general regression is set up in a way that is very similar to the one just used for the simpler problem of the reduced amplitudes in the coda normalization method. In this case, the linear equation used to describe the logarithm of the observed amplitude recorded at a distance $r_j \leq r \leq r_{j+1}$,

$$
A_k(f) = SOURCE_i(f) + pD_j(f) + (1-p)D_{j+1}(f) + SITE_l(f)
$$

where $k = 1, 2 \cdots n$ (number of observation),

$i = 1, 2, \cdots ne$ (number of earthquakes),

$j = 1, 2, \cdots m$ (number of distance terms), and

$l = 1, 2, \cdots ns$ (number of sites).

The matrix form of the described problem can be then written as:

$$\mathbf{A}_{\{n+m+1\}\times 1} = \mathbf{B}_{\{n+m+1\}\times\{ne+m+ns\}}\mathbf{M}_{\{ne+m+ns\}\times 1}$$

The $\{A_k\}$ is the set of the available data, either the logarithms of the peak values of the filtered time histories, or the logarithms of the RMS averages of the windowed S-waves Fourier spectra. The right-hand side terms of the constraint equations are also in the $\{A_k\}$ vector.

In the explicit matrix equation, rows relative to data and constraints are separated by the first horizontal dotted line in each term. The row between the first and the second dotted lines refers to the constraint forced on the site terms; rows between the second and the third dotted lines are relative to the the smoothing of the attenuation term. The row below the last line of dots forces the attenuation functional to be zero at the reference distance.

The explicit matrix form of the linear system of equation just described is

Source Terms   Distance Terms   Site Terms

$$
\begin{pmatrix} A_1 \\ A_2 \\ \vdots \\ \vdots \\ A_n \\ \cdots \\ 0 \\ \cdots \\ 0 \\ \vdots \\ \vdots \\ 0 \\ \cdots \\ 0 \end{pmatrix}
=
\left(
\begin{array}{cccc|cccccc|cccc}
1 & 0 & \cdots & 0 & 0 & p & 1-p & \cdots & & 0 & 1 & 0 & \cdots & 0 \\
0 & 0 & \cdots & 0 & p & 1-p & 0 & \cdots & & 0 & 0 & 0 & \cdots & 1 \\
\vdots & \vdots & & \vdots & \vdots & \vdots & & & & \vdots & \vdots & \vdots & & \vdots \\
\vdots & \vdots & & \vdots & \vdots & \vdots & & & & \vdots & \vdots & \vdots & & \vdots \\
0 & 0 & \cdots & 1 & 0 & 0 & p & \cdots & & 0 & 0 & 1 & \cdots & 0 \\
\cdots & & & & \cdots & & & & & & \cdots & & & \\
0 & 0 & \cdots & 0 & 0 & 0 & 0 & \cdots & & 0 & w & w & \cdots & w \\
\cdots & & & & \cdots & & & & & & \cdots & & & \\
0 & 0 & \cdots & 0 & -2w & w & 0 & \cdots & & 0 & 0 & 0 & \cdots & 0 \\
\vdots & \vdots & & \vdots & w & -2w & w & \cdots & & 0 & \vdots & \vdots & & \vdots \\
\vdots & \vdots & & \vdots & \vdots & \vdots & \ddots & & & \vdots & \vdots & \vdots & & \vdots \\
\vdots & \vdots & & \vdots & \vdots & \vdots & & \ddots & & \vdots & \vdots & \vdots & & \vdots \\
0 & 0 & \cdots & 0 & 0 & 0 & \cdots & & w & -2w & 0 & 0 & \cdots & 0 \\
\cdots & & & & \cdots & & & & & & \cdots & & & \\
0 & 0 & \cdots & 0 & 0 & w & 0 & \cdots & & 0 & 0 & 0 & \cdots & 0
\end{array}
\right)
\times
$$

$$
\times
\begin{pmatrix}
SRC_1 \\
SRC_2 \\
SRC_3 \\
\vdots \\
SRC_{ne} \\
\cdots \\
D_1 \\
D_2 \\
D_3 \\
\vdots \\
\vdots \\
D_m \\
\cdots \\
SITE_1 \\
SITE_2 \\
SITE_3 \\
\vdots \\
SITE_{ns}
\end{pmatrix}
$$

The general regression is performed by using a least-squares algorithm. A search is carried out through the parameter space to find the minimum of the quantity:

$$\sum_i \left(\left(D_{kOBS} - D_{kPRED} \right) / \sigma_i \right)^2)$$

The σ_i are those resulting from the regression.

2.5   Forward Modeling

Given i) a source model, ii) the attenuation parameters $Q(f)$ and κ_0, iii) the geometrical spreading function $g(r)$, and iv) a functional form to quantify the duration of the seismic signal as a function of hypocentral distance and frequency, we can try to reproduce the empirical estimate of the attenuation functional $D(r, f)$, as well as the empirical excitation terms at the arbitrary reference distance $r = r_{ref}$.

The general equation describing the attenuation parameter $Q(f)$ is the following:

$$Q(f) = Q_0 \left(\frac{f}{f_r} \right)^\eta .$$

However, since the reference frequency $f_r = 1.0$ Hz, throughout this study we will use the simpler form:

$$Q(f) = Q_0 f^\eta.$$

Forcing the synthetic attenuation terms to be zero at the reference distance allows to isolate the contributions of the regional anelastic attenuation and the geometrical spreading from the anelastic energy loss at shallow depths described by the parameter κ_0.

It is also important to keep in mind that all the parameters mentioned trade off with each of the others, and with the parameters of the source

spectral model that represent the characteristics of the seismic events in the investigated region. Specifically, the shape of the geometrical spreading function (the steepness of each linear segment in a loglog space) trades off with the anelastic parameter, $Q(f) = Q_0 f^\eta$. The trade off is mostly concentrated on Q_0, since the sensitivity of the attenuation functional on the parameter η alone is usually extremely high. The parameyter κ_0 trades off with the parameters controlling the high-frequency content of the theoretical source spectra used to solve the forward problem.

2.6 Advantages of The Approach:

To obtain a regional predictive relationship, researchers would generally gather a large number of strong-motion recordings and perform a regression to obtain the decay of the ground motion parameters with distance (see Campbell and Bozorgnia, 1994, for a worldwide attenuation relationship for the peak horizontal acceleration, or Boore et al., 1993, for a study on data from western North America).

With the approach just described, we can use seismograms of the background seismicity. The consequence of this choice is that, since we no longer need strong-motion recordings for our regressions, large amounts of data from microseismic networks become available. Another advantage, compared to a traditional approach, is that now we can apply the coda normalization technique to integrate our datasets with poorly-calibrated waveforms. The technique is also used to obtain a first estimate of the attenuation functional, to be used as a starting model for the general regression. Finally, what is probably the most important advantage of the

approach described in this chapter is that we need not to formulate hypotheses on the functional form of the scaling laws before the regression.

3. Ground Motion Scaling in the Apennines (Italy)

3.1   Introduction

3.1.1   Earthquake Spectral Parameters Along the Apennines:

Rovelli et al. (1988) analyzed 75 strong-motion accelerograms from the central and the southern Apennines ($4 \leq M \leq 7$), all from normal faulting, in the $0.1 \leq f \leq 20$ Hz spectral band. By using an ω^2 model (see Appendix C) to match the observed acceleration spectra, they investigated the spectral parameters M_0, f_c, $Q(f)$ and κ_0. The distance range spanned by the accelerograms was 8-147 km. 62% of the recordings were within 40 km, 72% of them within 50 km.

They modeled the observed acceleration spectra as:

$$A(f) = \left[\frac{S(f; M_0, f_c)}{r} \right] \exp\left[-\pi \kappa_0 f \right] \exp\left[\frac{-\pi f r}{v_s Q(f)} \right]$$

where the source term $S(f; M_0, f_c)$ depends on the scalar moment of the earthquake, M_0, and on its corner frequency, f_c, which, in turn, depends on the third root of the [stress-drop/ scalar moment] ratio (Appendix C).

Rovelli et al. (1988) verified the cube relationship for the events along the Apennines, and found a constant value for the stress parameter

$$\Delta \sigma = 190 \pm 64 \ \text{bar}.$$

They also carried out a regression on the attenuation parameters κ_0 and Q_0, by following the method presented by Anderson and Hough (1984).

A qualitative analysis of the linearity of the spectral fall-off was done in order to eliminate noisy spectra. obtaining the following results:

$$\kappa_0 = 0.07 \pm 0.02 \ s$$

$$Q(f) = Q_0 \cdot f^{1.0}$$

$$Q_0 = 100.$$

The value of the regional parameter Q_0 showed large fluctuations, between 40 and 120 s, with a strong frequency dependence. The high crustal attenuation in the Apennines is a common feature of tectonically active regions. Rovelli at al. (1988) analysed the variability of κ_0 with the hypocentral distance and concluded that it was smaller than the $\sim 30\%$ uncertainty on the parameter itself.

We will see that our estimate of the attenuation parameter $Q(f)$ is substantially different from the one just mentioned. For this reason, in what follows we will not use the spectral model proposed by Rovelli et al. (1988). For our convenience we will use a spectral model characterized by a lower stress drop (70 bar). This model has been proposed by Boore and Joyner (1997) for events of southern California. The functional form for this model is given in Appendix C, multiplied by a site amplification term $V(f)$ taken from Atkinson and Silva (1997), based on that in Boore (1986).

3.1.2   Preexisting Predictive Relationships for the Apennines:

Sabetta and Pugliese (1987), hereafter SP87, were the first to describe the results of a regression on strong-motion waveforms (accelerograms) for Italy. They defined the attenuation characteristics of the peak horizontal acceleration (PHA) and peak horizontal velocities (PHV). SP87 is still a standard reference work for the Italian structural engineers.

In their regression, SP87 used the functional form

$$f(y) = a + f_1(M) + f_2(r) + f_3(S) + \epsilon$$

where y is the strong motion parameter to be predicted and ϵ is the uncertainty associated with $f(y)$.

$$f(y) = \log y$$

$$f_1(y) = bM$$

$$f_2(r) = C \log r.$$

If anelastic attenuation is taken into account, we can write:

$$f_2(r) = C \log(r^2 + h^2) + D \cdot r$$

where C is the geometrical spreading exponential, r is a generic distance from the fault that can be chosen in different ways, h is a fictitious depth determined by the regression, and $D \cdot r$ is the anelastic attenuation coefficient. SP87 chose

$$C = -1 \text{ and } D = 0.$$

These assumptions are valid only for distances shorter than that where supercritical reflections first appear, and for a perfectly elastic medium.

In treating PHA, SP87 grouped together stiff and deep soil sites, since shallow soil sites showed larger amplification for the peak acceleration with respect to the stiff ones. For the regression on the PHV's, deep and shallow soil sites were grouped together because of their similar behavior. Deep soil average PHA and PHV were 87% of the average PHA, and 130% of the average PHV at rock sites, respectively.

The database used by SP87 contained 190 horizontal component accelerograms, generated by 17 events that have occurred in Italy since 1976 ($4.6 \leq M \leq 6.8$), in different tectonic environments. Recordings from a compressional region (Friuli) and three extensional ones were gathered in two groups (the time histories from Irpinia and those from central Italy-Sicily). In grouping together central Italy and Sicily, some perplexities may arise because it is known that Sicily is characterized by a lower regional attenuation (higher values of Q) than central Italy (Di Bona, personal communication). Nevertheless, regressions performed separately on data from compressional and from extensional earthquakes gave results within the error estimates of the regression performed on the combined dataset.

Sites were classified as follows:

- **stiff:** characterized by the following average shear-wave velocity:

$$v_s > 800 \ \text{m/s}$$

(limestone, sandstone, siltstone, marl, shale, conglomerate);

- **soil:** characterized by the following average shear-wave velocity:

$$400 \leq v_s \leq 800 \ \text{m/s}$$

(alluvium; sand; gravel; clay; silt).

A soil site characterized by no more than 4-5 m of sediments, was considered a stiff site.

On the basis of the recent experience gained in studying the propagation of surface-waves in loose sediments (Malagnini et al., 1995; Malagnini, 1996; Malagnini et al., 1997), we know that the values of shear-wave velocity indicated for soils by SP87 are too high to describe the elastic properties of shallow, soft sediments.

The final functional form adopted by SP87 to model PHA and PHV was

$$\log y = a + bM - \log(r^2 + h^2)^{\frac{1}{2}} + cS$$

and their final results were:

$$\log PHA = -1.562 + 0.306 M - \log(r^2 + 5.8^2)^{\frac{1}{2}} + 0.169 S$$

for the peak ground acceleration, and

$$\log PHV = -0.710 + 0.455M - \log(r^2 + 3.6^2)^{\frac{1}{2}} + 0.133 S$$

for the peak ground velocity. In the formulas above, PHA is measured in g, and PHV in cm/s; M is the local magnitude, r is the closest distance to the surface projection of the fault rupture (in km), and S is a variable taking a value in the $[0, 1]$ interval, according to the site geology:
For PHA, $S = 0$ for stiff and deep soil sites and $S = 1$ for shallow soil sites.
For PHV, $S = 1$ for shallow and deep soil sites and $S = 0$ for stiff sites.

SP87 stated that, by choosing r to be the epicentral distance, the final results were very similar, although the standard errors were significantly higher. SP87 used the largest of the two peaks of the horizontal

time histories. They generally referred to M_L, but they used M_S when both M_L, $M_S \geq 5.5$.

Sabetta and Pugliese (1996), hereafter SP96, developed empirical predictive relationships for the vertical and the horizontal components of the response spectra. The database used by both SP87 and SP96 was the same. Out of the 190 horizontal component acceleration time histories SP96 used 95 horizontal accelerograms.

The multiple regression was carried out using the following functional form for 14 different frequencies in the range 0.25 - 25 Hz:

$$\log(y) = a + bM + c \log(r^2 + h^2)^{\frac{1}{2}} + e_1 S_1 + e_2 S_2$$

S_1 and S_2 refer to the site classification, and take the values of 1 for shallow and deep soil sites, respectively, and 0 otherwise. As in their previous paper (SP87), SP96 used $c = -1$ (direct-wave geometrical spreading). Table 4 of SP96 provides the values of (a, b, c, e_1 and e_2) for each one of the chosen frequencies.

Along the Apennines, SP96 observed that the anelastic attenuation acts mainly in the shallow soil layers, and therefore depends more on the local site conditions than on the source-receiver path. In our results, however, we show that the regional attenuation plays the most important role.

3.2 The Dataset

The dataset analysed in this paper consists of more than 3,000 three-component seismograms (over 6,000 horizontal time histories), from 446 regional earthquakes. They were recorded by three transects deployed by the *Istituto Nazionale di Geofisica* (ING), respectively across the northern,

central and southern Apennines for recording teleseisms (Amato et al., 1994a, 1994b, 1995a, 1995b, 1998a), and by two temporary, portable networks. The latter two were installed in Umbria (central Italy) by ING to monitor the Massa Martana seismic sequence, that followed the $M = 4.5$ event occurred on May 12, 1997, 13:50 GMT, and to monitor the Colfiorito seismic sequence that followed the $M_w = 6.0$ earthquake occurred on September 26, 1997, 09:40 GMT (Amato et al., 1998b).

Most of the recording sites deployed in these experiments were equipped with broad-band instruments. Since these arrays sampled events in different, non-overlapping periods of time, we also use data from two permanent stations of the MedNet network (a digital, broadband Mediterranean network operated by ING), which recorded events in common with the transects, and the Colfiorito arrays. In this way, possible tradeoffs due to systematic effects on the recorded amplitudes (instrumental or site-related distortions of the signals) can be detected, or at least reduced. The two reference stations, AQU and CII, are located near L'Aquila and Carovilli, respectively, in central and southern Italy. Unfortunately, CII only partially covered the time span of the whole dataset.

Strong motion stations of the National Accelerometric Network operated by the Electric Power Company (ENEL) recorded some of the mainshocks of the Colfiorito sequence. Those records were also included in the dataset, although they were used only for the stage of the coda normalization at regional distance, and excluded from the final regression.

The source-receiver distance distribution for the whole dataset is shown in Figures 3.1 and 3.2. The y-axes of the two plots display the station names, the x-axes show the source-receiver hypocentral distance. The

distance distribution for the data recorded along the three transects is displayed in Figure 3.1 and the hypocentral distance distribution for the Colfiorito and Massa Martana datasets is plotted in Figure 3.2.

3.2.1 The Teleseismic Transects

In summer 1994, a two-year project called: "Geodynamic Modelling of an active Region of the Mediterranean: the Apennines," was funded by the European Community (Contract EV5V-0464). The goal of that project was to define a geodynamic model of the Apennines (Amato et al., 1994a, 1994b). The area of interest for this project included the northern, central, and southern Apennines, in the $40.5 - 43.5°$N latitude range.

Three teleseismic transects were deployed across the Apennines over periods of several months in 1994, 1995 and 1996. The main purpose for deploying the transects was to record teleseisms to be used for receiver-function studies and seismic tomography. A sampling rate of 20-40 sps was chosen for each station of the teleseismic transects. Each system provided continuous recordings.

The northern Apennines Transect (1994)

Operating between June and August 1994, this experiment consisted of 10 digital recorders deployed along a line from Corsica to the Adriatic coastline (Amato et al., 1994a, 1994b, 1995b). The transect was 340 km long, with an average interstation spacing of 32 km from Elba to Conero. Figure 3.3 shows a map of the region, as well as the locations of the seismic stations and events of interest.

The region crossed by this transect is of geodynamic interest because

Apennines
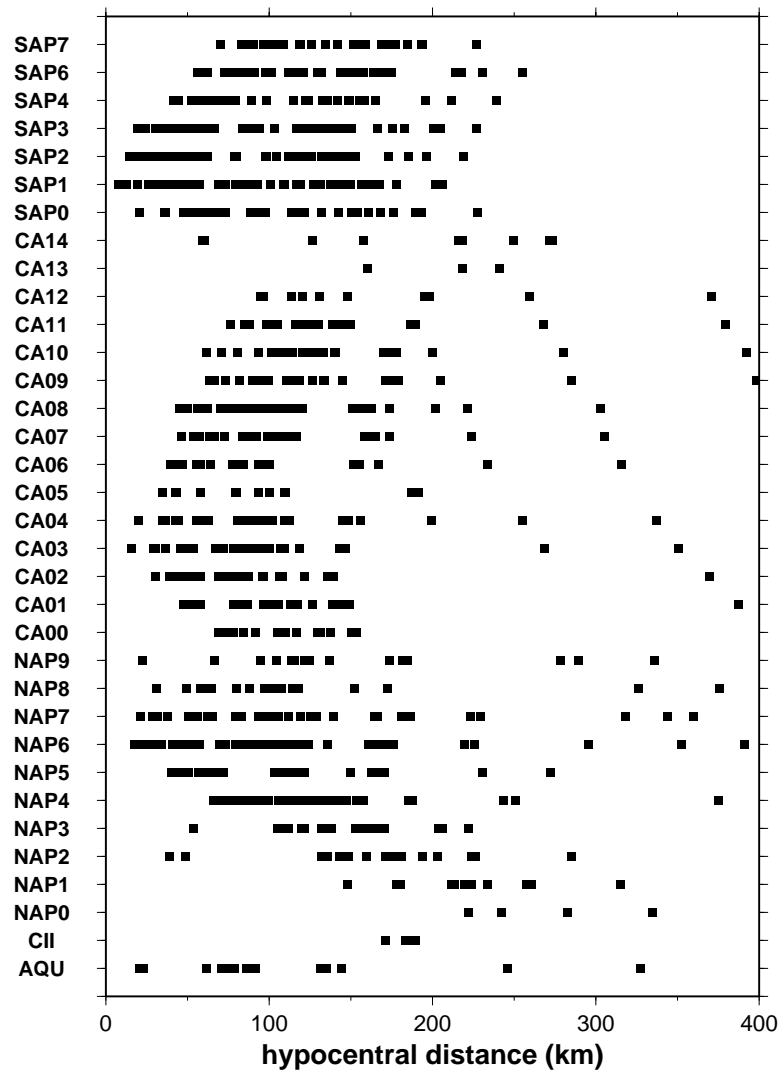
Figure 3.1: Source-receiver hypocentral distance distribution for the data recorded along the three teleseismic transects.

Apennines
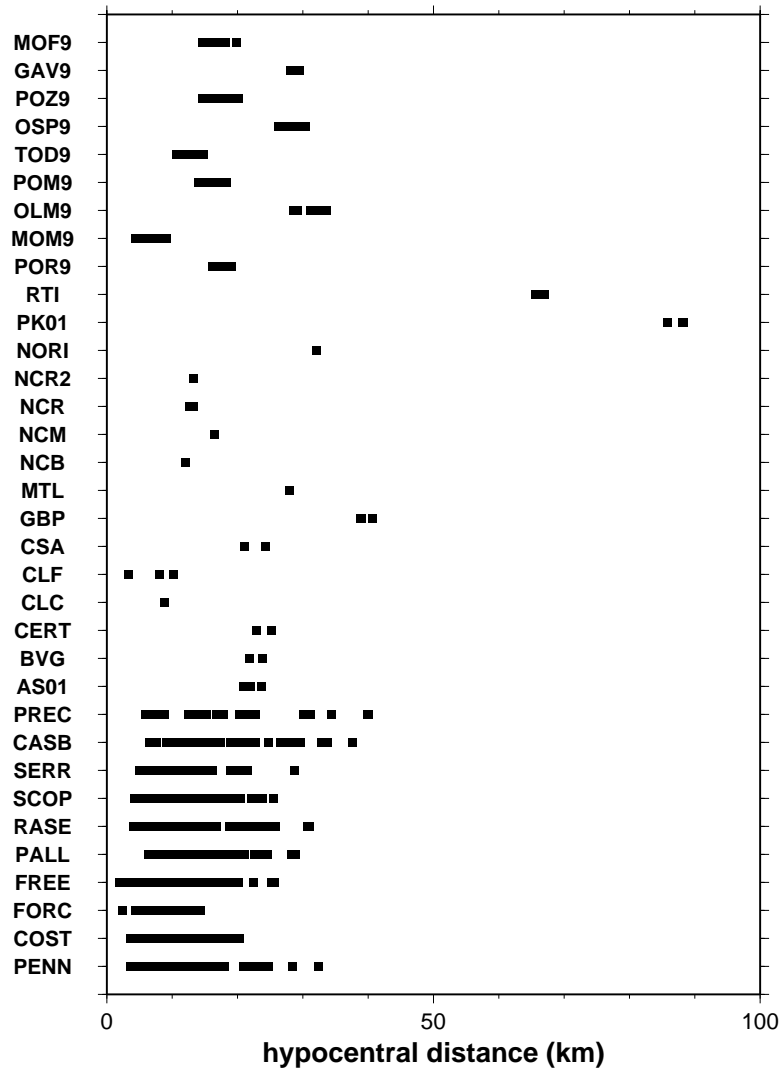
Figure 3.2: Source-receiver hypocentral distance distributions for the Massa Martana and Colfiorito campaigns.
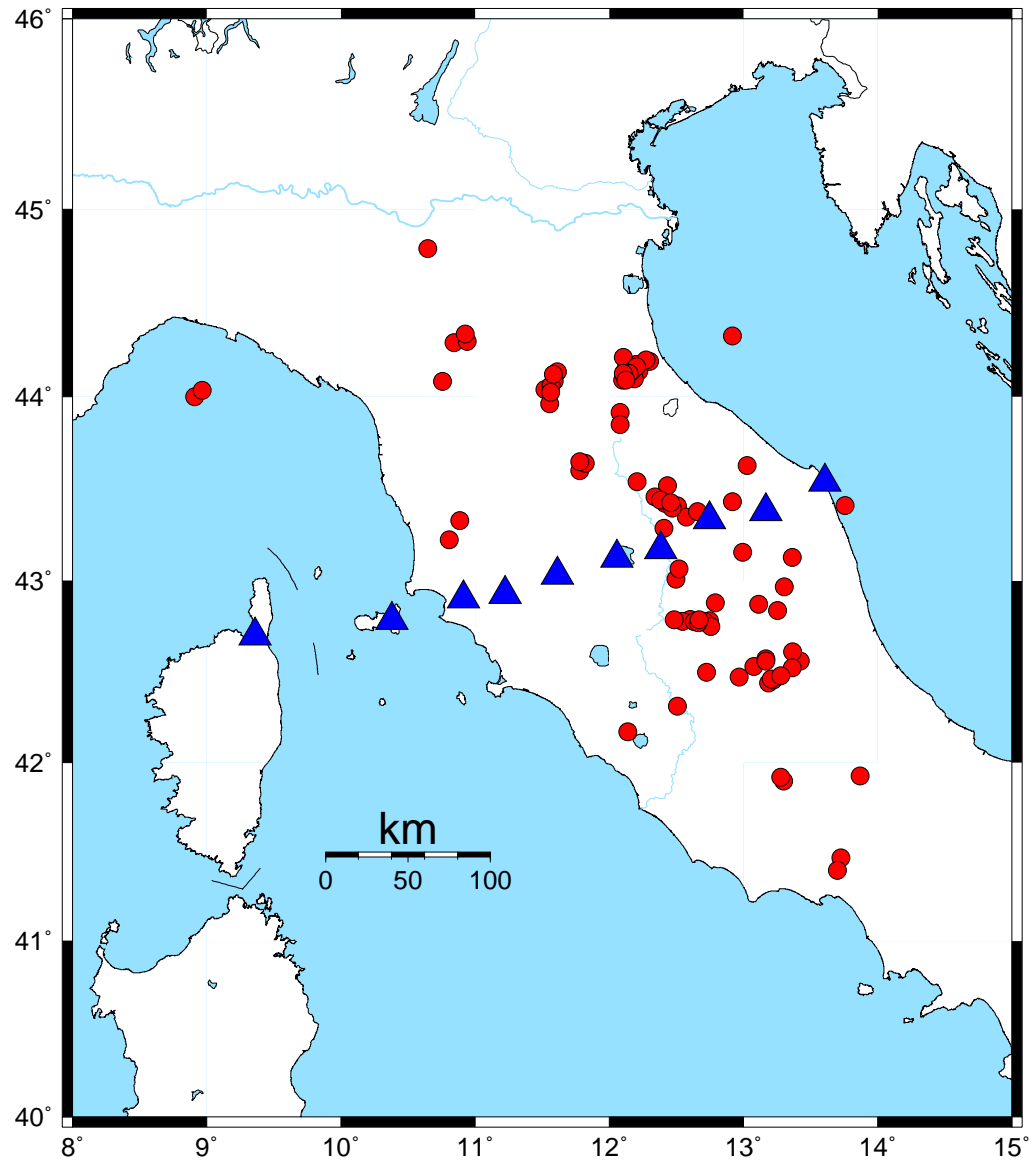
Figure 3.3: Map of the northern Apennines. Blue (black) triangles indicate the positions of the recording stations of the northern Apennines Teleseismic Transect (1994); red (gray) circles denote the location of the epicenters of the regional events recorded during the experiment.

of the occurrence of subcrustal earthquakes, deeper than 90 km (Selvaggi and Amato, 1992), and because of the existence of a strong high-velocity anomaly beneath Tuscany (Amato and Chiarabba, personal communication) that lies deeper and to the west of the subcrustal seismicity. These observations indicate a residual west-southwestward subduction of the Adria plate beneath the Apennines, and a related extension of the lithosphere in the internal part of the northern Apennine arc, a back-arc region (Anderson and Jackson, 1987).

Each recording site along the 1994 transect was equipped with a RefTek 72a-07 24-bit digitizer. Continuous recordings were stored on hard disks (5 sites) or on DAT cassettes (5 sites). Each station was instrumented with three-component seismometers: Lennartz LE/3D (feedback, 5 sec) at seven sites, Kinemetrics S-1 (5 sec) at two sites, and Guralp CMG3 T-ESP at one site. The sampling rate was set at 40 sps for all stations.

The Central Apennines Transect (1995)

In spring-summer 1995, a second teleseismic transect was deployed across the central Apennines (Amato et al., 1995b). The transect operated from April to July 1995, with 15 digital stations, from Tolfa (Rome) on the Tyrrhenian coast, to the Tremiti islands in the Adriatic Sea. Figure 3.4 shows a map of the area involved in the experiment. The figure shows the station locations and the epicentral locations of the regional events that are used in this study.

A substantial change in the depth of the Moho is observed along the direction where the transect is deployed. The Moho is about 25 km deep in western peninsular Italy, and 35 km deep on the Adriatic side of the
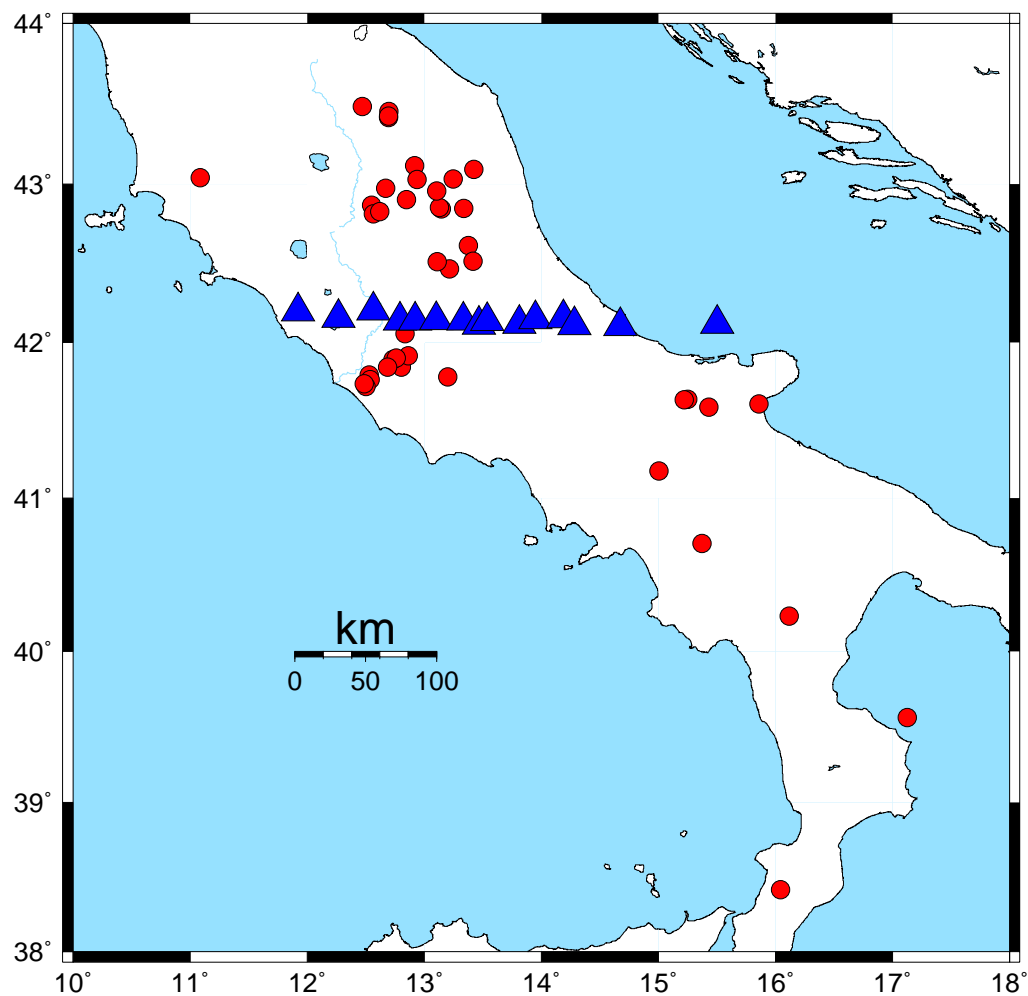
Figure 3.4: Map describing the central Apennines Teleseismic Transect, deployed in 1995. Blue (black) triangles indicate the positions of the recording stations; red (gray) circles denote the epicentral locations of the regional events recorded during the experiment.

Apennines (Geiss, 1987). This observation is also consistent with the west-southwestward subduction of the Adria plate beneath the Apennines.

The recording sites along the transect of 1995 were equipped with RefTek 72a-07 24-bit digitizers. Continuous recordings were stored on hard disks (6 sites) or on DAT cassettes (9 sites). Each station was also instrumented with three-component seismometers: Lennartz LE/3D (5 sec) instruments were deployed at eleven sites, a Guralp CMG4 T at one site, a Guralp CMG3 T-ESP at one site, a Guralp CMG3 at one site, and Guralp CMG4's at two sites. A sampling rate of 20 sps was chosen for this experiment.

The Southern Apennines Transect (1996)

A third teleseismic transect was deployed across the southern Apennines from the beginning of April 1996 to the beginning of November 1996. It consisted of 8 stations instrumented with RefTek 72a-07, 24-bit digitizers. At 3 sites we had Lennartz LE/3D (5 sec) seismometers, whereas the remaining 5 sites were equipped with Guralp CMG40T broadband sensors.

Each seismic station continuously recorded data for the whole duration of the experiment. For the first month of operation only, the sampling rate was set to 40 sps; then it was reduced to 20 sps. Figure 3.5 shows the location of the recording sites of this transect, together with the epicentral locations of the events used in this study.

3.2.2 The Massa Martana Campaign (1997)

On May 12, 1997, at 13:50 GMT, an $M_W = 4.5$ event occurred near the town of Massa Martana. In order to monitor the sequence of aftershocks,
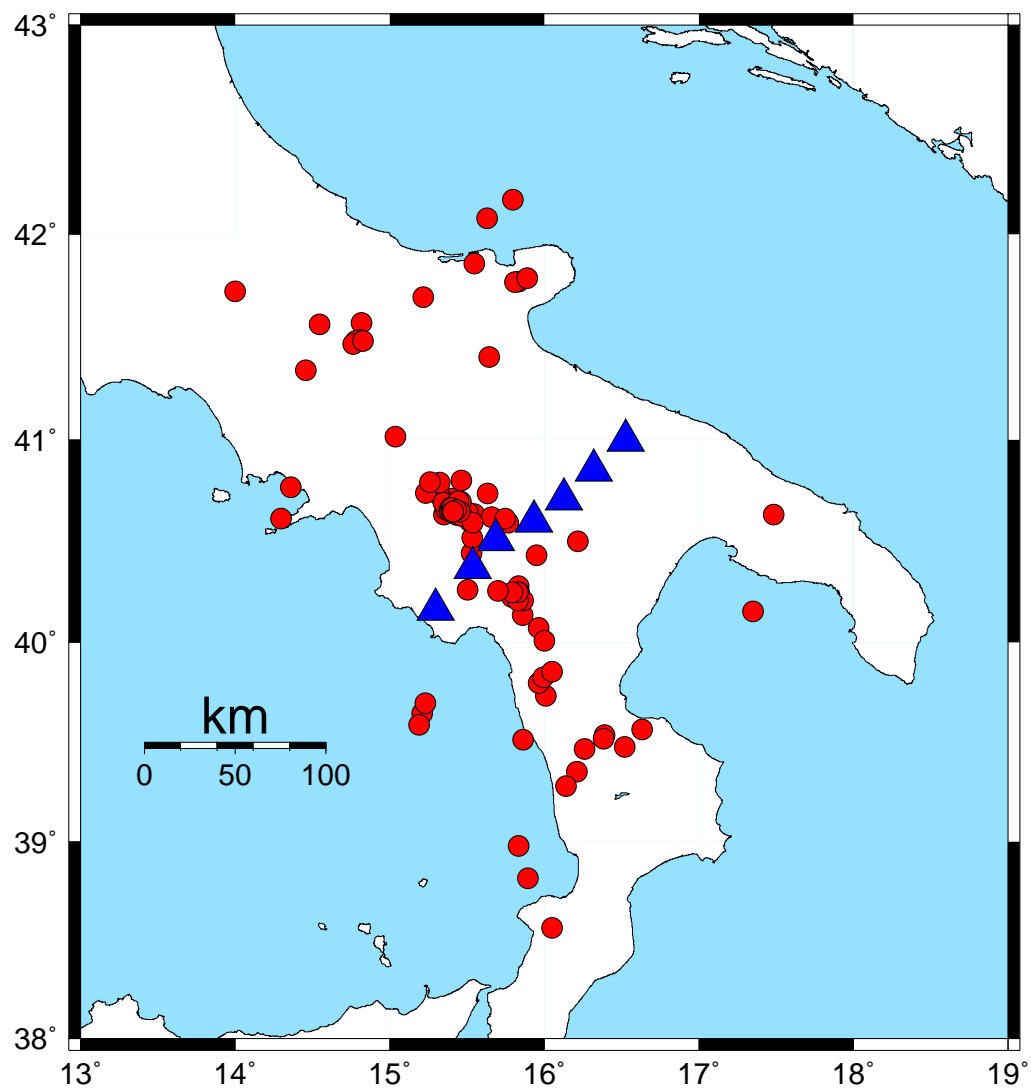
Figure 3.5: Map of the central Apennines Teleseismic Transect deployed in 1996. Blue (black) triangles indicate the positions of the recording stations; red (gray) circles indicate epicentral locations of the regional events recorded during the experiment.

the Istituto Nazionale di Geofisica installed a local network of 9 stations shortly after the main event occurred. All stations were equipped with RefTek 72a-07 digitizers. The seismometers included Lennartz LE/3D's at 4 sites, Guralp CMG40T at 4 sites; and a three-component Mark Product L4-3D at one site. The sampling rate chosen for the stations operating during this campaign was 100 sps. Figure 3.6 shows the stations of the local network (black squares), and the locations of the events used in this study.

3.2.3 The Colfiorito Campaign (1997)

The Colfiorito seismic sequence followed an $M_w = 6.0$ earthquake that occurred on September 26, 1997, 09:40 GMT. The sequence was closely monitored by a local network installed by ING, starting on the first day of activity. The temporal and spatial evolution of the seismicity in the area has been described by Amato et al. (1998b). Figure 3.6 shows the locations of the portable seismic stations (blue, or dark, triangles) and of the events used in this study. All the 10 stations were instrumented with RefTek 72a-07 digitizers and CMG40T three-component broadband sensors. Recordings were taken continuously at a rate of 100 sps. Accelerograms from two of the main events of the sequence, recorded by the strong-motion national network run by ENEL, the national power agency, were also used. The locations of the accelerometers are indicated in the map by the lighter inverse triangles; the location of the two main events by the white hexagons (partially covered and overlapping).
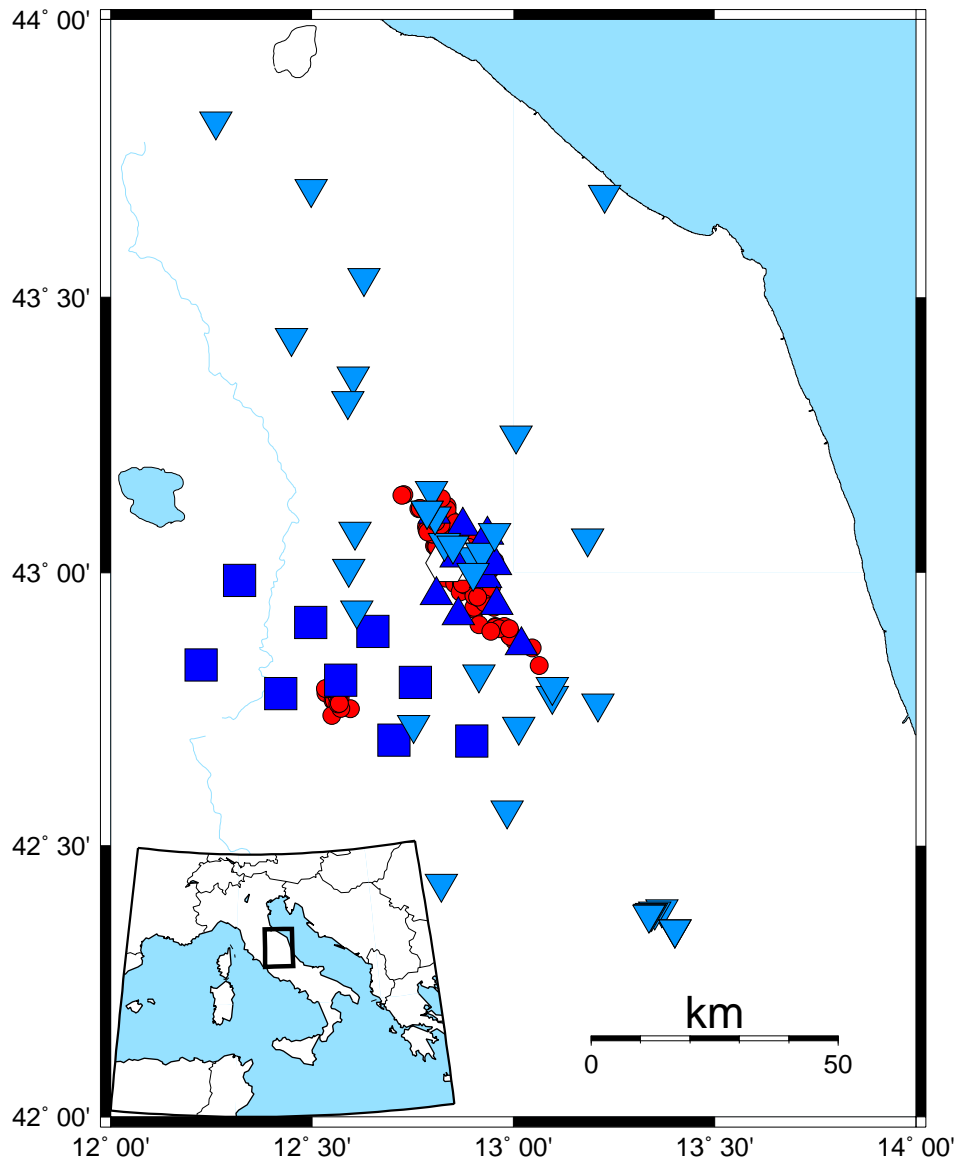
Figure 3.6: Map of the area struck by the Colfiorito earthquake sequence in September-November 1997, and by the May 12, 1997 event of Massa Martana. The locations of the white hexagons (only one is clearly visible) within the large cloud of red (gray) dots (epicentral locations) are relative to two of the main shocks of the Colfiorito sequence. The small cloud of epicentral locations located SW of the Colfiorito events marks the aftershock area of the Massa Martana event. Both sequences have been closely monitored by ING portable arrays deployed in the areas around Massa Martana (blue -dark- squares indicate the positions of the seismic stations of the portable network) and Colfiorito (dark-blue -black- triangles represents the ING portable stations. Light-blue -dark gray- reversed triangles indicate the locations of the accelerometers of the National Accelerometric Network run by ENEL).

3.3 Data Processing

3.3.1 The Bandpass Filters

As described in the previous chapter, each time history of the Italian data set was bandpass filtered around a set of sampling frequencies (0.25, 0.33, 0.4, 0.5, 1.0, 2.0, 3.0, 4.0 and 5.0 Hz), by using a set of 8-pole hi-pass Butterworth filters, followed by a set of 8-pole Butterworth lo-pass filters, with corners at $1/\sqrt{2}f_{0_i}$ and at $\sqrt{2}f_{0i}$, respectively. The maximum amplitude is then taken from each filtered time history.

3.3.2 Coda Normalization Analysis

Figure 3.7 shows the shape of the decay of the normalized coda with time (thick red lines), computed on the filtered time histories at each one of the suite of sampling frequencies. The RMS average over a running window is computed along each time history, and plotted in the figure as a function of time. The black lines give the RMS value of the pre-event noise, red (gray) parts refer to the RMS of the seismic signals between P- and S-wave arrivals, green (light gray) sections are relative to RMS signals between the S-wave arrivals and the stable coda; finally, the blue (dark) segments of the curves start at $2t_S$ and describe the RMS of the coda as a function of time. Each peak is normalized to the value of the coda at an arbitrary reference time, yielding a first estimate of the $D(r, f)$. The path term is forced to be zero at the reference distance. Figures 3.8 show the estimates of the functional $D(r, f)$ at 0.5, 1, 2, 3, 4 and 5 Hz. The functional $D(r, f)$, computed over the normalized data, is indicated at each frequency by the black line connecting the green (light) diamonds. Indi-

vidual reduced amplitudes are indicated by small red (dark) diamonds. Larger green (light gray) diamonds indicate the values of $D(r, f)$ at the distance nodes.

From a visual inspection of Figure 3.8 we can see that the distribution of the normalized amplitudes at all frequencies is characterized by the presence of large outliers. For this reason we chose to use an L1-norm minimization of the residuals for this stage of the analysis to avoid bias.

3.3.3 Duration of Ground Motion

In order to use the RVT to compute the peak values of the filtered time histories we need to associate with each frequency and distance the corresponding duration of the seismic signal. Following Raoof et al. (1999), we estimate the $5 - 75\%$ duration of the seismic ground motion for all the available recordings, band-pass filtered around each one of the sampling frequencies in the following set: 0.25, 0.30, 0.40, 0.5, 1.0, 2.0, 3.0, 4.0 and 5.0 Hz. Figure 3.9 shows the estimated durations versus distance at some of the indicated frequencies.

In this case, an L_1-norm optimization is also used to obtain an estimate of the duration as a function of distance at each central frequency. Results of the inversion are shown by the green (light gray) diamonds in Figure 3.9. The duration of the seismic signal as a function of distance is well defined at all frequencies, in the diagrams in Figure 3.9. This functional dependence will be important when the predictive modeling of the ground motion decay will be attempted by using the RVT.
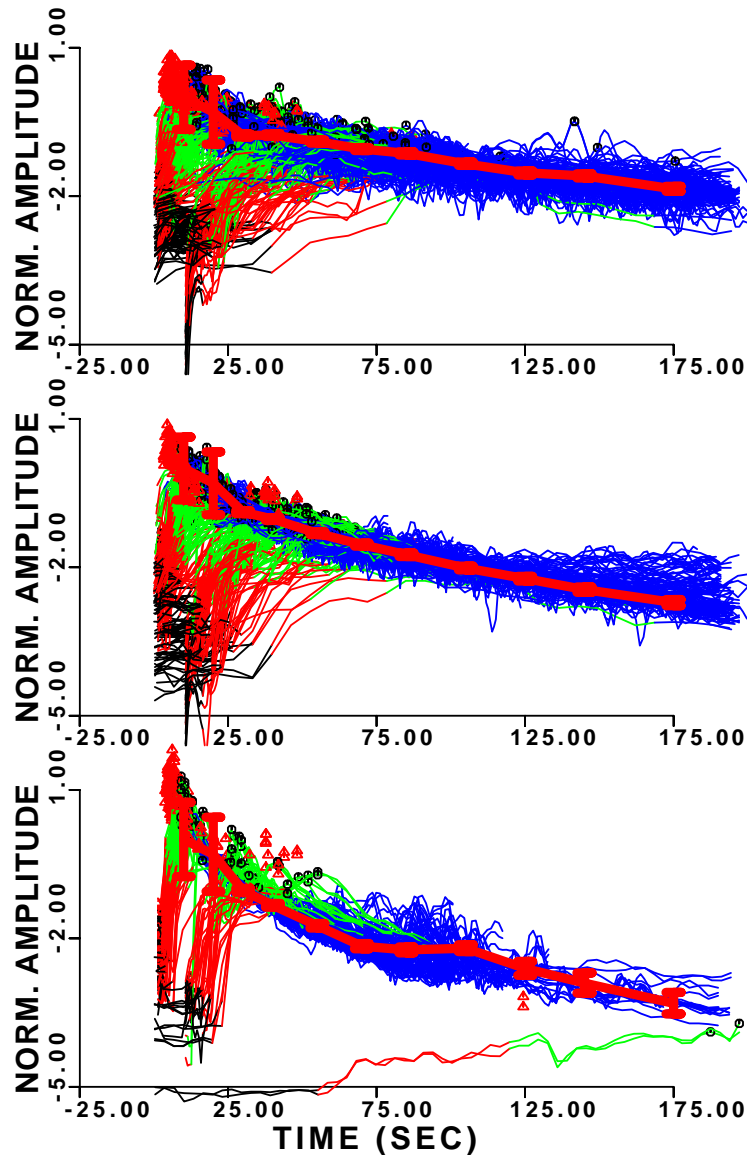
Figure 3.7: The shape of the seismic coda at 0.5, 1.0 and 5.0 Hz (bottom to top frames) as a function of time is indicated by the thick red (gray) lines. Error bars are also represented. The color (or tone of gray) figures represent the RMS value of the seismic signals (filtered velocities) for each processed waveform. The initial black sections of the lines indicate the RMS value as a function of time of the signal preceding the P-wave arrivals (seismic noise). Red (gray) segments are relative to the RMS values of the signals between the P- and the S-wave arrivals. Green (light gray) segments refer to the seismic signals arriving after the S-wave arrivals. Blue (dark) segments indicate the RMS value of the coda seismic signals (after twice the S-wave arrival times). Red (gray) triangles indicate the peak values for each filtered, normalized time history.
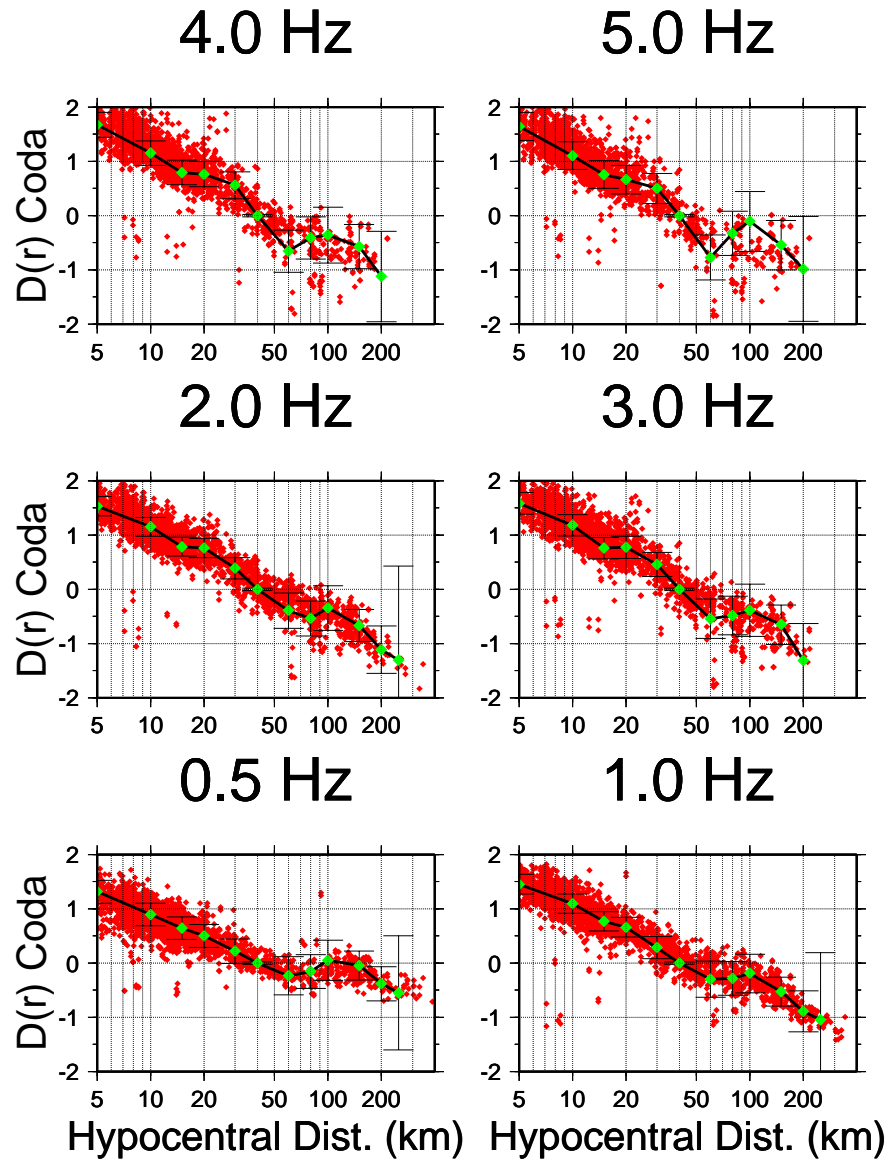
Figure 3.8: Results of L_1 regressions over the reduced amplitude data (red -gray- small diamonds) at the frequencies indicated above each frame. Green (light gray) large diamonds represent the inverted values of the coda estimate of $D(r, f)$ at the nodal locations. Between each nodal point, the attenuation function is computed by a linear interpolation. The distribution of the raw data is affected by large and numerous outliers. For this reason we chose to use a L_1 minimization algorithm. Note that the attenuation functional is normalized to zero at the reference distance of 40 km. Error bars shown in the picture have been computed by using a least-squares algorithm.

4.0 Hz

5.0 Hz

2.0 Hz

3.0 Hz

0.5 Hz

1.0 Hz
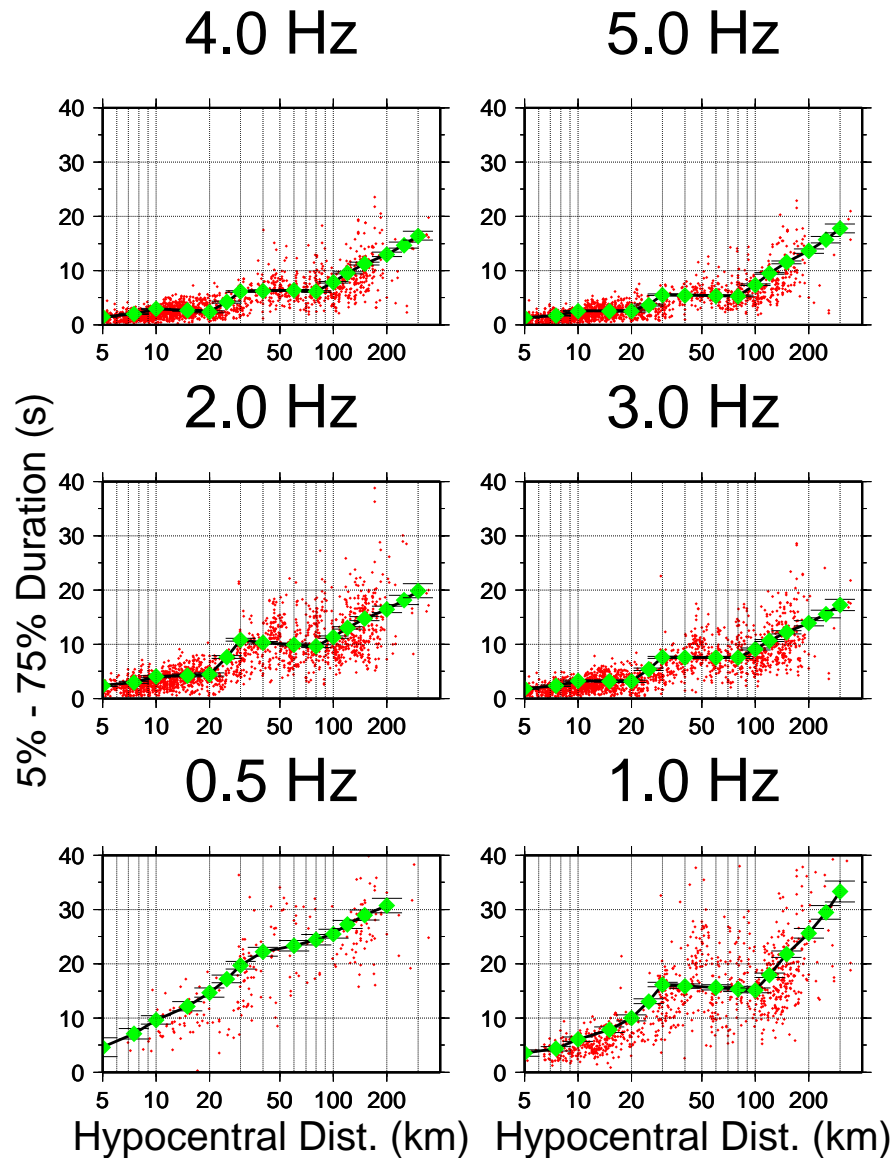
Figure 3.9: 5-75% duration distribution for the regional data at different frequencies. The x-axes refer to hypocentral distance (km), and the y-axes to duration (s). Duration is computed as the time window comprising 5-75% of the seismic energy recorded by the specific station. Red (dark) small diamonds indicate individual values of duration. Green (light gray) diamonds indicate the values of duration computed at a set of nodes, by using a L_1 inversion; the associated error bars are computed by using a least-squares algorithm.

Apennines Attenuation Functional

f (Hz)	r (km)	$D(r,f)$	σ	Nobs	f (Hz)	r (km)	$D(r,f)$	σ	Nobs
	5	0.492	0.041	304		5	0.797	0.036	304
	10	0.288	0.032	667		10	0.531	0.028	667
	15	0.157	0.027	450		15	0.328	0.023	448
	20	0.068	0.024	252		20	0.202	0.021	251
	30	0.014	0.020	250		30	0.068	0.017	247
	40	0.000	0.017	196		40	0.000	0.015	193
	50	0.006	0.040	206		50	-0.015	0.035	200
	60	-0.001	0.042	211		60	-0.035	0.036	208
	70	-0.022	0.043	128		70	-0.077	0.037	129
0.25	80	-0.070	0.044	160	0.40	80	-0.133	0.038	164
	90	-0.151	0.047	109		90	-0.211	0.041	108
	100	-0.209	0.050	214		100	-0.259	0.043	209
	120	-0.233	0.054	231		120	-0.300	0.047	233
	140	-0.273	0.068	288		140	-0.362	0.060	291
	180	-0.376	0.077	172		180	-0.479	0.068	175
	200	-0.490	0.108	37		200	-0.607	0.089	37
	230	-0.602	0.141	18		230	-0.721	0.113	21
	260	-0.730	0.190	13		260	-0.833	0.152	17
	300	-0.881	0.236	9		300	-0.949	0.193	11
	5	0.679	0.038	304		5	0.948	0.033	304
	10	0.445	0.029	667		10	0.640	0.026	667
	15	0.268	0.024	449		15	0.423	0.021	448
	20	0.157	0.022	252		20	0.268	0.020	249
	30	0.047	0.018	250		30	0.094	0.016	248
	40	0.000	0.016	194		40	0.000	0.014	195
	50	-0.003	0.037	199		50	-0.028	0.033	200
	60	-0.013	0.038	208		60	-0.050	0.034	207
	70	-0.045	0.039	128		70	-0.096	0.035	128
0.33	80	-0.096	0.040	165	0.50	80	-0.157	0.036	164
	90	-0.181	0.042	108		90	-0.217	0.038	107
	100	-0.236	0.045	207		100	-0.253	0.040	211
	120	-0.269	0.049	234		120	-0.300	0.044	233
	140	-0.317	0.062	289		140	-0.374	0.054	290
	180	-0.438	0.070	173		180	-0.500	0.062	175
	200	-0.576	0.094	36		200	-0.625	0.080	39
	230	-0.684	0.120	19		230	-0.734	0.101	24
	260	-0.777	0.164	16		260	-0.833	0.138	19
	300	-0.874	0.206	10		300	-0.933	0.165	12

Table 3.1: Attenuation functional at 0.25, 0.33, 0.4 and 0.5 Hz. The columns give values of frequency (first and sixth columns), hypocentral distance (second and seventh columns), attenuation (third and eighth columns), associated error bar (fourth and nineth columns), and number of observations (fifth and tenth columns).

Apennines Attenuation Functional
f (Hz)	r (km)	$D(r,f)$	σ	Nobs	f (Hz)	r (km)	$D(r,f)$	σ	Nobs
	5	1.386	0.029	304		5	1.667	0.030	304
	10	0.997	0.022	667		10	1.173	0.023	667
	15	0.709	0.019	448		15	0.807	0.019	446
	20	0.480	0.017	250		20	0.583	0.017	249
	30	0.194	0.014	251		30	0.277	0.014	251
	40	0.000	0.012	200		40	0.000	0.012	198
	50	-0.081	0.028	199		50	-0.157	0.029	202
	60	-0.122	0.029	206		60	-0.256	0.030	211
	70	-0.188	0.030	129		70	-0.333	0.030	132
1.00	80	-0.274	0.030	167	3.00	80	-0.442	0.031	173
	90	-0.332	0.032	111		90	-0.569	0.033	114
	100	-0.393	0.034	214		100	-0.707	0.035	215
	120	-0.482	0.037	239		120	-0.895	0.038	239
	140	-0.605	0.045	293		140	-1.139	0.046	293
	180	-0.751	0.051	176		180	-1.418	0.052	177
	200	-0.895	0.066	45		200	-1.650	0.064	47
	230	-1.024	0.083	33		230	-1.852	0.080	37
	260	-1.167	0.113	22		260	-2.074	0.114	22
	300	-1.335	0.140	13		300	-2.363	0.164	14
	5	1.554	0.029	304		5	1.742	0.031	304
	10	1.095	0.022	667		10	1.211	0.024	667
	15	0.764	0.018	445		15	0.816	0.020	445
	20	0.544	0.016	249		20	0.587	0.018	250
	30	0.243	0.014	251		30	0.278	0.015	251
	40	0.000	0.012	198		40	0.000	0.013	199
	50	-0.137	0.027	200		50	-0.165	0.030	202
	60	-0.209	0.028	211		60	-0.278	0.031	210
	70	-0.279	0.029	130		70	-0.366	0.031	131
2.00	80	-0.375	0.030	171	4.00	80	-0.489	0.032	173
	90	-0.475	0.031	113		90	-0.632	0.034	114
	100	-0.590	0.033	215		100	-0.790	0.036	215
	120	-0.736	0.036	239		120	-1.006	0.039	239
	140	-0.927	0.044	292		140	-1.287	0.049	287
	180	-1.135	0.050	175		180	-1.598	0.055	173
	200	-1.332	0.062	49		200	-1.838	0.071	44
	230	-1.519	0.077	37		230	-2.043	0.091	32
	260	-1.725	0.103	19		260	-2.276	0.129	19
	300	-1.956	0.151	15		300	-2.584	0.175	11

Table 3.2: Attenuation functional at 1.0, 2.0, 3.0 and 4.0 Hz. The columns give values of frequency (first and sixth columns), hypocentral distance (second and seventh columns), attenuation (third and eighth columns), associated error bar (fourth and nineth columns), and number of observations (fifth and tenth columns).

f (Hz)	r (km)	$D(r,f)$	σ	Nobs
Apennines Attenuation Functional				
	5	1.805	0.032	304
	10	1.259	0.025	667
	15	0.845	0.020	445
	20	0.596	0.018	249
	30	0.279	0.015	249
	40	0.000	0.013	199
	50	-0.169	0.031	202
	60	-0.300	0.032	210
	70	-0.391	0.032	131
5.00	80	-0.524	0.033	173
	90	-0.689	0.036	113
	100	-0.871	0.038	213
	120	-1.107	0.041	235
	140	-1.407	0.052	288
	180	-1.740	0.058	175
	200	-1.981	0.078	45
	230	-2.156	0.101	29
	260	-2.339	0.141	15
	300	-2.588	0.204	7

Table 3.3: Attenuation functional at 5.0 Hz. The columns give values of frequency (first column), hypocentral distance (second column), attenuation (third column), associated error bar (fourth columns), and number of observations (fifth column).

3.3.4 Regional Attenuation

Tables 3.1, 3.2 and 3.3 give the numerical results of our regression on the regional attenuation functional for the Apennines. They give, for each frequency and distance, the corresponding value of $D(r)$, of its associated uncertainty, as well as the number of observations available at the specific distance (within each distance bin).

Figure 3.10 shows the comparison between synthetic and empirical estimates of the attenuation relationships at all the sampled frequencies, for the peak amplitudes of the filtered time histories. The black lines in Figure 3.10 represent our theoretical prediction of the $D(r, f)$ functional at the various frequencies. The curves are sensitive to the functional form of $g(r)$, to the quality factor, and to its frequency dependence, $Q(f) = Q_0 f^\eta$. More specifically, the separation between the different curves at a fixed distance
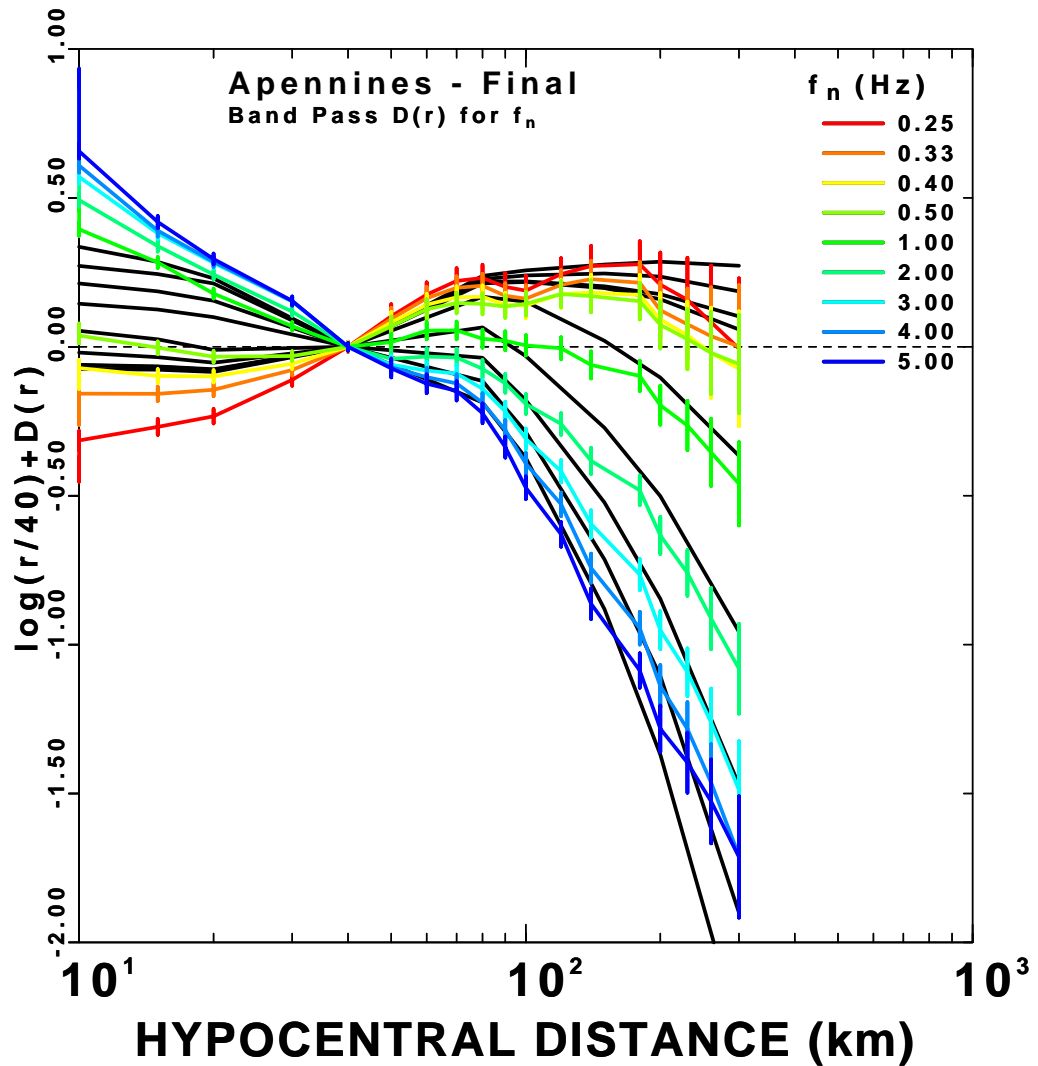
Figure 3.10: Attenuation functional $D(r, f)$ obtained from the regression on the peak values of th e filtered velocities at the sampling frequencies of 0.25, 0.33, 0.4, 0.5, 1.0, 2.0, 3.0, 4.0, 5.0 Hz (color -tone of gray-lines). The attenuation functional has been normalized to zero at a reference hypocentral distance of 40 km. The black lines in the background describe our theoretical predictions of the attenuation relationships based on a simple attenuation model and the application of the RVT (see text for details).

gets larger as η decreases; the curves would lie on top of each others if $\eta = 1$. Also, curves get steeper for lower Q's. Since high frequencies attenuate with distance more severely than low frequencies, $\eta < 1$. Figure 3.10 is insensitive to the choice of κ_0, because of the normalization of the curves at the reference distance. Although the modeling of the empirical attenuation functional has been done only for the peak amplitude data, the same set of parameters must be used to model the Fourier amplitudes. We used $Q_0 = 130$, $\eta = 0.10$ and

$$g(r) = \begin{cases} r^{-0.9} & r \leq 30\text{km} \\ r^0 & 30 \leq r \leq 80\text{km} \\ r^{-0.5} & r \geq 80\text{km} \end{cases}$$

Note that the plot in the figure are normalized to a r^{-1} geometrical spreading for clarity. Thus the function

$$\log\left(\frac{r}{40}\right) + D(r)$$

is plotted. The horizontal dashed line in the picture represents a decay proportional to r^{-1}. This representation provides a way of comparing our results with the assumption of constant decay ($\propto r^{-1}$) and of no anelastic attenuation, which was used by SP87 and SP96.

Site Terms

As a by-product of the final regression, we obtain the source and site terms for each sampled frequency, which allow us to check the stability of the final part of the signal processing.

Site terms for all the available sites for the regression over the peak values, except for those from the Massa Martana campaign, are shown

Colfiorito
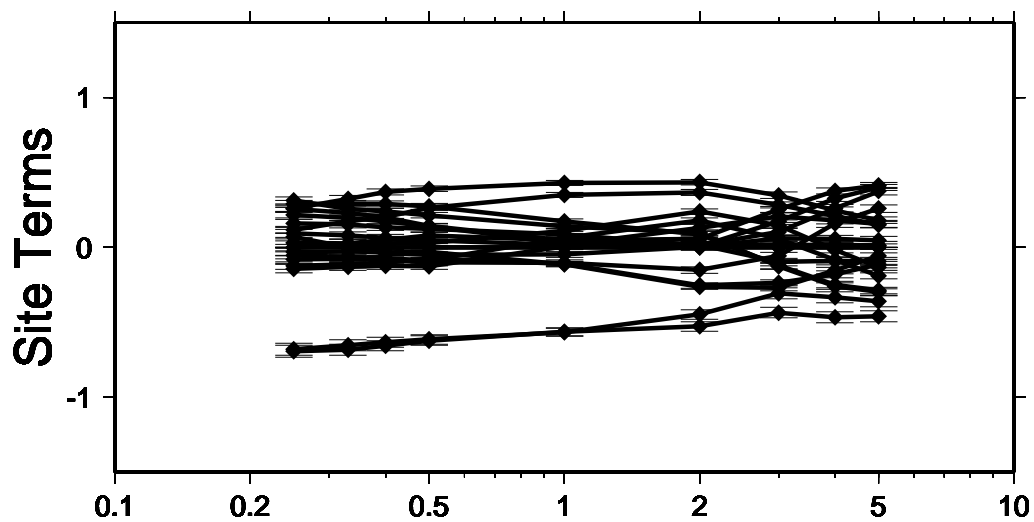
Transects
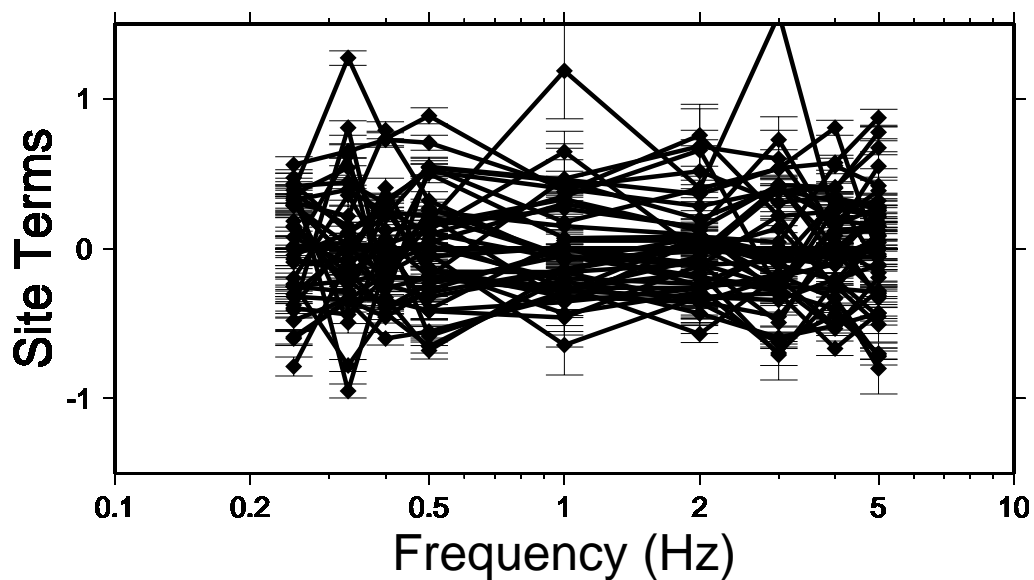
Figure 3.11: Inverted site terms for the entire Italian dataset. Although the inversion was simultaneously run on the complete set of seismograms, we preferred to show the site terms divided in two groups: the sites that recorded the Colfiorito seismic sequence of 1997, and the ones distributed over the three teleseismic transects. The two **MedNet** site terms are shown in the "Transect" frame.

in Figure 3.11. Notice that these site terms represent deviations from the network average. The Colfiorito site terms agree with each other very well since almost all stations were deployed at similar sites.

Excitation Terms

Although the inversion was run simultaneously on the complete data set, we preferred to show the excitation terms divided in two groups: Figures 3.12 and 3.13 show the excitation terms obtained from the regressions on the peak amplitudes (black thin curves) over the entire dataset. Because of the normalization of the regional attenuation functional at the reference distance of 40 km, these terms represent the expected level of motion at 40 km. Superimposed (thick red -gray- curves) are the theoretical predictions of the same excitation terms at the same reference distance, for various moment magnitudes (M_w =2.0, 3.0, 4.0, 5.0, 6.0). The thick red (gray) lines are produced by using the spectral earthquake model by Boore and Joyner (1997) for southern California, and the excitation is propagated to the reference distance by using a geometrical spreading and the two high-frequency attenuation filters:

$$e^{-\frac{\pi f}{V Q_S(f)} r} \exp\left[-\pi \kappa_0 f\right]$$

By matching the spectral shapes at high frequency in this pictures we find that $\kappa_0 = 0.00$. The single-corner frequency spectral model by Boore and Joyner (1997) is characterized by a 70 bar stress drop. Finally, in Figure 3.14, we show the residuals of the general regression.
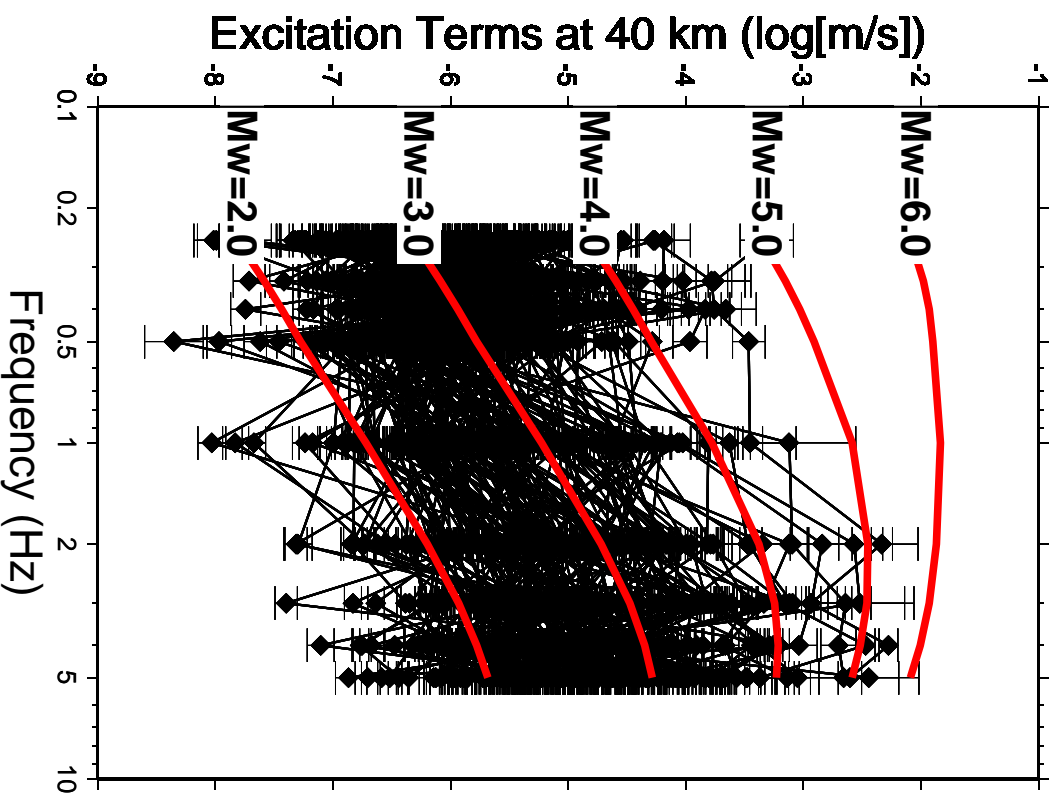
Figure 3.12: Inverted excitation terms for the events recorded by the three teleseismic transects, compared to predictions using southern California source model and regional propagation.
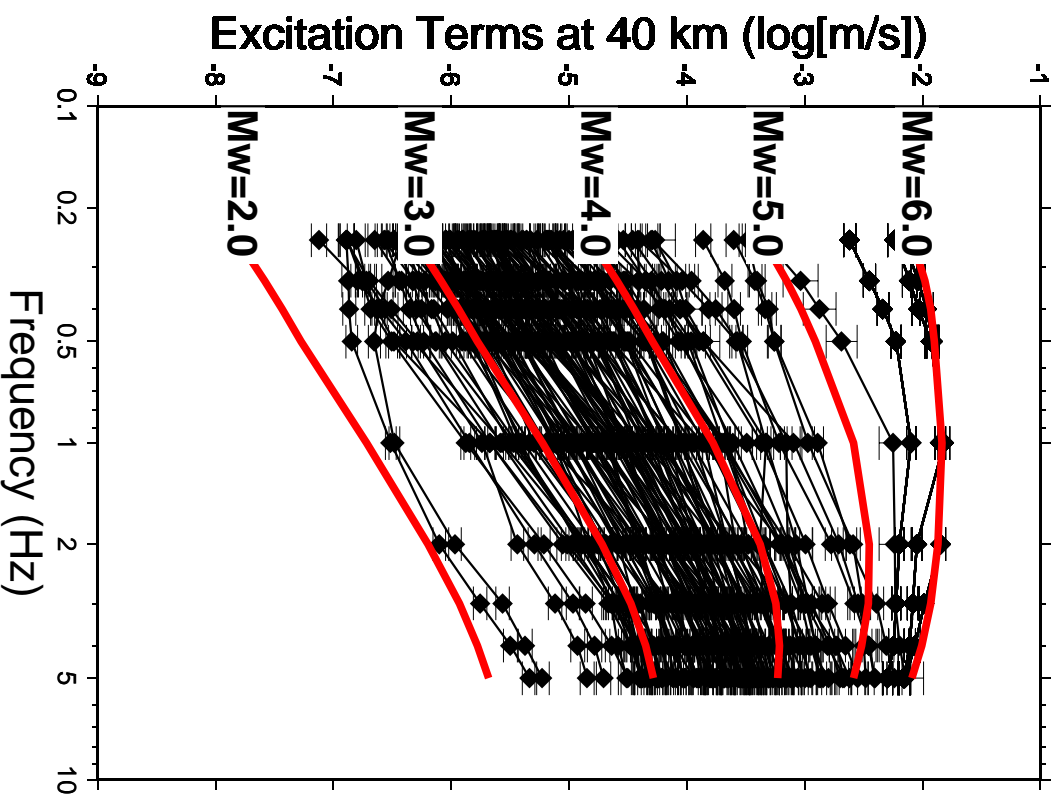
Figure 3.13: Inverted excitation terms for the events recorded during the Colfiorito sequence in 1997, compared to predictions using southern California source model and regional propagation.
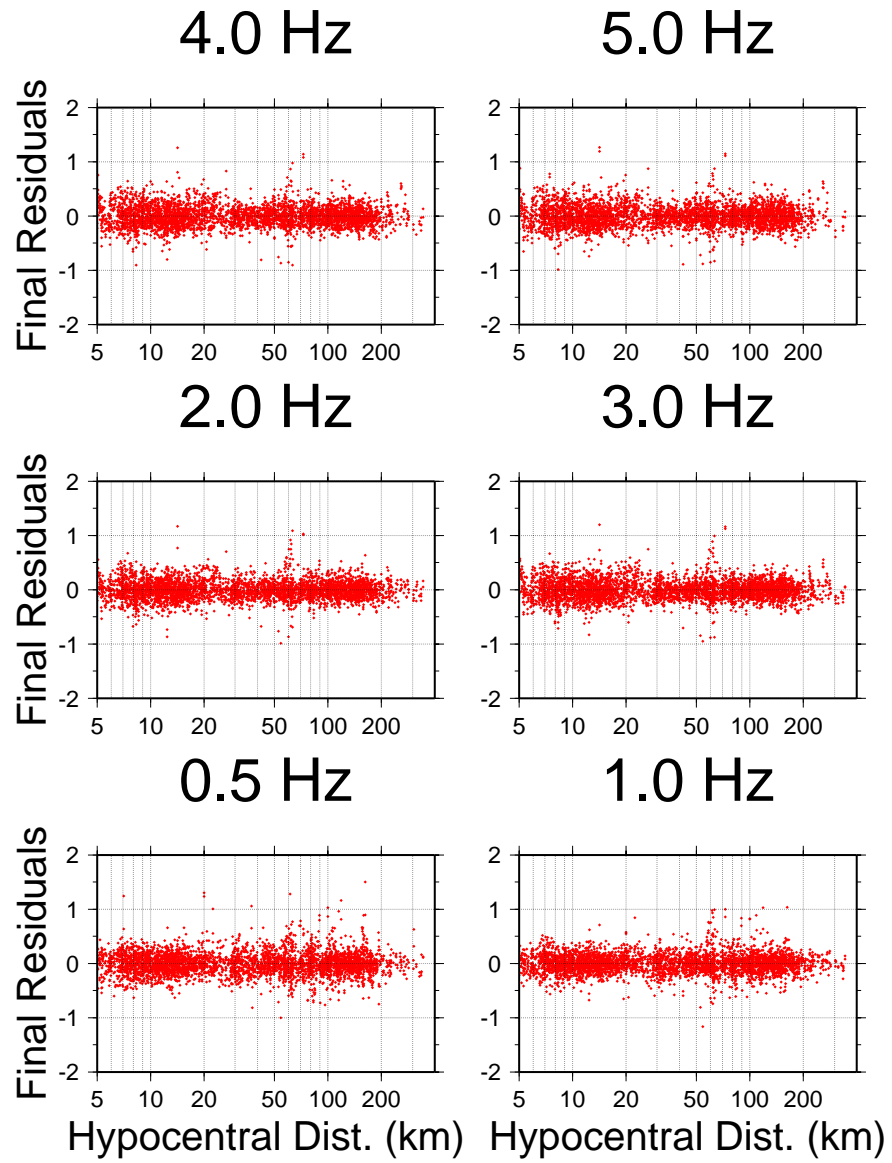
Figure 3.14: Final residuals computed at 0.5, 1.0, 2.0, 3.0, 4.0 and 5.0 Hz.

3.3.5 Comparison with the coda normalization results

Figure 3.15 compares the attenuation functional obtained from the final regression to its estimate computed by using only the coda normalization technique. The figure indicates that the coda normalization technique represents a good tool for the empirical determination of the attenuation functional in a region. What makes this technique very helpful is that its use is not subordinated to the availability of well-calibrated recordings.

3.3.6 Comparison with Southern California

Since ground motion scaling of southern California represents a standard for ground motion studies applied to other active regions lacking of a significant strong motion accelerogram data base, we compare the results of the regressions on the attenuation of the filtered velocities published by Raoof et al. (1999) to ours. Other than some minor differences of the two datasets, the procedure applied in the two cases was virtually identical. Figure 3.16 compares the Italian $D(r, f)$ (red -dark gray- diamonds) to the southern Californian results (green -light gray- diamonds). The attenuation functionals from the two regions are very similar at 0.5 and 1.0 Hz; in all other cases the differences are significant, with a more rapid attenuation in Italy at higher frequencies.

The use of empirical relationships developed in southern California must be discouraged even for estimating the magnitude of an earthquake from the duration of the ground motion. The reason for this is discussed in a later section.
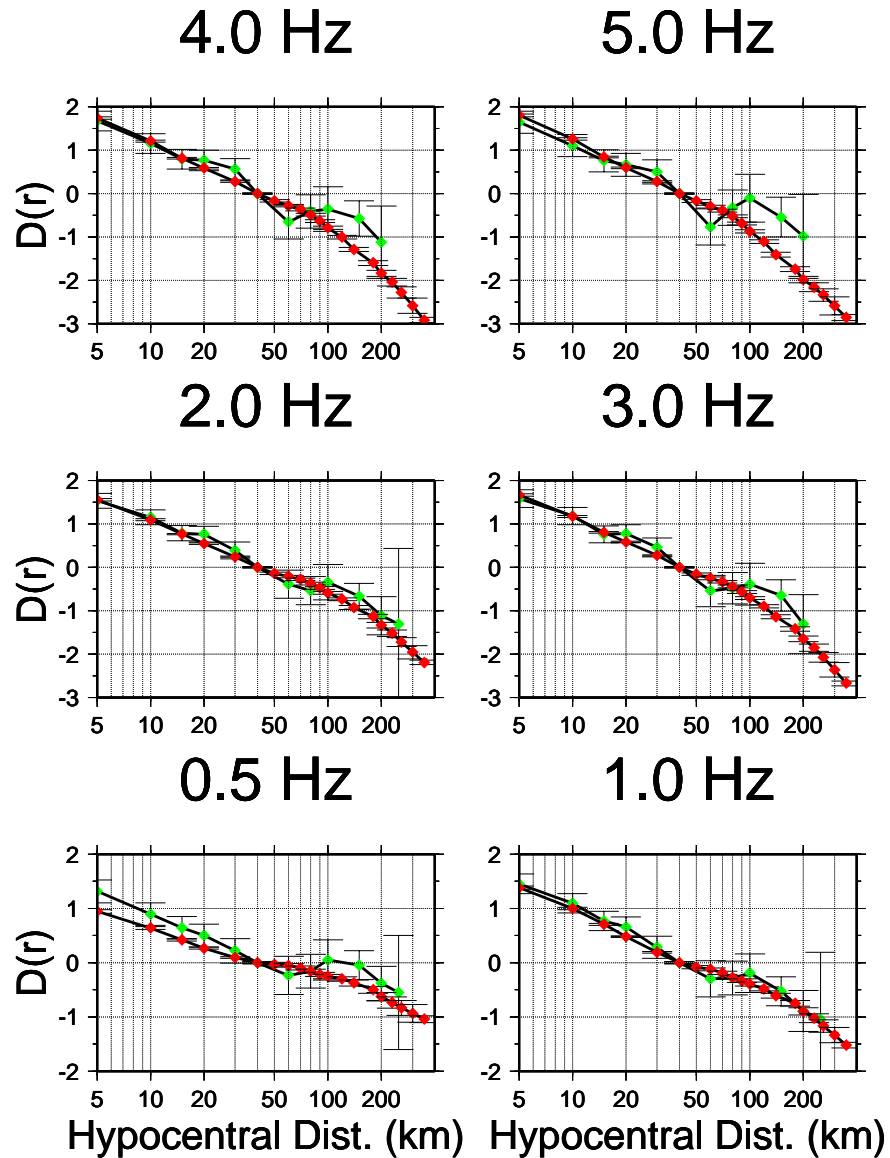
Figure 3.15: Comparison between the attenuation functional obtained from the general regression (red -dark gray- diamonds), and its estimate computed by using the coda normalization technique (green -light gray- diamonds). The six frames in this picture show the comparison at the frequencies of: 0.5, 1.0, 2.0, 3.0, 4.0 and 5.0 Hz.
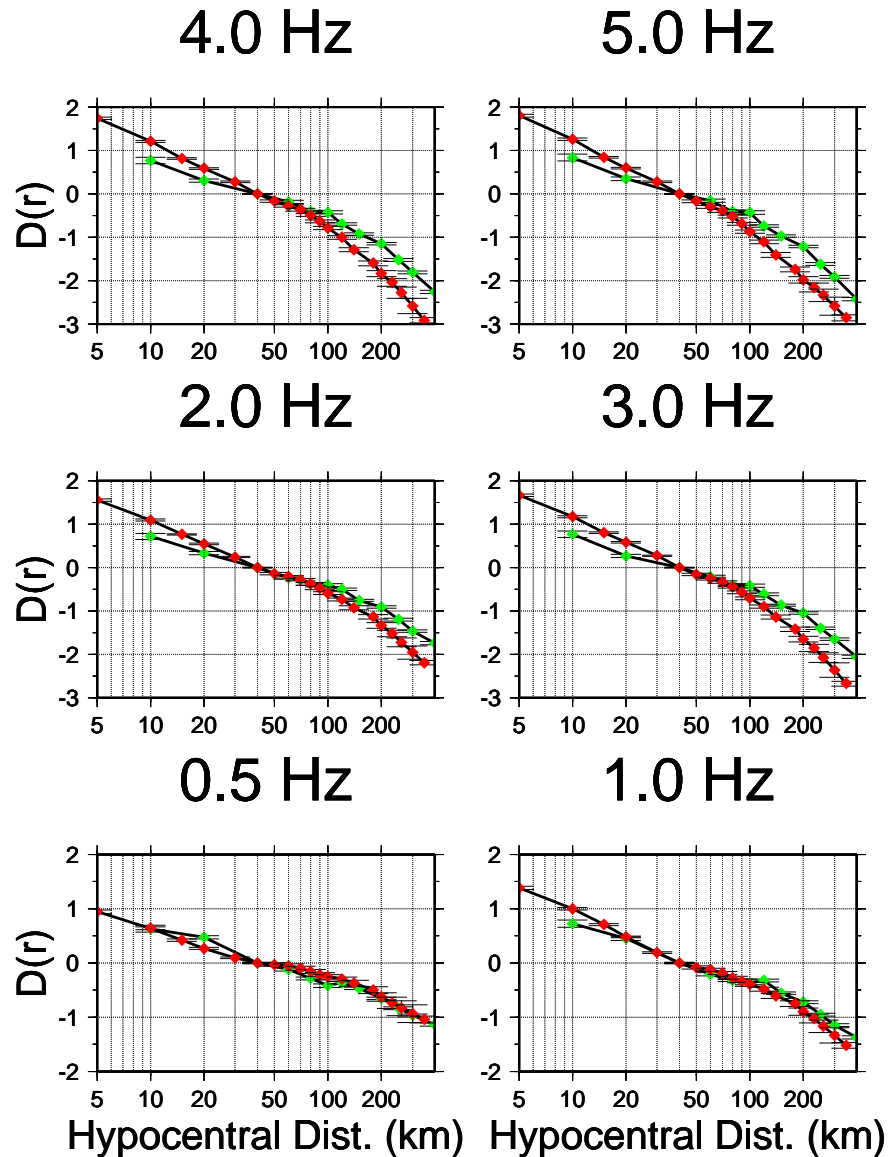
Figure 3.16: Comparison between the attenuation functional computed for the Apennines (red -gray- diamonds) and the one provided by Raoof et al. (1999) for southern California (green -light gray- diamonds). The comparison is made because southern California is often used as a reference standard, for what concernes the prediction of the ground motion. From this picture we see that there is a similar behavior at 0.5 and 1.0 Hz, whereas at higher frequencies the two regions show substantially different attenuation curves.

3.4   Fourier Amplitude Spectra

An attempt to automatically evaluate the Fourier amplitude spectra was carried out on the individual waveforms. For each time history, for each frequency, the duration of the time window used for the computation of the RMS spectral average was evaluated by computing the $5\% - 75\%$ fraction of the seismic energy following the S-waves, on the filtered time histories, at the corresponding central frequencies. The RMS average of the spectrum associated to each time history was computed over a time window of that duration, starting at the S-wave arrival. The RMS average was taken on the Fourier amplitude spectrum, between the corner frequencies of the bandpass filter at the specific central frequency.

Regressions were then attempted over the set of the individual Fourier components, in the same way that has been described for the peak values in the time domain. Unfortunately, since the nature of the noise at the recording sites prevented a correct computation of the signal duration most of the times, we could not repeat the processing carried out for the peak amplitudes. Due to the nature of our approach, though, the same functional dependence used to describe the attenution of the peak amplitudes, as a function of the frequency and hypocentral distance, is expected to describe the distance decay of the Fourier amplitudes at the corresponding sampling frequencies.

3.5   Peak Ground Motion

The RVT has been used to compute the expected peak horizontal acceleration (PHA) and the peak horizontal velocity, on seismic spectra cal-

culated by means of the southern California source model, together with our attenuation and duration functionals. The computer code used for this purpose uses a linear relationship with zero offset to describe the increase of duration with hypocentral distance, and we input an average slope value of 0.06 s/km, based on our duration analysis.

Our estimates of PHA for a moment magnitudes $M_w =$5.0, 6.0 and 7.0, are indicated by 'M99' in Figure 3.17. The Figure compares our results with the regressions of Sabetta and Pugliese (1987), indicated by 'SP87'. The thick segments on the SP87 lines represents the range of distances where strong-motion data were available for the SP87 regressions. It is encouraging to see that the agreement at $M_w = 7$ between our estimates and their results is good, since SP87 could use data in a wide distance range, up to 200 km away from the earthquake. At lower magnitudes the two sets of curves are still in a fairly close agreement within the distance range covered by data in the SP87 study, although the linear curves significantly diverge from ours at long distances.

The PHV's, on the other hand, show a different behavior (see Figure 3.18). At high magnitude ($M = 7$) the SP87 results and our estimates are in fair good agreement at short distances ($r \leq 30$ km), but beyond the first crossover distance of our geometrical spreading, our estimates are significantly higher than the regression curves of SP87. For smaller magnitudes ($M = 5, \ 6$), the two sets of curves are in good agreement, at least within the distance ranges covered by data in the work of SP87.

The differences between our predictions and the empirical observations may be due to two factors: the source spectrum model used for the predictions and the magnitudes used for the empirical regressions. The

PHA (g)
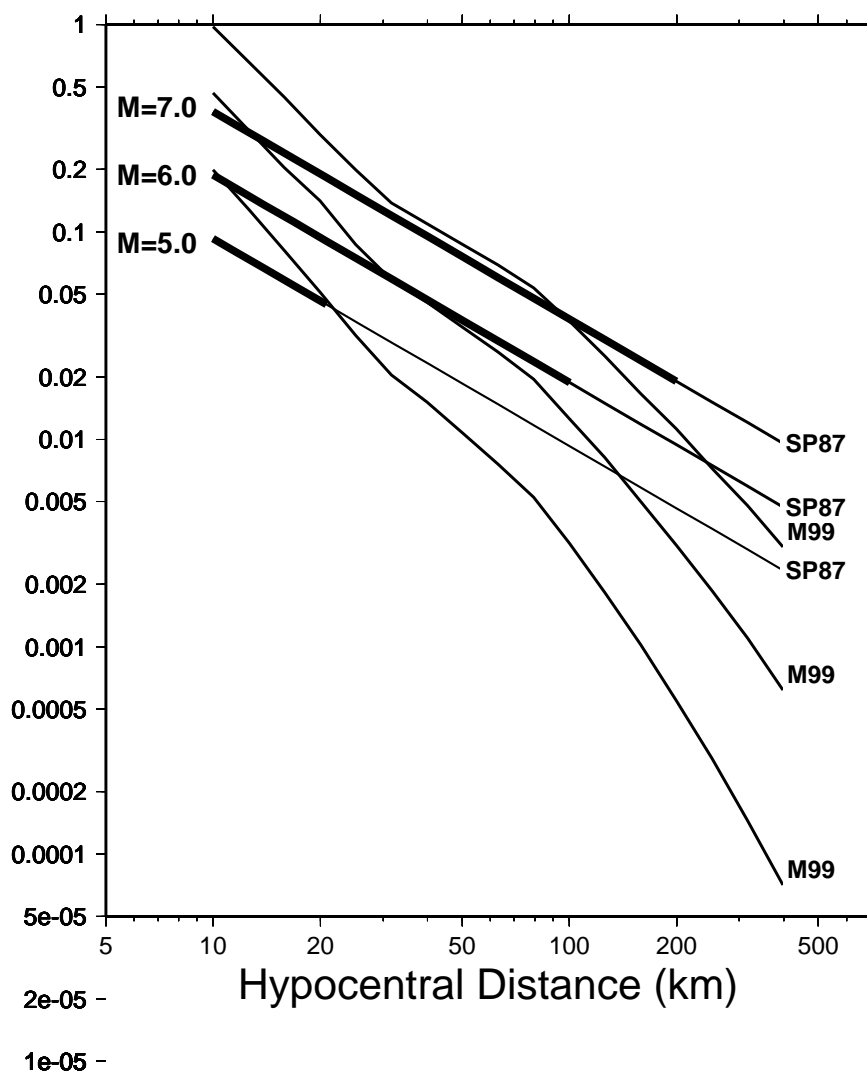
Figure 3.17: Estimates of peak horizontal acceleration based on the attenuation functional obtained in this study, coupled with the spectral model of Boore and Joyner (1997) for southern California (curves marked 'M99'). These are compared with the curves obtained by Sabetta and Pugliese (1987) by regressing peak horizontal acceleration data from strong-motion recordings of earthquakes occurred along the Apennines, in Sicily, and in the Friuli region (northeastern Alps, curves are marked: 'SP87'). The ranges of distance actually covered by the dataset of Sabetta and Pugliese at various magnitudes are indicated on each line by a thick segment. The curves have been extrapolated to large distances by using the formula given by SP87. See text for more details.

magnitude problem is discussed in the next section. The source spectrum model seems inadequate for large earthquakes in the Apennines, and for the lower frequencies controlling the PHV. Thus more work on the scaling of Italian earthquakes is required!

3.6   Magnitude Estimates

Since the beginning of our work, we noticed a systematic divergence between the duration magnitudes estimated routinely at ING and the corresponding amplitude levels of our excitation terms. For example, the upper limit for the magnitude distribution of the 1996 data used in this paper was $M_{dING} = 3.8$ for an event of October 10, 1996, at 19:14 UT, which was listed as a $m_b = 4.6$ in the NEIC catalog. For this event, our amplitude level is agrees with the NEIC magnitude (see Figure 3.19).

It is well known that duration magnitudes are systematically lower than moment magnitudes above a certain threshold, when durations are observed on the output of short-period seismometers. The shift of the corner frequency for increasing earthquake size, coupled with the instrument response of short-period seismometers, leads to saturation for M_d for large earthquakes (Herrmann, 1975). Giardini et al. (1997) calibrated regression curves commonly used for earthquakes within the Mediterranean region, and concluded that the duration magnitude M_D used by most seismic networks requires accurate station calibration and should be restricted only to events with low seismic moment.

For the events in our data set, we noticed that M_{dING} seriously underestimates the moment magnitudes above $M_w \approx 3.4$. Figures 3.19 and 3.20

PHV (cm/s)
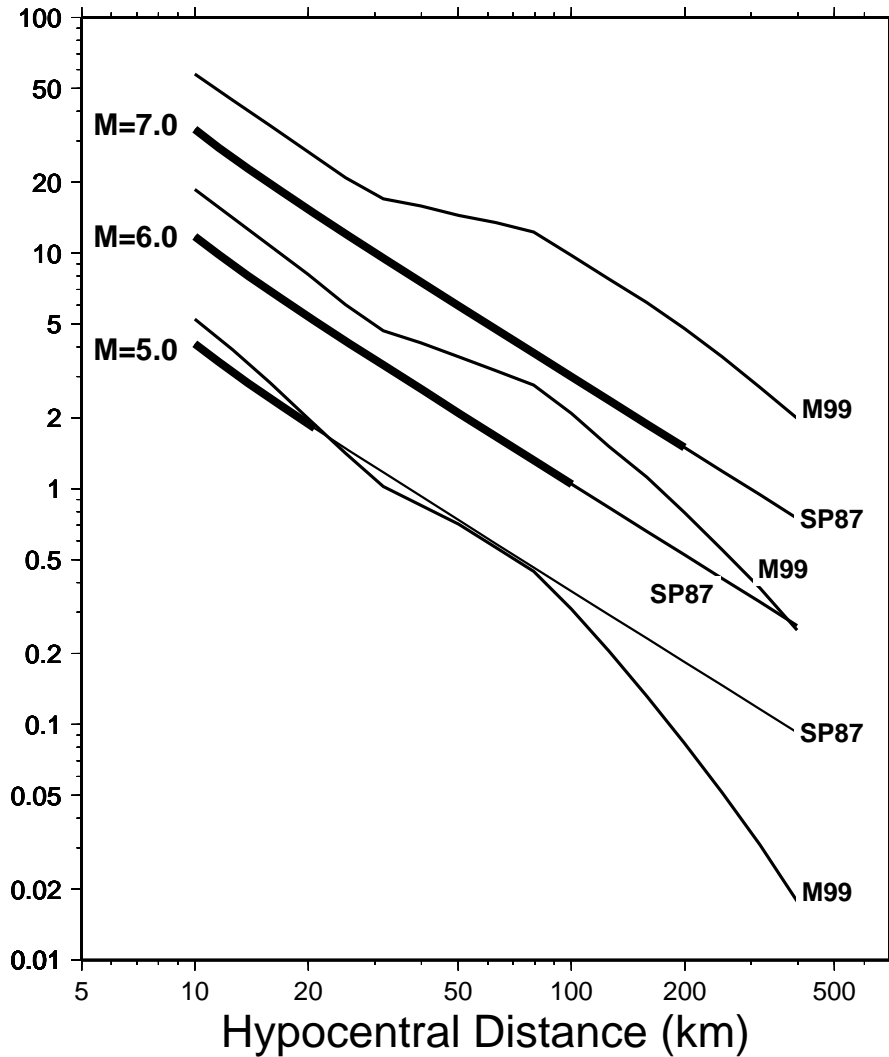
Figure 3.18: Estimates of peak horizontal velocity based on the attenuation functional obtained in this study, coupled with the spectral model of Boore and Joyner (1997) for southern California (curves marked 'M99'). These are compared with the curves obtained by Sabetta and Pugliese (1987) by regressing peak horizontal velocity data from strong-motion recordings of earthquakes occurred along the Apennines, in Sicily, and in the Friuli region (northeastern Alps). Their curves are indicated by 'SP87'. The ranges of distance actually covered by the dataset of Sabetta and Pugliese at various magnitudes are indicated on each line by a thick segment. The curves have been extrapolated to large distances by using the formula given by SP87. See text for more details.

describe our attempt to test our capability of providing correct absolute values of the ground shaking at the reference distance of 40 km. It must be clear that what follows does not provide a new tool for the computation of the magnitude along the Apennines, but just highlights the discrepancy between the magnitudes listed in the Italian earthquake catalog and the corresponding estimates of M_w or m_b. Four earthquakes in our dataset had independent measures of the magnitudes that could be compared with the corresponding M_{dING}'s listed in the ING catalog. The comparison is done in Figure 3.19, where the two upper blue (dark gray) lines show the excitation terms of two events recorded during the Colfiorito seismic sequence, the first on September 26, 1997, at 00:33 UT ($M_w = 5.67$, Ekström et al., 1998), the second at 9:40 UT the same day ($M_w = 6.00$, Ekström et al., 1998). The third blue (dark) curve in the picture is for an event that occurred in the Colfiorito area on September 27, 1997 at 08:08 UT ($M_w = 4.35$, Ekström et al., 1998). The green (light gray) line in Figure 3.19 is relative to an event occurred on April 27, 1996 at 00:38 UT, for which NEIC provided a magnitude $m_b = 4.6$. For this event, ING estimated $M_{dING} = 3.8$. The duration magnitudes provided by ING are indicated in green (light gray) and blue (dark) on the right side of Figures 3.19, according to the color, or tone of gray, of the corresponding line. The values of M_w indicated in blue (dark) and green (light gray) on the left side of the picture are the ones used to compute our theoretical predictions (indicated by the red -gray- lines).

Figure 3.20 shows the computed excitation terms corresponding to two earthquakes, one of which occurred on July 16 1996 at 12:46 UT and the other on July 19, 1996 at 01:20 UT. We obtained a good fit for our excitation amplitudes at 40 km (black lines), by using $M_w = 3.3$ ($M_{dING} = 3.4$).
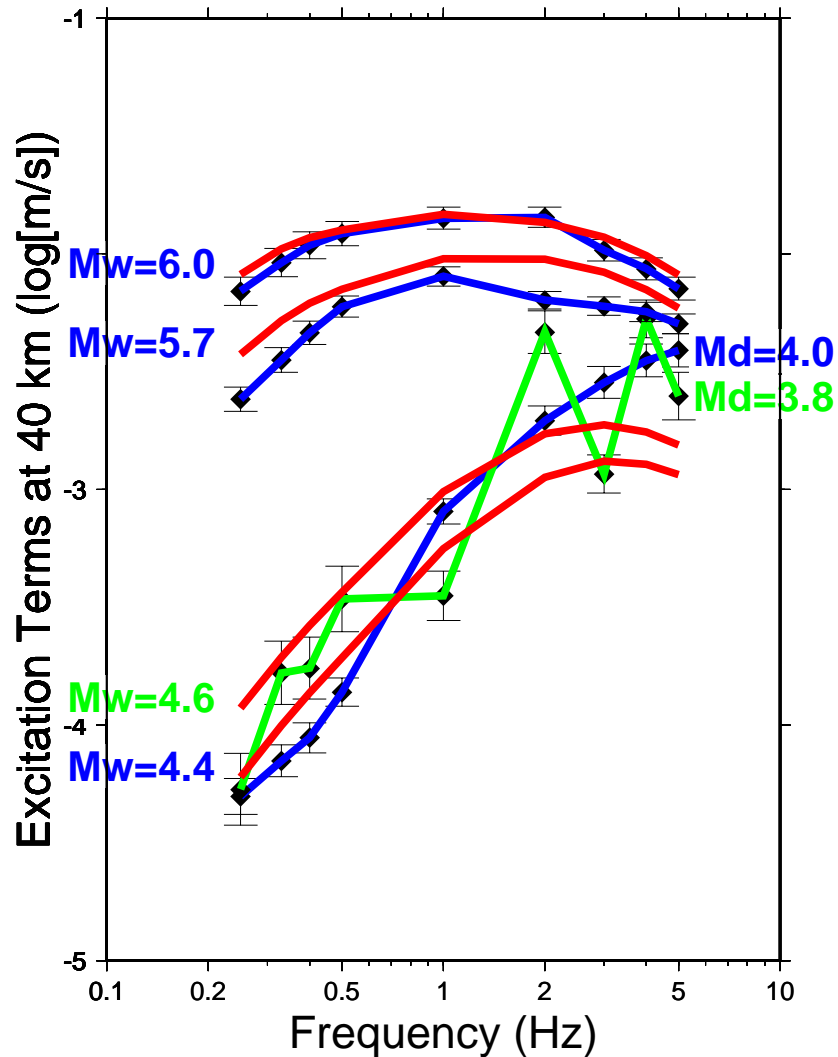
Figure 3.19: This figure shows the excitation terms for which we could find some independent magnitude estimates (from the NEIC catalog, number in green -light gray- on the left side of the picture, and from Ekström et al., 1998, number in blue -dark- on the left side of the picture). The corresponding theoretical predictions computed by using the RPT and the cited, independent magnitude estimates, are also plotted (red -gray- lines). Blue (dark) lines refer to excitation terms for events of the Colfiorito seismic sequence; the green (light gray) line is relative to an event recorded by the 1996 southern Apennies teleseismic transect. On the right side of the picture, in green (light gray) and blue (dark), are the values of M_{dING} for the two low-magnitude events. Notice the substantial difference with the corresponding values of M_w and M_{dING}.
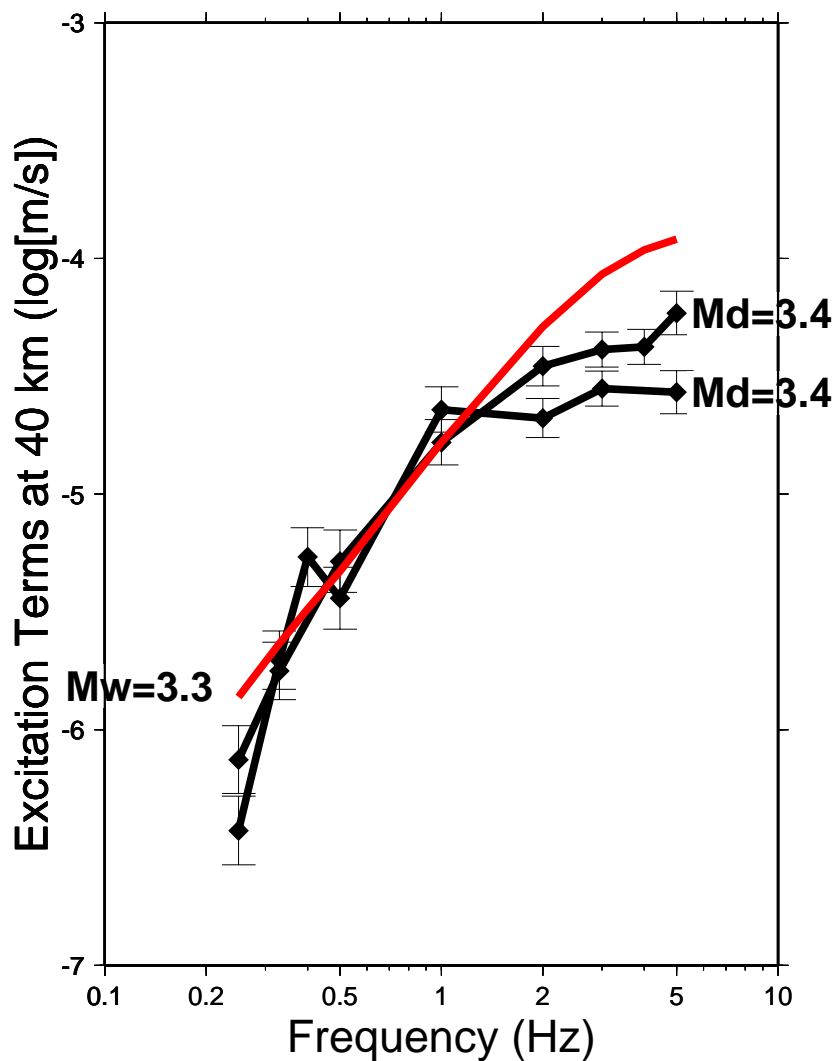
Figure 3.20: The figure shows two excitation terms obtained from our general regression (black lines), with the indication of their duration magnitudes (M_{dING}) on the right side of the picture. The events were recorded by the 1996 southern Apennines teleseismic transect. The red (gray) curve represents a theoretical prediction of the observed excitation terms, relative to a moment magnitude $M_w = 3.3$.

Figure 3.20 indicates that $M_{dING} \sim M_w$, for $M_{dING} < 3.5$, whereas Figure 3.19 shows that M_{dING} underestimates true size for larger events.

The use of duration as a measure of magnitude is described by many authors (Biszticsany, 1958; Sole'vev, 1965; Tsumura, 1967; Lee et al., 1972; Crosson, 1972, Real and Teng, 1973). A general formulation for the duration magnitude can be the following:

$$M_d = p + q \log \left[\tau + s\Delta \right]$$

where τ is the duration of the seismic signal, from the onset of P-waves, and Δ is the epicentral distance. Although quantitatively defined and automatically computed, the durations used at ING to calculate the magnitudes for the seismic catalog are always estimated by the operator on duty, directly on the seismic signal.

Herrmann (1975) noted that for small earthquakes, the "q" parameter is related to the coda envelope shape, which can be written as

$$a(t) = A_0 \left(\frac{\tau}{t_s - t_p} \right)^{-\delta}$$

where

$$\tau = t - t_p.$$

A_0 is proportional to the seismic moment ($A_0 \propto M_0$), especially if small earthquakes are studied, for which the source corner frequency is within or greater than the sensor passband. If the duration τ is defined as

$$\tau = t_{noise} - t_p$$

and t_{noise} is such that

$$a(t_{noise}) = C \cdot a_{noise}$$

where a_{noise} is the noise amplitude, and C is an arbitrary constant, larger than 1. $C = 2$ could be a good choice for observations.

$$a(t_{noise}) \propto M_0 \left(\frac{\tau}{t_s - t_p} \right)^{-\delta}$$

taking the logarithms,

$$\log a(t_{noise}) = \log M_0 - \delta \log \tau + f(r) + \log(a_{noise}) + \text{const}$$

where $f(r) = \delta(t_s - t_p)$ is a function of the hypocentral distance. If we want to use τ to estimate the magnitude of an event, we can use the relationship

$$M_w = \frac{1}{1.5} \log M_0 + \text{const.}$$

(Hanks and Kanamori, 1979) which presumably holds also for events in the Apennines, and write

$$M_d = q \log \tau + \text{const.}$$

where

$$q = \frac{\delta}{1.5}.$$

The coefficient 1.5 derives from the empirical relationships defined by Gutenberg and Richter to relate the seismic energy to the magnitude M_s, see Lay and Wallace, 1995).

For the Italian region, Console et al. (1988) proposed

$$M_{dING} = -0.87 + 2 \log (\tau + 0.00047\Delta).$$

Lee et al. (1972) used the following relationship for California:

$$M_{dING} = -0.87 + 2 \log (\tau + 0.00175\Delta).$$

Figure 3.21 demonstrates that the choice of q (=2.0) made by Console et al. (1988) in the formula for the definition of the duration magnitude is inadequate for the Italian region. The upper frame shows a horizontal time history from the event of April 27, 1996 at 00:38 UT ($m_b = 4.6$). The dotted and dashed lines describe the coda decay function for $\delta = 3.0$ and $\delta = 4.0$, respectively. In the lower frame is shown a log log plot of the absolute values of the time history as a function of time, together with lines proportional to $t^{-3.0}$ (dotted), and $t^{-4.0}$ (dashed).

Although a reevaluation of the duration-magnitude relationship for the Italian region requires a regression on a large dataset, it is clear that the formula of Console et al. (1988) should be reconsidered in the light of this simple example. The new parameter should then be

$$q = \frac{\delta}{1.5} = \frac{4.0}{1.5} \simeq 2.67$$

3.7 Conclusions

We determined empirical attenuation relationships for S- and L_g- waves at regional distances for the peak ground motion along the Apennines. This goal was achieved by performing regressions over a large number of time histories (over 6000 horizontal waveforms), which have been collected in the last five years along the entire Apennines fold-and-thrust belt.

Most of the dataset consists of broadband seismograms from portable local networks, although a small part of it (~ 200 horizontal component waveforms) comes from accelerometric recordings collected during the strongest events of the recent Colfiorito sequence (max magnitude: $M_w = 6.0$).
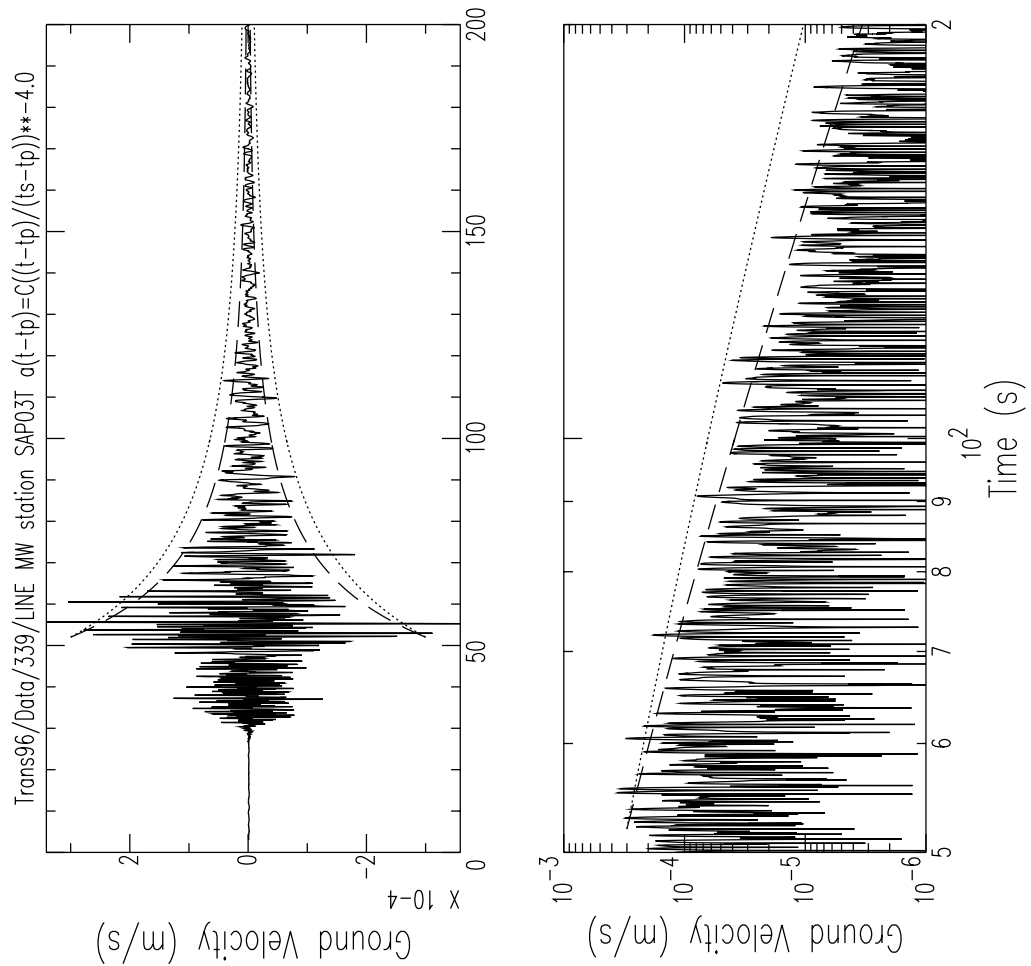
Figure 3.21: The transverse component of ground motion recorded by station SAP3 (southern Apennines Transect, 1996) during the event occurred on April 27, 1996 at 00:38 UT ($m_b = 4.6$) is plotted in the upper frame. The envelope of the seismic signal after the S-wave arrival is outlined by the dashed curves corresponding to an amplitude decay with time proportional to $t^{-4.0}$. The dotted curves represent a decay proportional to t^{-3}, as indirectly assumed to happen in Italy by Console et al. (1988). In the lower frame the absolute values of the horizontal time history are plotted in a log log fashion. Again, the dashed and dotted lines represent the $t^{-4.0}$ and the t^{-3} decays with time (note that the time scales of the two frames are different).

The regressions were performed over the peak amplitudes of the band-pass filtered waveforms over a discrete set of sampling frequencies ($f_n =$ 0.25, 0.33, 0.40, 0.5, 1.0, 2.0, 3.0, 4.0, 5.0 Hz). The result of our effort is a smooth, piece-wise linear estimate of the regional attenuation functional for the peak amplitudes of the filtered ground velocities, computed at the mentioned set of sampling frequencies. The results of our regressions show that the regional scaling for the peak amplitudes is well defined in the Apennines region.

We modeled the S- or L_g-wave empirical attenuation functional as

$$D(r, f) = \log \left[g(r) \exp\left(-\pi \kappa_0 f\right) \exp\left(\frac{-\pi f r}{Q_s(f)V}\right) \right].$$

$g(r)$ was chosen as a tri-linear function a in log log space. Changes of the steepness in the empirical attenuation functional are seen at distances of 30 and 80 km, suggesting that the geometrical spreading factor changes from direct- to surface-wave-type within a transition zone where direct S-waves costructively interfere with intra-crustal reflections and with critically and supercritically reflected S-waves from the Moho. In our parameterization, the anelastic part of the attenuation functional depends on the parameters $Q_S = Q_0 f^\eta$, and on the regional estimate of the parameter κ_0. For the parameters mentioned, our results suggest the following quantities:

$$\kappa_0 = 0.00 \ s$$

and

$$Q_s(f) = 130 f^{0.10}.$$

The anelastic attenuation function is to be coupled with the following ge-

ometrical spreading

$$g(r) = \begin{cases} r^{-0.9} & r \leq 30\text{km} \\ r^0 & 30 \leq r \leq 80\text{km} \\ r^{-0.5} & r \geq 80\text{km} \end{cases}$$

The information carried by each time history about the duration of the significative ground shaking at that particular source-receiver distance were extracted by using the following definition of duration: the width of the time window containing the 5-75% of the cumulative seismic energy behind the S-wave arrival. The duration of the seismic signal in the Apennines were obtained for point sources in time and space. This information is given as a function of distance and frequency.

Our estimate of the parameter κ_0 for the Apennines is quite low, and contrasts with the results of other workers, who observed higher values (Rovelli, 1988; Di Bona, personal communication). This disagreement is due to the tradeoff induced by the use of the southern California spectral model, which is characterized by a stress-drop of only 70 bars, too low for the Italian region.

Another important result is that a low-Q_S crust exists throughout the region. The loss of energy due to anelasticity along regional paths is described by the frequency dependent parameter $Q_S(f) = 130 \cdot f^{0.10}$. As we will see in Chapter 4, the frequency dependence of Q is valid in a broad frequency range (0.25 - 16.0 Hz). The disagreement between our estimate of $Q(f)$ and the ones provided by other studies performed in Italy by Rovelli (1988) and by Del Pezzo et al. (1985), is probably due to the paucity of the datasets used by these authors.

The main implication of this work is that, because of the low-Q_S at all frequencies, high-frequency (1 - 20 Hz) seismic hazard along the Apen-

nines will be dominated by the local seismicity. Nevertheless, exceptions to this rule are likely to occur, due to the existence of important site amplification effects (see, for example, Boschi et al., 1995).

In the future it will be necessary to produce the same results over sets of data collected in the Western and Eastern Alps, and in Sicily. This complex effort will eventually allow us to produce modern hazard maps for the entire Italian territory. A reevaluation of the source parameters for the earthquakes of the Apennines will also be necessary.

In the last section of this paper we demonstrated that the duration-magnitude relationship given by Console et al. (1988) may be inadequate to describe the actual source size away from $M_w \approx 3.4$. Their relationship severely underestimates magnitudes above that threshold, and probably overestimates them below it. For the relation

$$M_d = p + q \log \left[\tau + s\Delta \right]$$

Console et al. (1988) derived a regional estimate of s, the correction to apply to the observed duration at increasing distances, but the parameters p and q were taken *tout-court* from the formula proposed by Lee et al. (1972) for southern California. From a visual inspection of a seismogram, we suggest $q \approx 2.67$ as a possible choice, although a thorough study is needed to properly reevaluate this and the other parameters.

We also showed that the attenuation functional for southern California (a region historically viewed as the reference standard by the Italian seismologists for what concernes studies on ground motion prediction) is substantially different from the Italian attenuation, for frequencies above 1 Hz. For purposes of ground motion prediction along the Apennines, the

Italian seismological community must therefore use only tools calibrated over the Italian region.

4. Ground Motion Scaling in the Umbria-Marche Region (Italy)

4.1 Introduction

One of the most interesting and important results obtained in the previous chapter for the whole Apennines is the functional dependence of the attenuation parameter $Q(f) = 130 \cdot f^{0.10}$ This result is very different from the one obtained by Rovelli et al. (1988), who suggested:

$$Q(f) = 100 \cdot f^{1.0}$$

In Chapter 3, the parameters for the anelastic attenuation were obtained by modeling the results of a regression over a large number of recordings (over 3,000 three-component waveforms) in the 0.25-5.0 Hz band. The waveforms from the Umbria-Marche data set were also part of the data set described in Chapter 3.

Since the Umbria-Marche sequence was recorded at a sample rate of 100 sps by the portable network deployed in Central Italy by ING right after the event of September 26, 1997 at 9:40 GMT, we used the set of locally recorded waveforms to check the validity of the attenuation parameter proposed for the whole Apennines, and of its frequency dependence, over a much broader frequency range (0.5 - 16 Hz). In doing so, we demonstrated that a simple, single form for the attenuation functional is able to model the observed attenuation all along the Apennines, despite the fact that other authors (Castro et al., 1999) indicate substantially different at-

tenuation functionals for the Umbria-Marche region, when compared to other parts of the peninsular Italy.

Since the largest source-receiver distances in the data set are about 40 km, a simple body-wave geometrical spreading is used at all distances for the forward modeling of our results in this chapter:

$$g(r) = r^{-1}.$$

4.2 The Dataset

The Colfiorito (or Umbria-Marche) seismic sequence followed an $M_w = 6.0$ earthquake that occurred on September 26, 1997, 09:40 GMT. The sequence was closely monitored by a local network installed by ING since the first day of activity. The temporal and spatial evolution of the seismicity in the area has been described by Amato et al. (1998). Figure 4.1 shows the locations of the portable seismic stations (blue triangles, black in a b/w reproduction) and of the events used in both the present and the previous chapter (red -gray- circles). All 10 stations were instrumented with RefTek 72a-07 digitizers and CMG40T three-component broadband sensors. Recordings were taken continuously with a 100 Hz sampling rate.

Before processing the data, we removed all waveforms in which multiple events overlapped in time over the coda-wave time window. After this preliminary selection, 142 events were available, for a total of $\sim 1,000$ three-component waveforms.
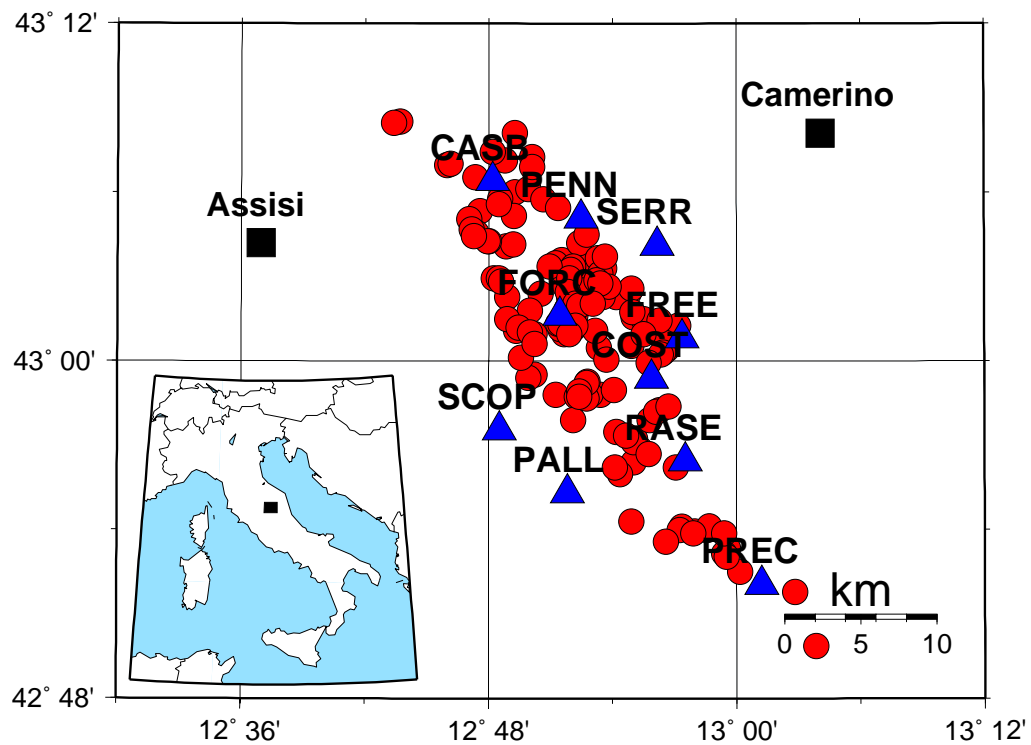
Figure 4.1: Map of the area struck by the Colfiorito earthquake sequence of September-November 1997. The locations of the events used in this study are indicated by red (gray) circles. The stations of the portable seismic network installed by ING to monitor the sequence are indicated by blue (black) triangles.

Colfiorito
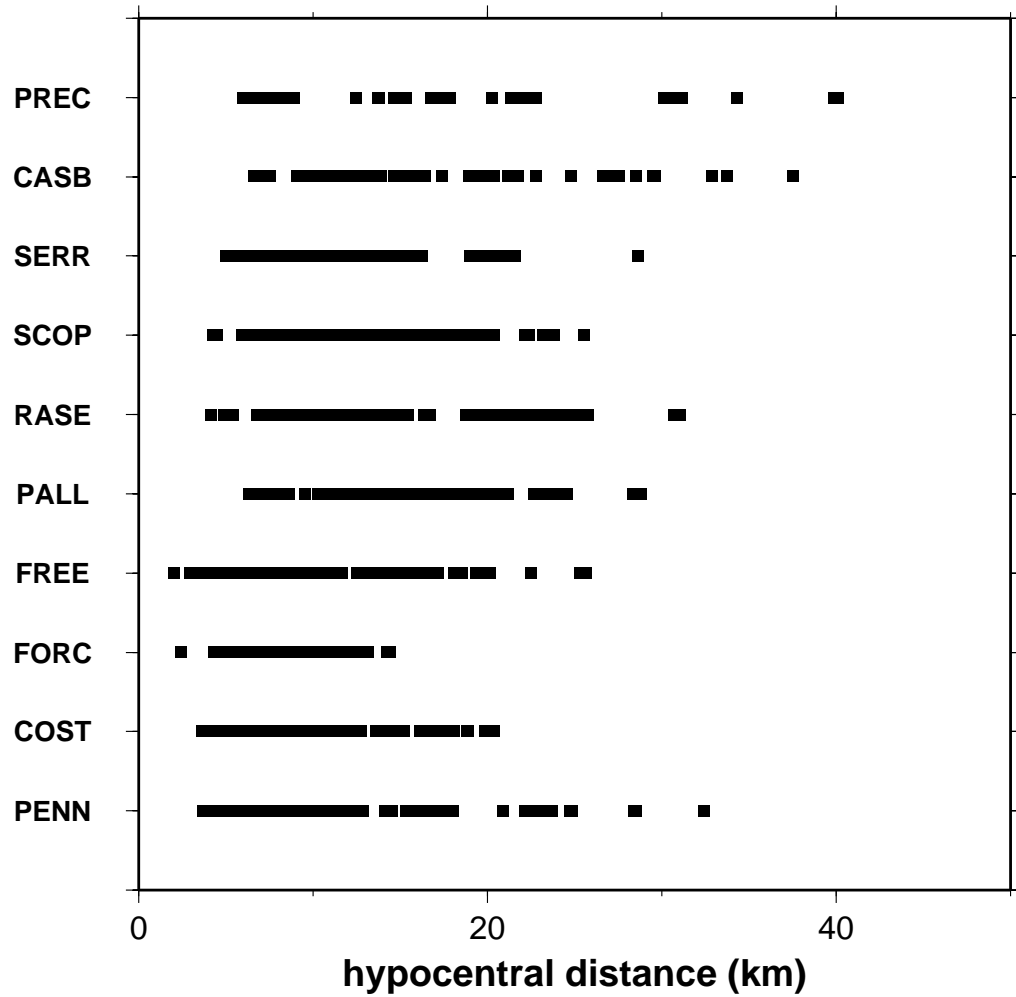
Figure 4.2: Distribution of hypocentral distances available in the Colfiorito data set.

4.3 Data Processing

The procedure for processing the data has been described in detail in the previous chapters, and basically consists of four major stages: filtering, coda normalization analysis, final regression, and forward modeling.

4.3.1 The Bandpass Filters

We decided to proceed with the analysis at the following frequencies: 0.5, 1.0, 2.0, 3.0, 4.0, 5.0, 6.0, 8.0, 10.0, 12.0, 14.0 and 16.0 Hz.

Each time history is narrow bandpass filtered around the sampling frequency f_0. This is done by applying a 8-pole, hi-pass Butterworth filter with a corner at $1/\sqrt{2}f_0$, followed by a 8-pole, lo-pass Butterworth filter with a corner at $\sqrt{2}f_0$. The peak value of each filtered time series is taken as the observed value at the hypocentral distance r, at the frequency f_0.

4.3.2 Coda Normalization Analysis

As seen in the previous chapter, the first step in the data processing is the definition of the coda shape for the investigated region, followed by the normalization of the peak value of each filtered time history to the corresponding RMS value of the seismic coda computed at a specified (arbitrary) reference time.

This procedure will produce an estimate of the attenuation functional at each available hypocentral distance, for each frequency of the chosen set. A L_1-norm misfit minimization, as described in the previous chapter, will provide an estimate of a piecewise linear attenuation functional. The normalization to a zero value of the functional at a reference distance of 10 km ($D(r = 10\text{km}, f) = 0$ produced the results shown in Figure 4.3. Stan-

dard errors plotted in Figure 4.3 were obtained by running a least-squares inversion algorithm on the data set of the normalized peak amplitudes. This hybrid approach is used because the L_1-norm minimization does not allow the computation of the error bars.

4.3.3   Duration of Ground Motion

In order to produce a quantitative prediction of the obtained attenuation functional for the peak filtered velocities, we use Random Vibration Theory (RVT). By using this mathematical tool we are able to compute the peak value of a given time history of duration T, given its RMS (or spectral) value. As described in the previous chapter, the definition of duration of ground motion is defined here as the length of the time window comprising the 5-75% portion of the seismic energy following the S-wave arrival. The computation of the duration of the seismic signals is performed independently for each seismogram and for each frequency.

Figure 4.4 shows the computed durations for all the recordings available, at six of the twelve sampling frequencies. On the basis of the observed duration of the ground shaking as a function of distance, we were able to set up a frequency- and distance-dependent duration functional to be used with the RVT to compute a prediction of the final attenuation functional for the region under investigation.

4.3.4   Regional Attenuation

In this stage of the data processing we are going to proceed with the final regression on the logarithms of the peak filtered velocities. Figure 4.5 shows the results of the regressions on the peak values of the filtered
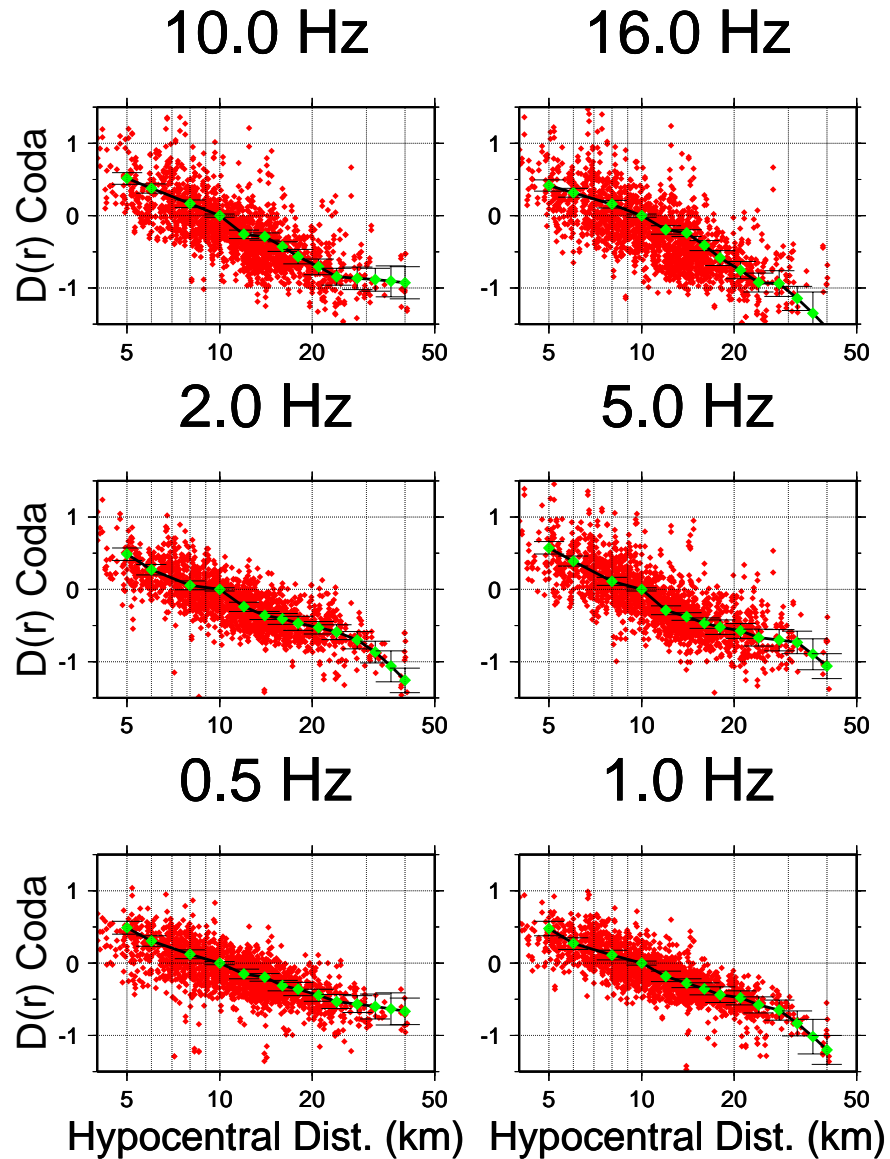
Figure 4.3: Results of the L_1 regressions over the reduced amplitude data (red -gray- small diamonds) at the frequencies indicated above each frame. Green (light gray) large diamonds represent the inverted values of the coda $D(r, f)$ at the nodal locations. Between each nodal point, the attenuation function is computed by a linear interpolation. The distribution of the raw data is affected by large and numerous outliers; for such reason we chose to use a L_1 minimization algorithm. Note that the attenuation functional is normalized to zero at the reference distance of 10 km. The error bars shown in the picture were estimated by using a least-squares inversion algorithm.
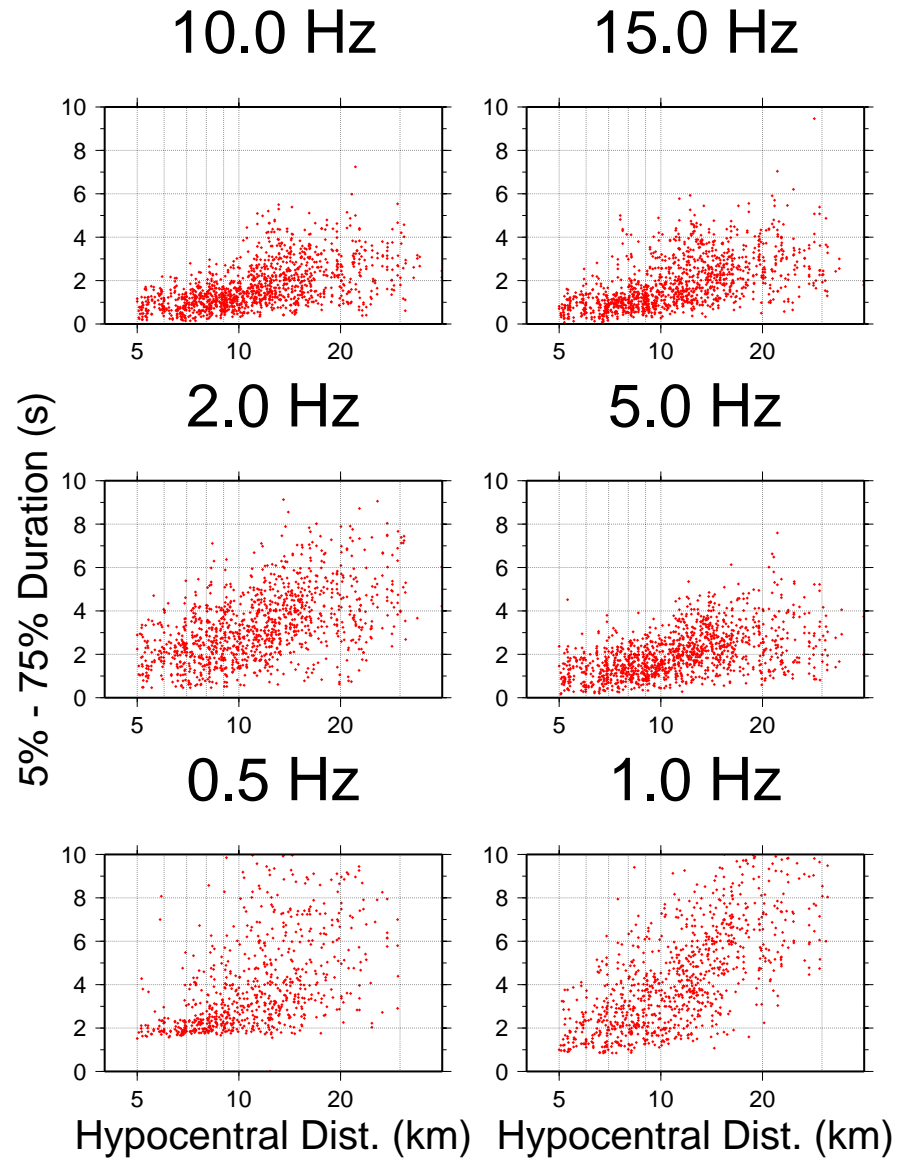
Figure 4.4: 5-75% duration distribution for the regional data at different frequencies. The x-axes refer to hypocentral distance (km), and the y-axes to duration (s). Duration is computed as the time window comprising the 5-75% of the seismic energy recorded on a specific seismogram.

velocities at the sampling frequencies of 0.5, 1.0, 2.0, 3.0, 4.0, 5.0, 6.0, 8.0, 10.0, 12.0, 14.0 and 16.0 Hz (color, or tone of gray, lines). Tables 4.1, 4.2 and 4.3 give the numerical values of the functional plotted in Figure 4.5, as a function of distance and frequency, with the associated uncertainties; the number of observation available at each frequency-distance pair is also given. Note that the attenuation functional has been normalized to zero at a reference hypocentral distance of 10 km. Note that the lines in Figure 4.5 are normalized to r^{-1} (body-wave geometrical spreading). The horizontal dashed line in the picture represents a r^{-1} decay with distance.

The modeling of the empirically estimated attenuation functional for the Umbria-Marche region has been carried out by using the same values of Q_0 and η that were used in the previous chapter to model the attenuation functional obtained from the inversion of the regional data set:

$$Q(f) = 130 \cdot f^{0.10}$$

Since the attenuation functional is normalized to zero at 10 km, there is no effect of κ_0 on Figure 4.5. This parameter will discussed in the next subsection, where it will be used to model the observed excitation terms at the reference distance.

4.3.5 Excitation Terms

In Figure 4.6 the excitation terms obtained from the regression on the peak filtered velocities (black diamonds linked by thin black lines) are plotted at the reference distance of 10 km. The displayed terms refer to all the events used in this study. Thick red (gray) lines indicate the theoretical predictions based on the application of the RVT, at different levels
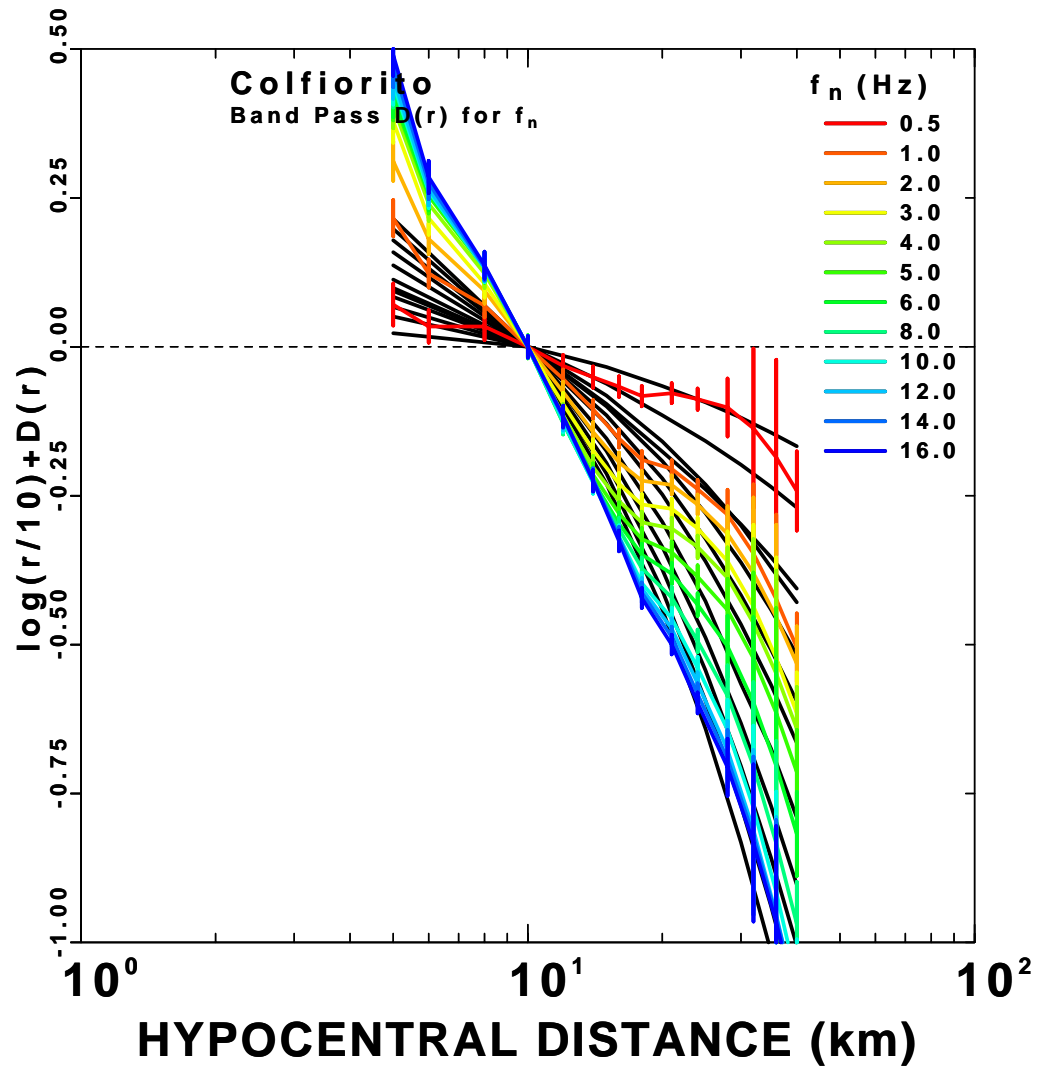
Figure 4.5: The attenuation functional $D(r, f)$ obtained from the regression on the peak values of the filtered velocities, is shown at the sampling frequencies of 0.5, 1.0, 2.0, 3.0, 4.0, 5.0, 6.0, 8.0, 10.0, 12.0, 14.0 and 16.0 Hz (color, or tone of gray, lines). The attenuation functional has been normalized to zero at a reference hypocentral distance of 10 km. The black lines in the background describe our theoretical predictions of the attenuation relationships based on a simple attenuation model, and on the application of the RVT (see text for details).

Umbria-Marche Attenuation Functional

f (Hz)	r (km)	$D(r,f)$	σ	Nobs	f (Hz)	r (km)	$D(r,f)$	σ	Nobs
	5.000	0.372	0.354E-01	61.880		5.000	0.517	0.306E-01	61.880
	6.000	0.256	0.274E-01	196.340		6.000	0.345	0.237E-01	196.340
	8.000	0.131	0.229E-01	345.350		8.000	0.166	0.198E-01	345.350
	10.000	0.000	0.182E-01	307.080		10.000	0.000	0.158E-01	307.080
	12.000	-0.111	0.183E-01	293.150		12.000	-0.133	0.158E-01	293.150
	14.000	-0.197	0.181E-01	250.550		14.000	-0.251	0.157E-01	250.550
	16.000	-0.271	0.176E-01	166.110		16.000	-0.358	0.152E-01	166.110
0.5	18.000	-0.338	0.171E-01	112.473	1.0	18.000	-0.445	0.148E-01	112.473
	21.000	-0.400	0.168E-01	102.213		21.000	-0.527	0.145E-01	102.213
	24.000	-0.468	0.180E-01	61.518		24.000	-0.619	0.155E-01	61.518
	28.000	-0.549	0.487E-01	35.395		28.000	-0.729	0.420E-01	35.395
	32.000	-0.642	0.134E+00	17.270		32.000	-0.852	0.116E+00	17.270
	36.000	-0.742	0.164E+00	3.980		36.000	-0.980	0.142E+00	3.980
	40.000	-0.844	0.666E-01	2.690		40.000	-1.107	0.575E-01	2.690
	5.000	0.613	0.334E-01	61.880		5.000	0.680	0.363E-01	61.880
	6.000	0.403	0.258E-01	196.340		6.000	0.438	0.281E-01	196.340
	8.000	0.191	0.216E-01	345.350		8.000	0.203	0.235E-01	345.350
	10.000	0.000	0.172E-01	307.080		10.000	0.000	0.187E-01	307.080
	12.000	-0.155	0.173E-01	293.150		12.000	-0.175	0.188E-01	293.150
	14.000	-0.289	0.171E-01	250.550		14.000	-0.320	0.186E-01	250.550
	16.000	-0.398	0.166E-01	166.110		16.000	-0.434	0.181E-01	166.110
2.0	18.000	-0.480	0.161E-01	112.473	3.0	18.000	-0.520	0.175E-01	112.473
	21.000	-0.554	0.159E-01	102.213		21.000	-0.594	0.172E-01	102.213
	24.000	-0.645	0.170E-01	61.518		24.000	-0.685	0.184E-01	61.518
	28.000	-0.761	0.461E-01	35.395		28.000	-0.807	0.499E-01	35.395
	32.000	-0.885	0.127E+00	17.270		32.000	-0.941	0.137E+00	17.270
	36.000	-1.010	0.155E+00	3.980		36.000	-1.079	0.169E+00	3.980
	40.000	-1.134	0.628E-01	2.690		40.000	-1.217	0.682E-01	2.690

Table 4.1: Attenuation functional at 0.5, 1.0, 2.0 and 3.0 Hz. The columns give values of frequency (first and sixth columns), hypocentral distance (second and seventh columns), attenuation (third and eighth columns), associated error bar (fourth and nineth columns), and number of observations (fifth and tenth columns).

Umbria-Marche Attenuation Functional									
f (Hz)	r (km)	$D(r,f)$	σ	Nobs	f (Hz)	r (km)	$D(r,f)$	σ	Nobs
	5.000	0.705	0.372E-01	61.880		5.000	0.719	0.378E-01	61.880
	6.000	0.462	0.288E-01	196.340		6.000	0.475	0.293E-01	196.340
	8.000	0.220	0.241E-01	345.350		8.000	0.229	0.245E-01	345.350
	10.000	0.000	0.191E-01	307.080		10.000	0.000	0.194E-01	307.080
	12.000	-0.194	0.192E-01	293.150		12.000	-0.202	0.195E-01	293.150
	14.000	-0.348	0.190E-01	250.550		14.000	-0.361	0.193E-01	250.550
	16.000	-0.463	0.185E-01	166.110		16.000	-0.484	0.188E-01	166.110
4.0	18.000	-0.550	0.180E-01	112.473	5.0	18.000	-0.578	0.183E-01	112.473
	21.000	-0.627	0.177E-01	102.213		21.000	-0.667	0.179E-01	102.213
	24.000	-0.716	0.189E-01	61.518		24.000	-0.766	0.192E-01	61.518
	28.000	-0.835	0.513E-01	35.395		28.000	-0.889	0.521E-01	35.395
	32.000	-0.969	0.141E+00	17.270		32.000	-1.028	0.144E+00	17.270
	36.000	-1.105	0.173E+00	3.980		36.000	-1.171	0.176E+00	3.980
	40.000	-1.243	0.700E-01	2.690		40.000	-1.316	0.711E-01	2.690
	5.000	0.724	0.376E-01	61.880		5.000	0.740	0.372E-01	61.880
	6.000	0.480	0.291E-01	196.340		6.000	0.485	0.287E-01	196.340
	8.000	0.232	0.243E-01	345.350		8.000	0.232	0.239E-01	345.350
	10.000	0.000	0.193E-01	307.080		10.000	0.000	0.189E-01	307.080
	12.000	-0.207	0.194E-01	293.150		12.000	-0.207	0.191E-01	293.150
	14.000	-0.371	0.192E-01	250.550		14.000	-0.373	0.190E-01	250.550
	16.000	-0.501	0.187E-01	166.110		16.000	-0.510	0.186E-01	166.110
6.0	18.000	-0.604	0.182E-01	112.473	8.0	18.000	-0.627	0.181E-01	112.473
	21.000	-0.703	0.179E-01	102.213		21.000	-0.743	0.178E-01	102.213
	24.000	-0.813	0.191E-01	61.518		24.000	-0.874	0.191E-01	61.518
	28.000	-0.950	0.517E-01	35.395		28.000	-1.033	0.511E-01	35.395
	32.000	-1.102	0.143E+00	17.270		32.000	-1.209	0.141E+00	17.270
	36.000	-1.260	0.175E+00	3.980		36.000	-1.390	0.172E+00	3.980
	40.000	-1.420	0.708E-01	2.690		40.000	-1.571	0.707E-01	2.690

Table 4.2: Attenuation functional at 4.0, 5.0, 6.0 and 8.0 Hz. The columns give values of frequency (first and sixth columns), hypocentral distance (second and seventh columns), attenuation (third and eighth columns), associated error bar (fourth and nineth columns), and number of observations (fifth and tenth columns).

Umbria-Marche Attenuation Functional									
f (Hz)	r (km)	$D(r,f)$	σ	Nobs	f (Hz)	r (km)	$D(r,f)$	σ	Nobs
	5.000	0.744	0.364E-01	61.880		5.000	0.753	0.356E-01	61.880
	6.000	0.483	0.281E-01	196.340		6.000	0.487	0.275E-01	196.340
	8.000	0.229	0.235E-01	345.350		8.000	0.230	0.229E-01	345.350
	10.000	0.000	0.186E-01	307.080		10.000	0.000	0.181E-01	307.080
	12.000	-0.204	0.188E-01	293.150		12.000	-0.201	0.183E-01	293.150
	14.000	-0.374	0.187E-01	250.550		14.000	-0.371	0.182E-01	250.550
	16.000	-0.522	0.182E-01	166.110		16.000	-0.524	0.177E-01	166.110
10.0	18.000	-0.652	0.177E-01	112.473	12.0	18.000	-0.661	0.173E-01	112.473
	21.000	-0.778	0.175E-01	102.213		21.000	-0.795	0.170E-01	102.213
	24.000	-0.919	0.187E-01	61.518		24.000	-0.945	0.183E-01	61.518
	28.000	-1.090	0.500E-01	35.395		28.000	-1.124	0.489E-01	35.395
	32.000	-1.279	0.138E+00	17.270		32.000	-1.316	0.134E+00	17.270
	36.000	-1.472	0.169E+00	3.980		36.000	-1.510	0.164E+00	3.980
	40.000	-1.666	0.693E-01	2.690		40.000	-1.705	0.676E-01	2.690
	5.000	0.772	0.352E-01	61.880		5.000	0.791	0.350E-01	61.880
	6.000	0.497	0.273E-01	196.340		6.000	0.507	0.272E-01	196.340
	8.000	0.231	0.228E-01	345.350		8.000	0.234	0.228E-01	345.350
	10.000	0.000	0.181E-01	307.080		10.000	0.000	0.181E-01	307.080
	12.000	-0.197	0.182E-01	293.150		12.000	-0.196	0.181E-01	293.150
	14.000	-0.368	0.180E-01	250.550		14.000	-0.371	0.179E-01	250.550
	16.000	-0.524	0.175E-01	166.110		16.000	-0.530	0.174E-01	165.870
14.0	18.000	-0.668	0.170E-01	112.473	16.0	18.000	-0.677	0.168E-01	111.713
	21.000	-0.809	0.168E-01	101.847		21.000	-0.822	0.165E-01	101.847
	24.000	-0.963	0.180E-01	60.885		24.000	-0.978	0.177E-01	60.885
	28.000	-1.139	0.484E-01	35.395		28.000	-1.153	0.480E-01	35.395
	32.000	-1.326	0.133E+00	17.270		32.000	-1.338	0.132E+00	17.270
	36.000	-1.514	0.163E+00	3.980		36.000	-1.523	0.162E+00	3.980
	40.000	-1.701	0.664E-01	2.690		40.000	-1.707	0.653E-01	2.690

Table 4.3: Attenuation functional at 10.0, 12.0, 14.0 and 16.0 Hz. The columns give values of frequency (first and sixth columns), hypocentral distance (second and seventh columns), attenuation (third and eighth columns), associated error bar (fourth and nineth columns), and number of observations (fifth and tenth columns).

of moment magnitude.

The theoretical prediction of the peak amplitude at frequency f_0 is done by "propagating" the corresponding Fourier amplitude component to the reference distance. The knowledge of the duration expected at that frequency and distance allow the application of the RVT to estimate of the peak value of the filtered time history in the time domain, via the use of the Parseval's equality. The propagation of the spectral components to the desired distances is accomplished by multiplying the theoretical Fourier amplitudes by the quantity:

$$\left(g(r_{ref}) \exp\left[-\frac{\pi f_0}{V Q_0 f_0^\eta} r_{ref} \right] \exp\left[-\pi \kappa_0 f_0 \right] \right)$$

where V is the shear-wave velocity, and

$$g(r_{ref}) = \frac{1}{r_{ref}}.$$

Of course, the parameter κ_0 trades off with the other parameters that characterize the source spectrum. Our estimate of $\kappa_0 = 0.00$ for the Colfiorito area represents the value needed to match the source spectra in this region, given the southern California earthquake spectral model by Boore and Joyner (1997), described in Appendix C, which is used throughout this dissertation. $\kappa_0 = 0.00$ does not represent the high-frequency fall-off parameter of the seismic spectra in this region, but just an effective value, to be used together with the southern California spectral model. Indepentent information on the source parameters in the region under investigation will allow us to reevaluate our estimate of κ_0. Conversely, if we had an independent estimate of κ_0, we would be able to define a better set of parameters for the source spectrum.

Colfiorito
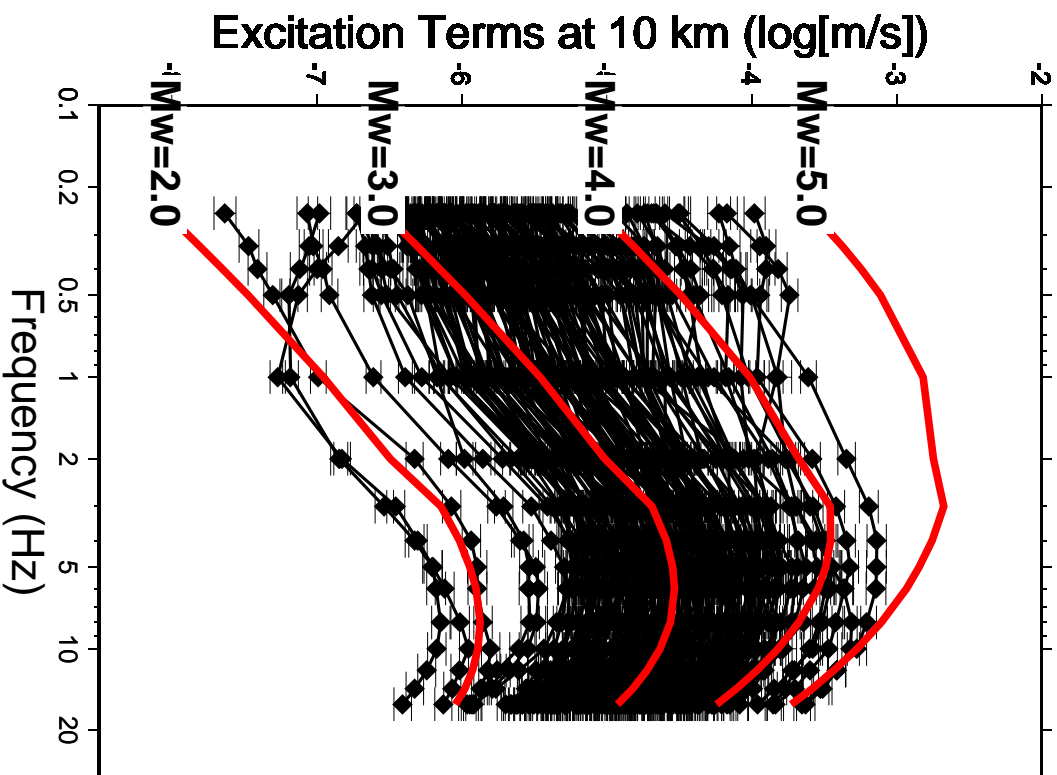
Figure 4.6: Inverted excitation terms relative to the events recorded by the portable network deployed by ING during the Colfiorito sequence in 1997 (black symbols connected by the black thin lines). Red (gray) thick lines correspond to estimates of the peak filtered velocities calculated at the sampling frequencies by using the RVT. In order to perform this calculations, we used the southern California source spectral model used by Boore and Joyner (1997), a body-wave geometrical spreading, a frequency- and distance-dependent duration that reproduce the trends shown in Figure 4.4. We also used the following regional estimates of the attenuation parameters: $Q(f) = 130 \cdot f^{0.10}$ and $\kappa_0 = 0.00$.

4.3.6   Site Terms

Figure 4.7 show the site term obtained from the regression on the peak amplitudes. Given the constraint

$$\sum_i SITE_i(f) = 0$$

the individual site terms shown in the figure represent the deviation of the specific site from the network average. Figure 4.7 shows that there are not large fluctuation from the network average at the various frequencies, although for frequencies higher than 2.0 Hz the distribution of the site terms gets wider.

No detailed information about the site geology is available at each seismometric location, although we know that all of them were deployed on rock outcrops. For this reason we expect the constraint forced on site terms to result in a relatively small bias on the inverted source terms. Finally, in Figure 4.8, we show the residuals of the general regression at a set of six central frequencies.

4.3.7   Comparison with the coda normalization results

Figure 4.9 compares the attenuation functional obtained from the final regression to its estimate computed by using the coda normalization technique. The figure again indicates that the coda normalization technique represents a good tool for the empirical determination of the attenuation functional in a region.

Colfiorito
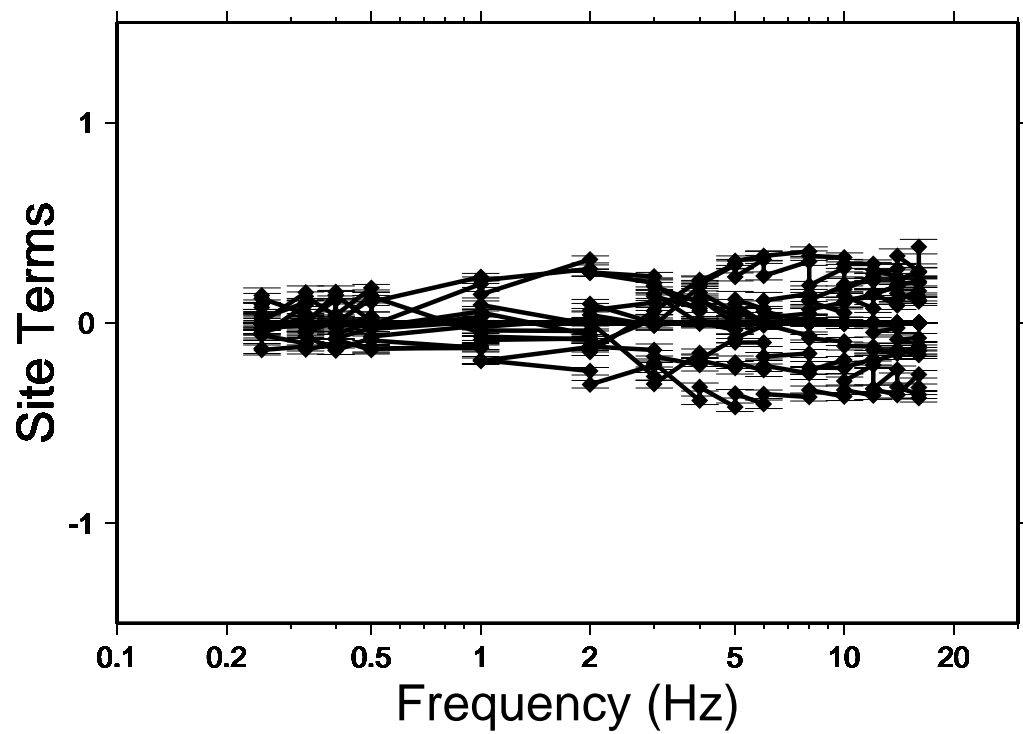
Figure 4.7: Inverted site terms for the Colfiorito data set.
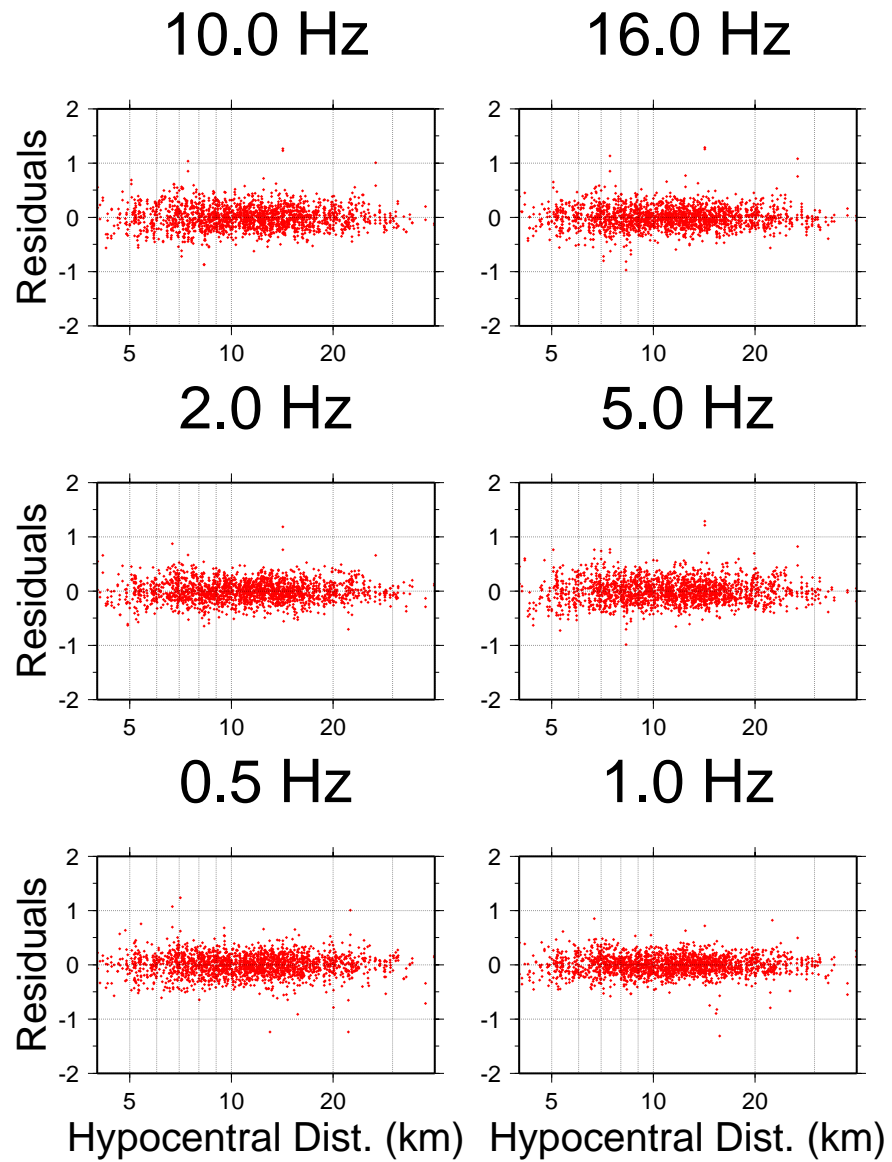
Figure 4.8: Final residuals computed at 0.5, 1.0, 2.0, 5.0, 10.0 and 16.0 Hz.
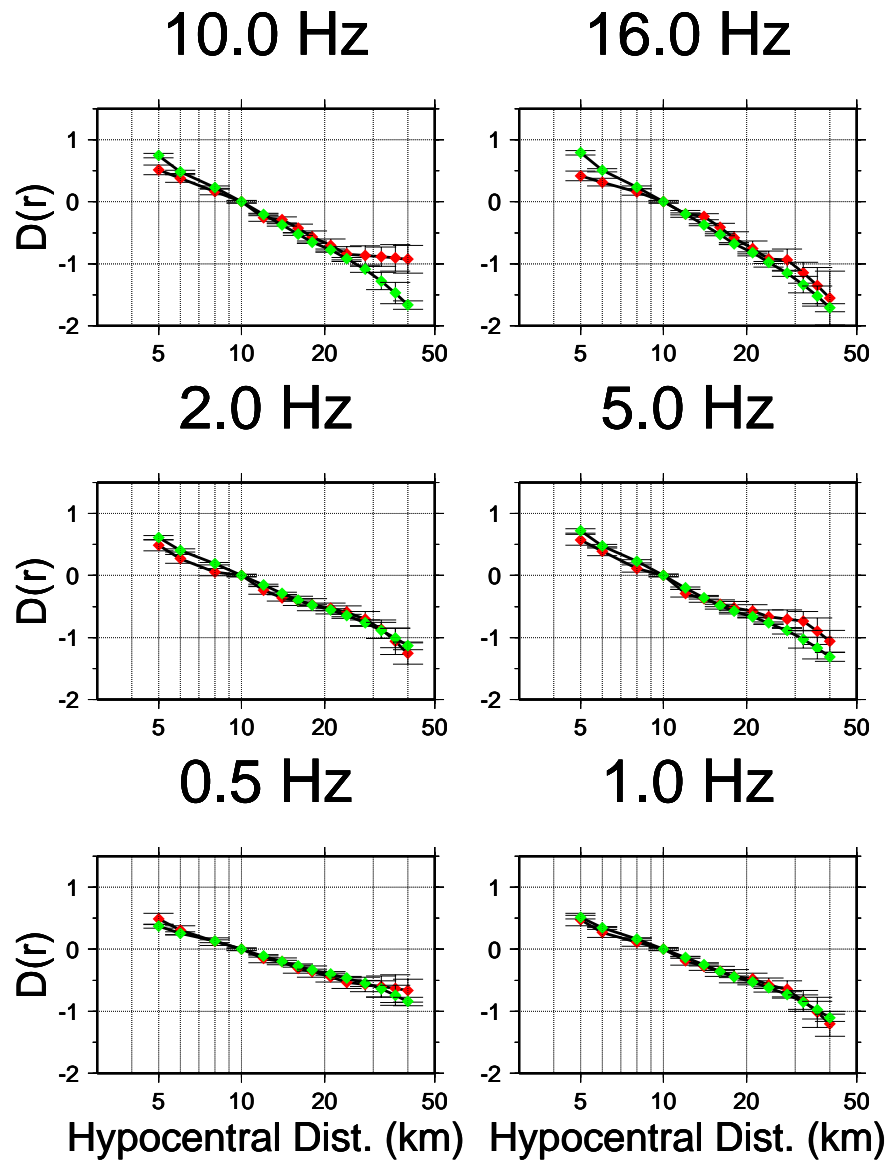
Figure 4.9: Comparison between the attenuation functional obtained from the general regression (red -dark gray- diamonds), and its estimate at various frequencies computed by using the coda normalization technique (green -light gray- diamonds). The six frames in this picture show the comparison at the frequencies of: 0.5, 1.0, 2.0, 5.0, 10.0 and 16.0 Hz.

4.4 Conclusions

We computed the ground motion attenuation relationships for narrow bandpass filtered time histories, within the region damaged by the Umbria-Marche seismic sequence of September-November 1997. The results shown here are valid for short hypocentral distances ($r \leq 40$ km).

A regression was performed over a large data set of over 2,000 horizontal seismograms recorded by a portable seismic network deployed by the Istituto Nazionale di Geofisica, in order to obtain the attenuation relationships of the peak values of bandpass filtered time histories. The results obtained in this chapter confirm the predictive model proposed for the Apennines region in Chapter 2, at least for what concerns the attenuation parameter

$$Q(f) = 130 \cdot f^{0.10}.$$

A simple direct-wave geometrical spreading was used to model the attenuation functional at all distances, up to 40 km. The spreading is described by

$$g(r) = r^{-1}.$$

The given estimate of the high-frequency attenuation parameter $\kappa_0 = 0.00$ is biased by the use of a source model calibrated in the southern California region (Boore and Joyner, 1997). This estimate of the high-frequency parameter, κ_0, is meaningful for the Umbria-Marche region only if coupled with the southern California source model. The one presented here is an estimate of effective κ_0.

5. Ground Motion Scaling in Germany

We have also investigated scaling laws at regional distances within Germany. This chapter describes the German crustal environment, the characteristics of the German Regional Seismic Network (GRSN), from which the data were obtained, the data set processed, and presents the results obtained for the region. In this case, we were able to obtain good results for both the peak values of the filtered ground velocities and the Fourier amplitude spectra.

5.1   Characteristics of the German Crust

Germany has been affected by three episodes of orogenic activity (Zeis et al., 1990). The Variscan orogeny is responsible for the NE-SW strike direction of the structures in the area, the Alpine orogeny caused a general uplift and block faulting of the whole Variscan area, whereas the last episode was the continental rifting and the formation of the Rhine graben.

The Black Forest is located at the eastern Flank of the Rhine graben rift zone and consists essentially of gneisses and granites of Variscan age to the east. To the north, Paleozoic rocks disappear underneath sedimentary rocks of Permian and Triassic age. In the Bohemian Massif, to the east, plutonic rocks of the Variscan basement are also exposed.

The northwestern German Basin (Wever et al., 1990) is generally characterized by a poorly reflective upper crust, generally, but also by dipping reflectors in both the upper and the lower crust. The depth of the Moho

in this part of Germany is approximately 30 km. The Moho depth map by Meissner et al. (1987) indicates a rather constant crustal thickness along the central Part of Germany.

Most of southern Germany is covered by Mesozoic sediments. South of the Danube river is the Molasse basin, formed by Tertiary and Quaternary sediments that orginated during the Alpine orogeny. The Molasse units are 5 to 6 km thick near the northern margin of the Alps (Zeis et al., 1990).

From the Deep Continental Drilling Program (KTB, see Gajewski and Prodehl, 1987) carried out in the Black Forest, southwest Germany, and from seismic refraction data (Lüschen et al., 1987), we get information about the Conrad discontinuity, that has depths between 16 and 18 km. This boundary coincides with a low velocity zone of the middle crust (Gajewski and Prodehl, 1987), the existence of which was postulated earlier (Mueller et al., 1969; 1973). Towards the northwest and south, the Conrad descends to 20 and 22 km, respectively. The Moho reaches depths between 27 and 28 km in the central part of the triangle (Zeis et al., 1990).

Evidence from reflection data (Deichmann and Ansorge, 1983) implies that the lower crust beneath the Black Forest is laminated, producing a zone of high reflectivity. Beneath the Black Forest and Swabian Jura, the crustal thickness is reduced to 25 km. To the northwest, the Moho reaches depths as great as 35 km. Beneath the northern foreland of the Alps, near their northern margin, the Moho descends gradually to about 40 km in depth. The top of the lower crust in the central Black Forest (30 km to the east of the Rhine graben) is thought to be at about 14 km (Edel et al., 1975 and Zucca, 1984) Edel et al. (1975) and Zucca (1984) both located the Moho at 25 km beneath the Rhine graben. The top of the lower crust beneath the

graben is at about 10 km.

5.1.1   Anelasticity of the Crust

As far as the attenuation of the seismic waves is concerned, numerous studies are available in the region. Among others, Plenefisch et al. (1994) indicated $Q_s = 400$ for the crust and upper mantle in the area of the upper Rhine Graben and northern Switzerland, from a study on S_n and P_n waves.

5.2   Description of the German Regional Seismic Network (GRSN)

The history of the German Regional Seismic Network is tightly linked to the establishment of the Gräfenberg array (GRF) in the Frankonian Jura in southern Germany. The GRF array was established in 1976 by funding from the German Research Council and became fully operational in spring 1980 to fulfill Germany's commitment for global earthquake monitoring, for international exchange of seismic data, and for scientific research in the newly developing area of broad-band seismology (Harjes and Seidl, 1978). The GRF array was operated and maintained by the Seismological Central Observatory (SZGRF) in Erlangen, which is a subdivision of the Federal Institute for Geosciences and Natural Resources (BGR) located in Hannover. This latter organization planned the GRSN network as an extension to the GRF array. While the GRF array has an aperture of about 100 x 50 km, spanned by 13 seismometric elements arranged in 3 sub-arrays, the GRSN extends over the entire area of Germany, with the northernmost stations near the Baltic Sea, and the southernmost stations in the Black For-

est and the Alpine foreland, thus providing an aperture of about 600 x 400 km. Originally, when the GRSN was planned in the late 1980's, only eight seismograph stations were scheduled to be installed in Western Germany. This initial network became operational in summer of 1991 (Hanka, 1991). After Germany's reunification, another four stations were installed in the former East Germany and started operation in 1992 and 1993, with more stations added more recently.

Currently, the GRSN consists of 16 seismometric stations equipped with Streckeisen STS-2 three-component broadband seismometers with a flat velocity response from 40 Hz to 120 s (except for GRFO with KS36000 broadband sensor). The digital data acquisition system consists of a 24-bit digitizer (Quanterra Q680), sampling the data at a rate of 80 Hz. The sensitivity of the GRSN systems (one count) corresponds to 1.667 nm/s. The raw data stream is continuously stored on internal hard disks. An event detector marks the time windows of probable seismic events. The data are resampled at 20 Hz and 1 Hz. The initial 80 Hz, as well as resampling streams, are stored on magnetic tape (DAT or Exabyte) for archiving at SZGRF, where the continuous 20 Hz and 1 Hz data streams are copied to CD-Recordables (CD-R). In addition, the 80 Hz waveform data from local and regional events are also saved to these archive disks which can be accessed through a jukebox system. The 80 Hz data streams are the ones used in this study.

The stations of the GRSN network are supplemented by the broadband element GEC2 of the GERESS array located in the Bavarian Forest (Harjes, 1990) which is identically equipped as the GRSN stations, except for the fact that the data are digitized by a RDAS-200 system. The sensitivity of

the STS-2 seismometer at GEC2 seismometers is therefore different, with 19.89 counts/(nm/s). The broadband data of the GEC2 station are digitized at a sampling rate of 80Hz, and stored continuously on CD-R, located in the GRSN jukebox system at BGR. This CD-R archive of digital waveform data is easily accessed for assembling a large data set of event-based data.

Site conditions range from hardrock sites (i.e. BFO, GEC2, WET) for stations located in mountainous areas, particularly in southern Germany, to sites underlain by soft sediments (BUG) in the northern part of Germany, and for FUR in southern Germany as well, where the station is sited on the soft Molasse sediments. Table 5.1 provides some information about the stations of the GRSN that are used in this study.

5.3   Data Processing

Because of the favourable noise characteristics of the available stations, recordings from the GRSN allowed the analysis on both the peak values of the bandpass filtered time histories and the Fourier amplitude spectral components.

5.3.1   Bandpass Filters

We proceeded with the analysis at the following set of frequencies: 1.0, 2.0, 3.0, 4.0, 5.0, 6.0, 8.0, 10.0, 12.0, 14.0 and 16.0 Hz.

Again, each time history was narrow bandpass filtered around the sampling frequency f_0. This was done by applying a 8-pole, hi-pass Butterworth filter with a corner at $1/\sqrt{2}f_0$, followed by a 8-pole, lo-pass Butterworth filter with a corner at $\sqrt{2}f_0$. The peak value of each filtered time

German Regional Seismic Network - site information

Station	Lat. (N)	Long. (E)	Elevation (m above sea level)	Elevation (m above WGS-84)	Geology	Operation
BFO	48.3301	8.3296	589	639	Granite	Jan 1991
BRG	50.8732	13.9428	296	340	Devonian Hornblende slates	Feb 1993
BUG	51.4406	7.2693	85	131	Upper carboniferous clastic sedimentary rocks	Sep 1991
CLL	51.3077	13.0026	230	276	Ordovician greywacke rocks	Apr 1993
CLZ	51.8416	10.3724	680	719	Upper carboniferous clastic sedimentary rocks	Feb 1991
FUR	48.165	11.277	565	611	Moraine over molasse	Mar 1991
GSH	50.7370	6.3798	370	n/a	Devonian Slates	Jul 1995
MOX	50.6447	11.6156	455	501	Lower Carboniferous of the Thuringian Franconian Slate Mountains	Nov 1992
TNS	50.2225	8.4473	815	846	Taunus quartzite, Devonian	May 1991
WET	49.1440	12.8782	613	652	Gneiss	Jun 1991
GEC2[1]	48.84511	13.70156	1132	n/a	Granite	Jun 1991

Table 5.1: Information concerning the individual stations of the GRSN network, including geographic location and start of operation. [1]GEC2 is a supplemental broadband element of the GERESS array with STS-2 sensor, characterized by a 19.89 counts/(nm/s) sensitivity.
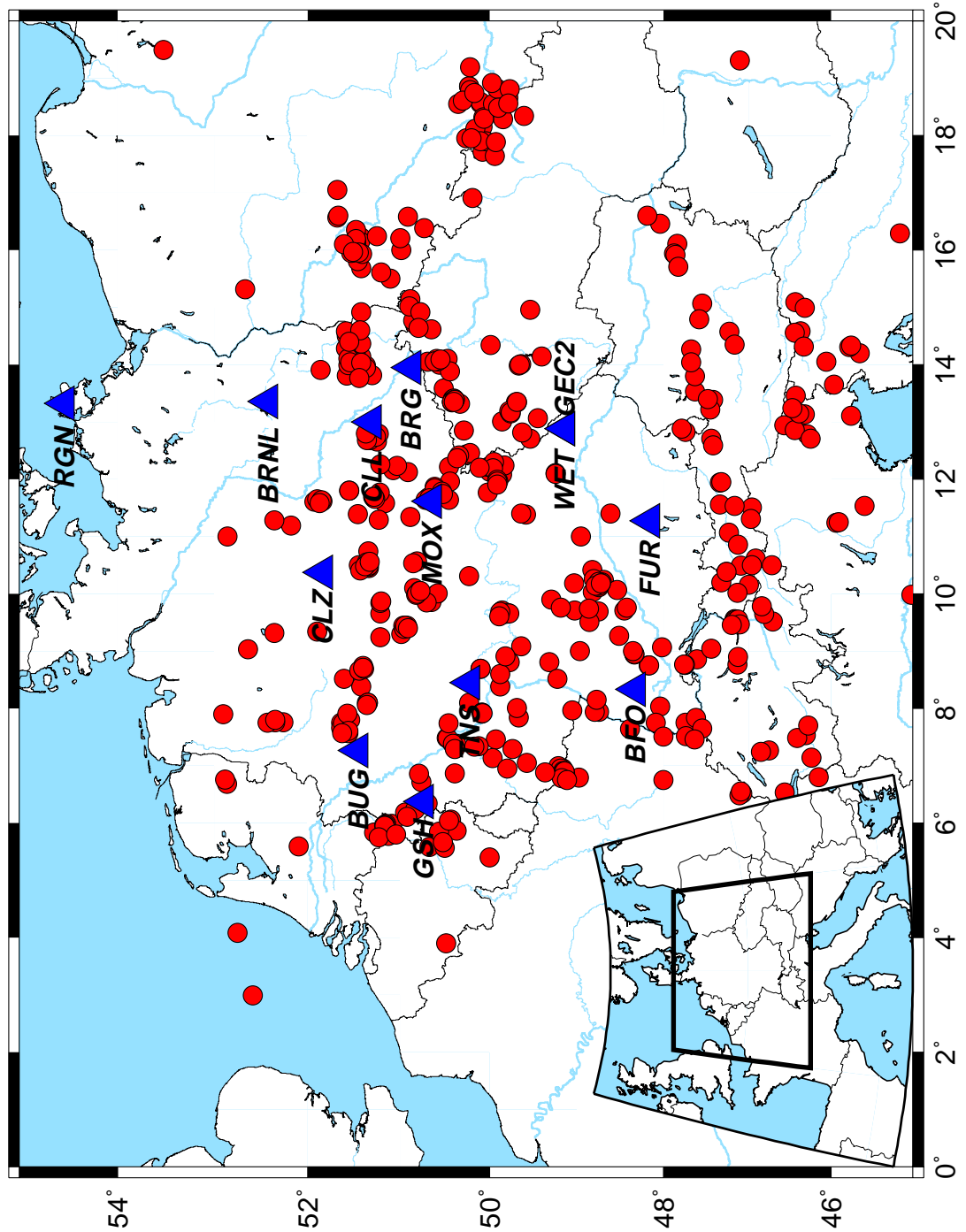
Figure 5.1: Map of central Europe. The stations of the German Regional Seismic Network (GRSN) are indicated by the blue (black) triangles; Red (gray) dots indicate the locations of the events (earthquakes and explosions) used in this study.

Grsn
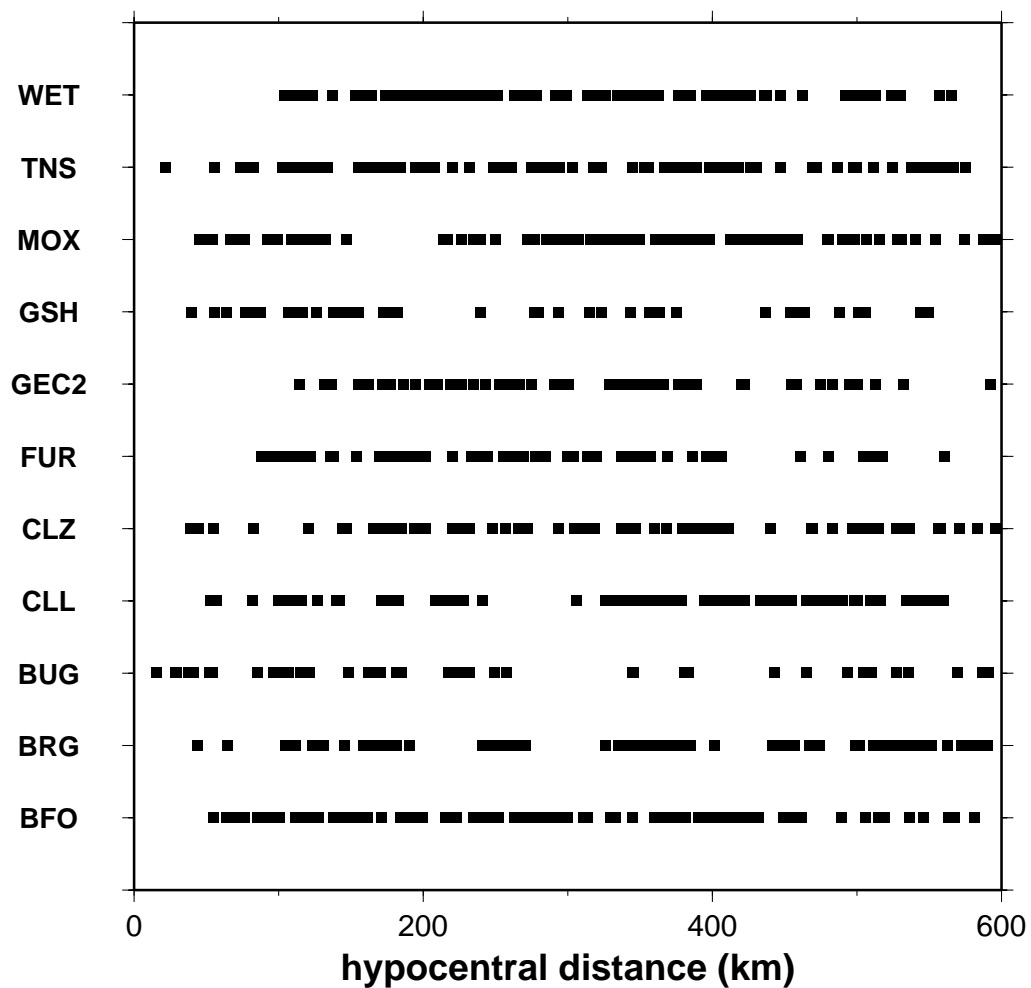
Figure 5.2: Source-receiver distances distribution for the GRSN stations used in this study. Each square in this picture represents one distinct three-component seismogram. The total number of three-component recordings used in this study is 1350. The even coverage at all distances shown by this figure allowed us to obtain results of high quality with a relatively small number of data points.

series, or the RMS average of the Fourier amplitude spectrum, is taken as the observed value at the hypocentral distance r.

5.3.2   Coda Normalization Analysis

As seen in the previous chapters, the first step in the processing procedure is carried out by computing the coda normalization estimate of the attenuation functional $D(r, f)$. Because of the presence of outliers in the data distribution shown in Figure 5.3, we preferred the use of a regression algorithm based on an L_1-norm minimization to quantify the attenuation functional obtained from the coda normalization method. Figure 5.3 shows the results relative to the regression on the filtered velocity peak values, whereas Figure 5.4 is relative to the coda normalization estimate of the $D(r, f)$ for the Fourier amplitude data set. The Figure refers to results obtained for frequencies of 0.5, 1.0, 2.0, 5.0, 10.0 and 16.0 Hz.

Since an inversion that minimizes the L_1-norm of the misfit vector does not allow the computation of uncertainties for the inverted model parameters, the error bars in the Figures 5.3 and 5.4 are computed from a least-squares inversion of the same data, for the same model parameters.

5.3.3   Duration of Ground Motion

Figure 5.5 presents the distribution of the calculated duration of the time windows containing the $5 - 75\%$ of the seismic energy following the S-wave arrival. The data points in Figure 5.5 are from all the available waveforms.

Again, the results are shown for the 0.5, 1.0, 2.0, 5.0, 10.0, 16.0 Hz central frequencies. It is clear from the picture that the duration of the ground

10.0 Hz

16.0 Hz

4.0 Hz

8.0 Hz

1.0 Hz

2.0 Hz

Hypocentral Dist. (km)   Hypocentral Dist. (km)
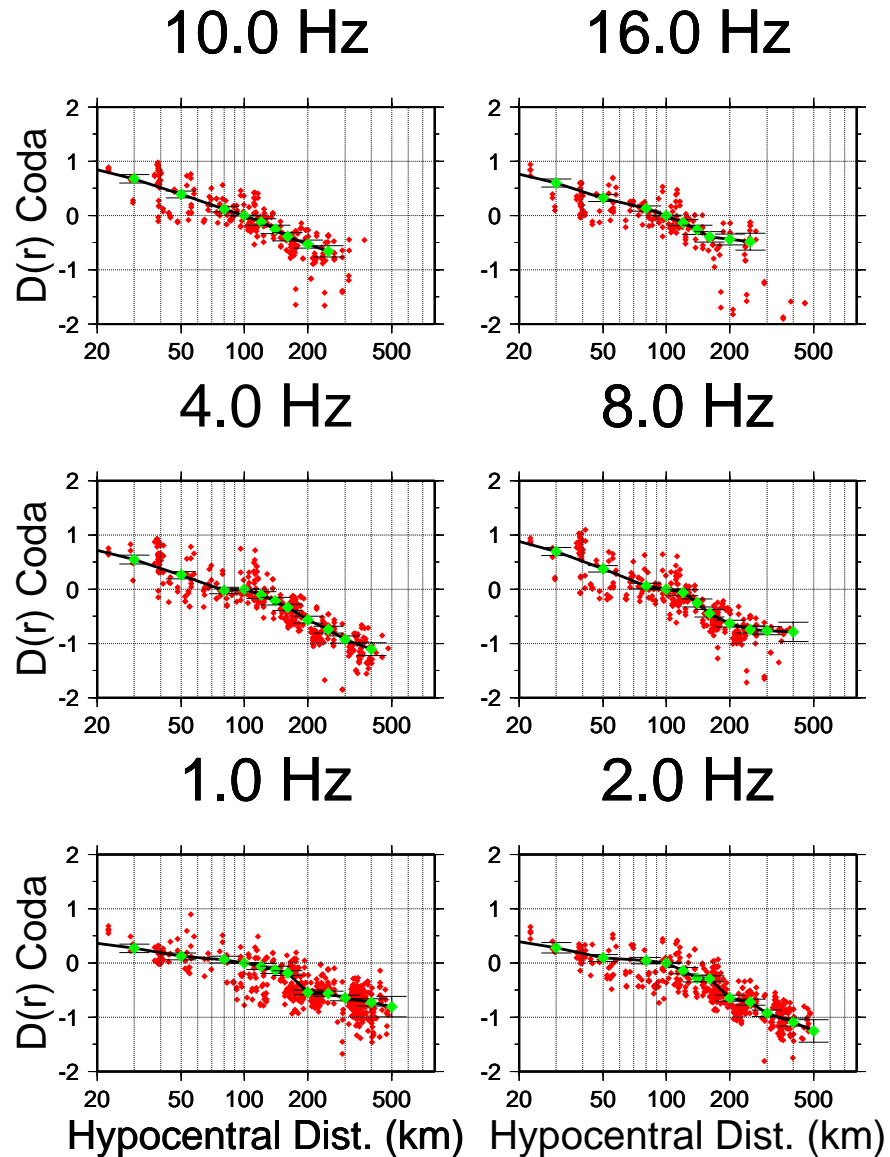
Figure 5.3: Results of the L_1 regressions over the reduced filtered velocity amplitudes (red -gray- small diamonds) at the frequencies indicated above each frame. Green (light gray) large diamonds represent the inverted values of the coda $D(r, f)$ at the nodal locations. Between each nodal point, the attenuation is computed by a linear interpolation. The distribution of the raw data is affected by large and numerous outliers; for such reason we chose to use an L_1 minimization algorithm. Note that the attenuation functional is normalized to zero at the reference distance of 100 km.

10.0 Hz   16.0 Hz

4.0 Hz   8.0 Hz

1.0 Hz   2.0 Hz

Hypocentral Dist. (km) Hypocentral Dist. (km)
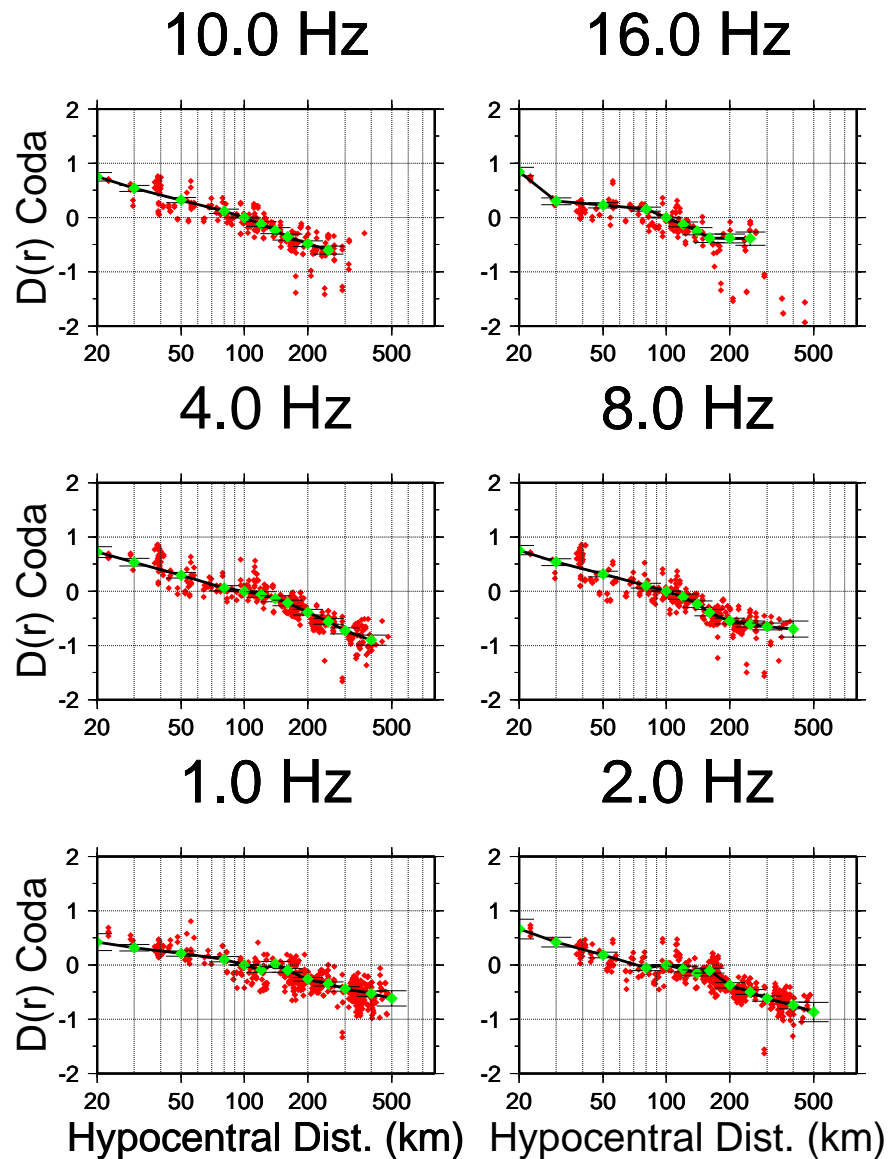
Figure 5.4: Results of the L_1 regressions over the reduced Fourier amplitudes (red -gray- small diamonds) at the frequencies indicated above each frame. Green (light gray) large diamonds represent the inverted values of the coda $D(r, f)$ at the nodal locations. Between each nodal point, the attenuation is computed by a linear interpolation. The distribution of the raw data is affected by large and numerous outliers; for such reason we chose to use an L_1 minimization algorithm. Note that the attenuation functional is normalized to zero at the reference distance of 100 km.

motion is characterized by a very small frequency dependence. It has not been possible to obtain an objective estimate of the duration functional as a function of frequency and distance for this data set. The following frequency-independent estimate of the duration as a function of distance, defined after visually inspecting the raw data, is used

$$T(r) = \begin{cases} 2.5 \ \text{s} & r = 50 \ \text{km} \\ 4.0 \ \text{s} & r = 100 \ \text{km} \\ 6.5 \ \text{s} & r = 170 \ \text{km} \\ 9.0 \ \text{s} & r = 200 \ \text{km} \\ 12.5 \ \text{s} & r = 400 \ \text{km} \\ 16.0 \ \text{s} & r = 700 \ \text{km} \end{cases}$$

5.3.4 Regional Attenuation

In this section we show the results of the final regressions on the peak filtered velocities and on the Fourier amplitudes (Figures 5.6 and 5.7), and the ones from the modeling as well. We modeled the attenuation functional by using the following parameters:

$$Q(f) = 400 \cdot f^{0.42}$$

$$g(r) = \begin{cases} r^{-0.8} & r \leq 140 \ \text{km} \\ r^{-1.5} & 140 \leq r \leq 180 \ \text{km} \\ r^0 & 180 \leq r \leq 220 \ \text{km} \\ r^{-0.5} & r \geq 220 \ \text{km} \end{cases}$$

Recall that

$$D(r, f) = \log\left(g(r) \exp\left[-\frac{\pi f}{VQ} r\right] \exp\left[\pi \kappa_0 f\right]\right).$$
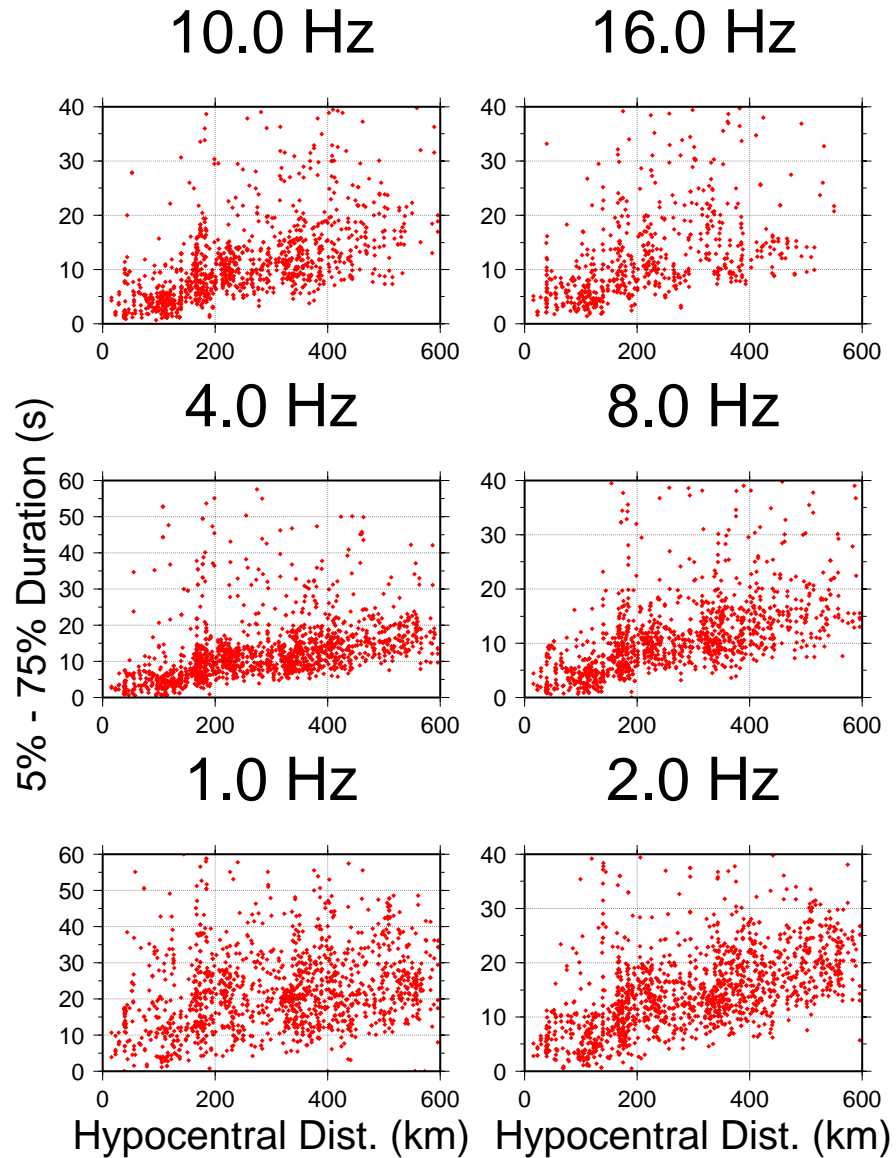
Figure 5.5: 5-75% duration distribution for the regional data at different frequencies. The x-axes refer to hypocentral distance (km), and the y-axes to duration (s). Duration is computed on each individual seismogram as the time window comprising the 5-75% of the seismic energy recorded by the specific station.
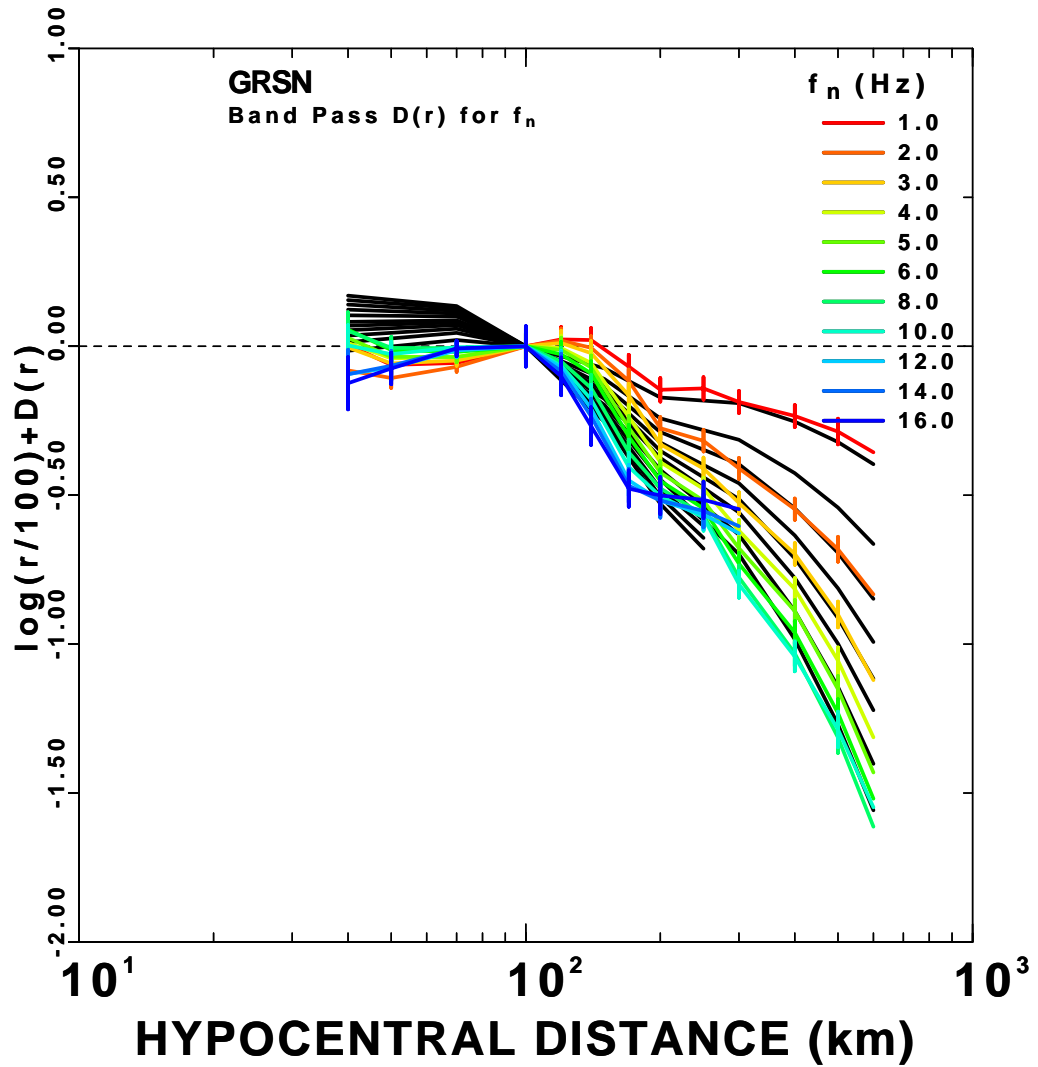
Figure 5.6: Attenuation functional $D(r, f)$ obtained from the regression on the peak values of the filtered velocities at the sampling frequencies of 1.0, 2.0, 3.0, 4.0, 5.0, 6.0, 8.0 10.0, 12.0, 14.0, 16.0 Hz (color, or tone of gray, lines). The attenuation functional has been normalized to zero at a reference hypocentral distance of 100 km. The black lines in the background describe our theoretical predictions of the attenuation relationships based on a simple model (see text for details).
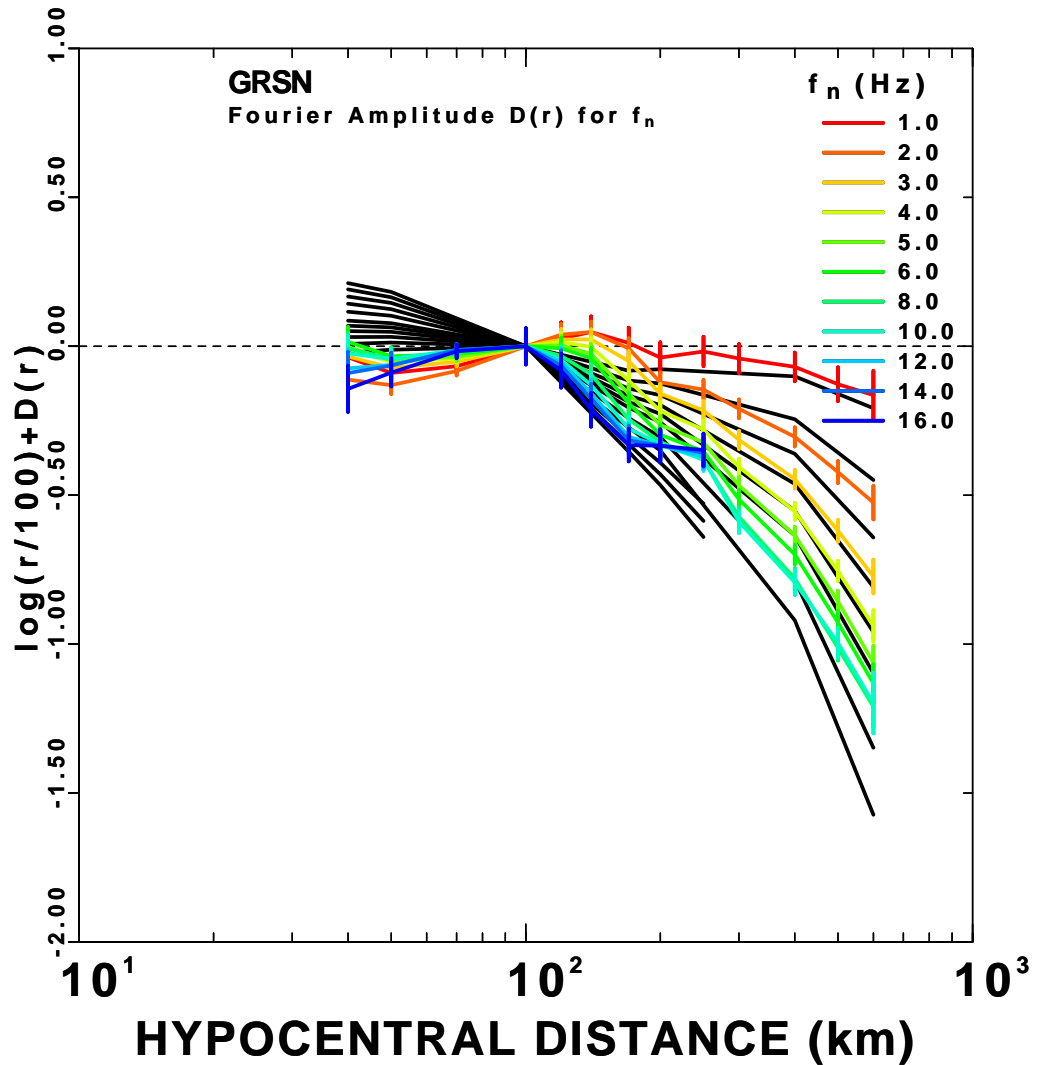
Figure 5.7: Attenuation functional $D(r, f)$ obtained from the regression on the peak values of the Fourier amplitudes at the sampling frequencies of 1.0, 2.0, 3.0, 4.0, 5.0, 6.0, 8.0, 10.0, 12.0, 14.0, 16.0 Hz (color, or tone of gray, lines). The attenuation functional has been normalized to zero at a reference hypocentral distance of 100 km. The black lines in the background describe our theoretical predictions of the attenuation relationships based on a simple model.

It is interesting to observe the behavior at large hypocentral distances ($r > 150$ km) of the high-frequency (12.0, 14.0 and 16.0 Hz) attenuation curves of Figures 5.6 and 5.7. The progressive reduction of the attenuation with increasing frequency cannot be explained by a simple attenuation model at all frequencies and distances. A similar phenomenon has been observed by Shin and Herrmann (1987) on recordings from the 1982 Miramichi earthquake.

The attenuation functionals for the peak filtered velocities and for the Fourier amplitudes are also described numerically by Tables 5.2, 5.3, 5.4, 5.5, 5.6, 5.7, 5.8 and 5.9 earthquake. These tables give the values of the functional $D(r, f)$ and of its associated uncertainties as a function of distance and frequency. Also the number of observations at each frequency-distance pair is indicated.

5.3.5 Site Terms

Figures 5.8 and 5.9 show the site terms obtained during the regressions on both the peak filtered velocities and the Fourier amplitudes. Some of the stations show divergence in the site term at high frequency ($f > 8$ Hz).

5.3.6 Excitation Terms

The excitation terms obtained from the regression are shown in Figures 5.10 and 5.11, respectively for the peak filtered velocities and for the Fourier amplitudes (black diamonds connected by thin black lines). Red (gray) thick lines in the figures represent the theoretical source term computed by using the southern California source model by Boore and Joyner (1997), coupled with the proposed geometrical spreading, attenuation pa-

Germany - Filtered Velocities
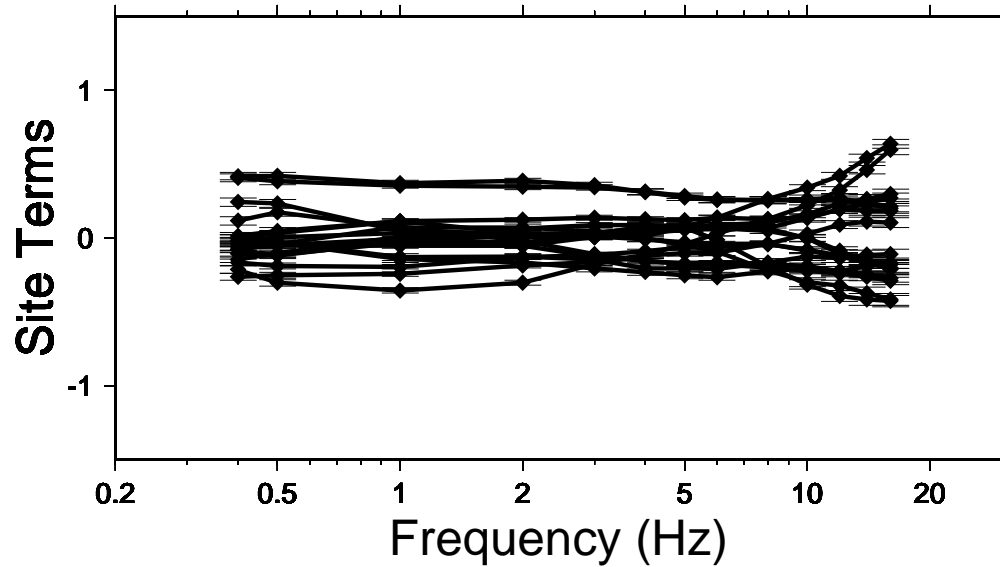
Figure 5.8: Inverted site terms (filtered velocity data).

Germany - Fourier Amplitudes
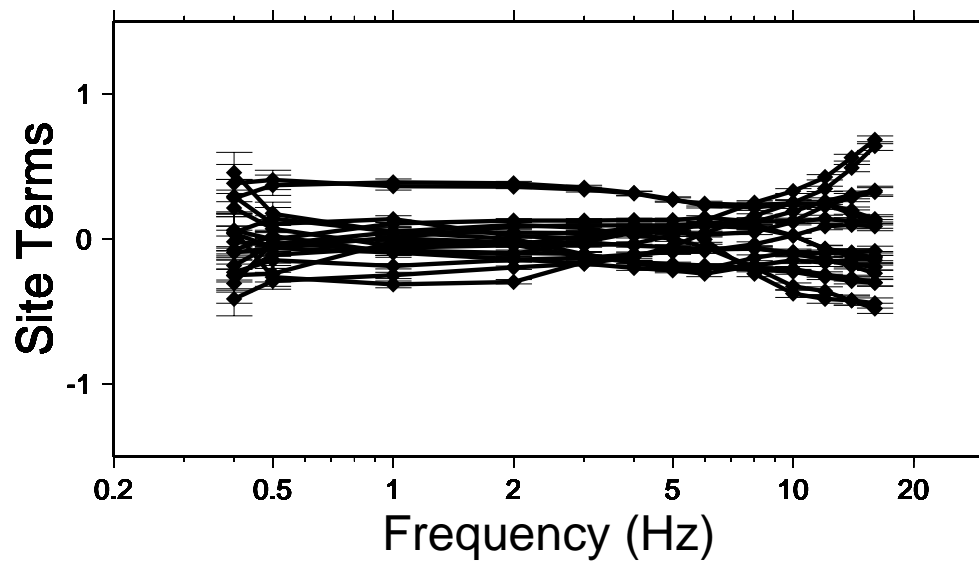
Figure 5.9: Inverted site terms (Fourier amplitude data).

rameters $Q(f)$ and κ_0, at the moment magnitudes indicated in the figures.

The high-frequency decay of the excitation terms were modeled by using

$$\kappa_0 = 0.08.$$

Two explanations can be used to justify the extremely high value of κ_0 just indicated: i) the parameter κ_0 trades off with the spectral model used to compute the spectra, and the southern California source spectral model is probably too rich in high frequencies for this region; ii) about 50% of our data set is made by explosion recordings. Since most of the explosions are related to strip mining blasts, we may expect these to mimic very low-stress drop sources, with spectra very much depleted in high frequencies when compared to the ones of actual earthquakes.

Figures 5.12 and 5.13 show the distribution of the residuals of the regressions carried out over the peak filtered and Fourier amplitudes, respectively. The residual distributions are shown at the frequencies of 0.5, 1.0, 2.0, 5.0, 10.0 and 16.0 Hz.

5.3.7   Comparison with the coda normalization results

Figures 5.14 and 5.15 compare the attenuation functionals obtained from the final regressions to their estimates computed by using the coda normalization technique. Again, the figures indicate that the coda normalization technique is a good tool for the empirical determination of the attenuation functional in a region, for both the Fourier spectral components and for the peak amplitudes.

Germany - Filtered Velocities
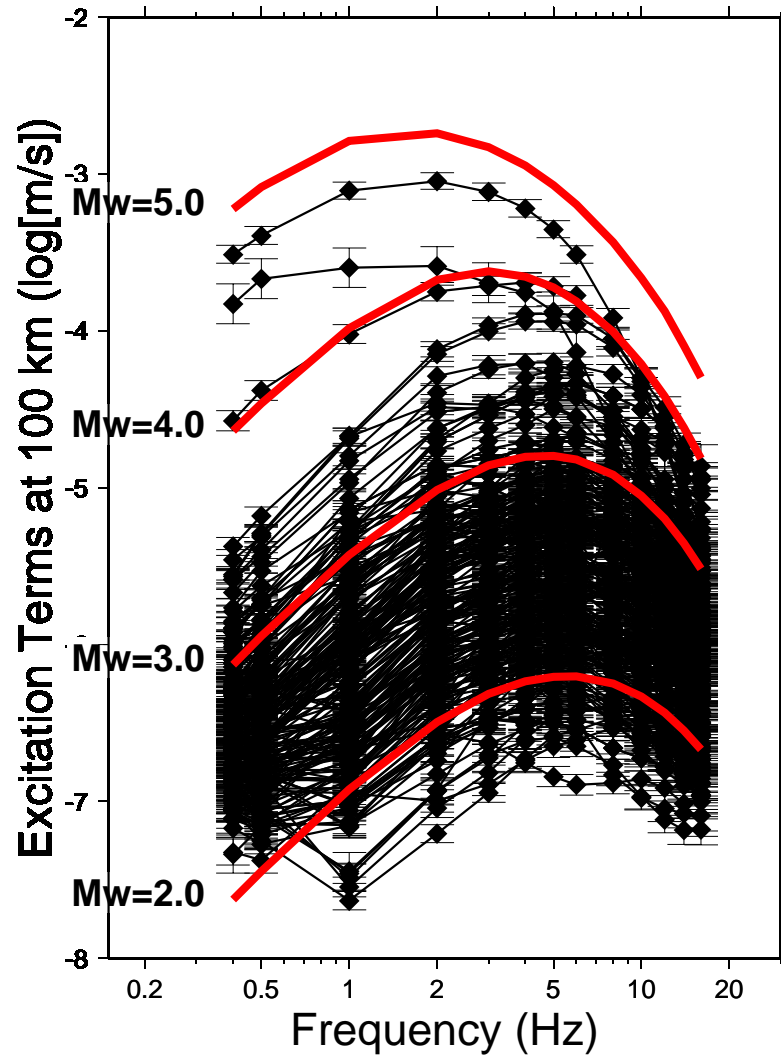
Figure 5.10: Inverted filtered velocity excitation terms (black diamonds linked by thin black lines). Thick red (gray) lines represent our estimates of the excitation terms, obtained at different magnitudes by using the Random Vibration Theory.
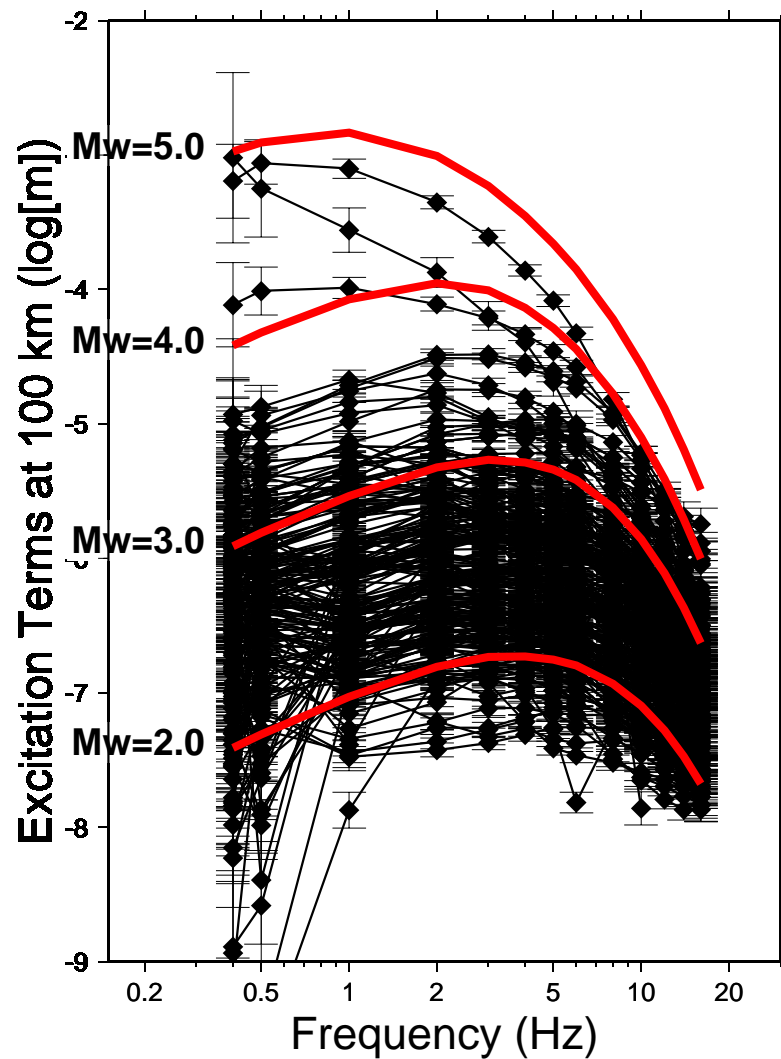
Figure 5.11: Inverted Fourier amplitudes excitation terms (black diamonds linked by thin black lines). Thick red (gray) lines represent our estimates of the excitation terms.

10.0 Hz

16.0 Hz

4.0 Hz

8.0 Hz

1.0 Hz

2.0 Hz
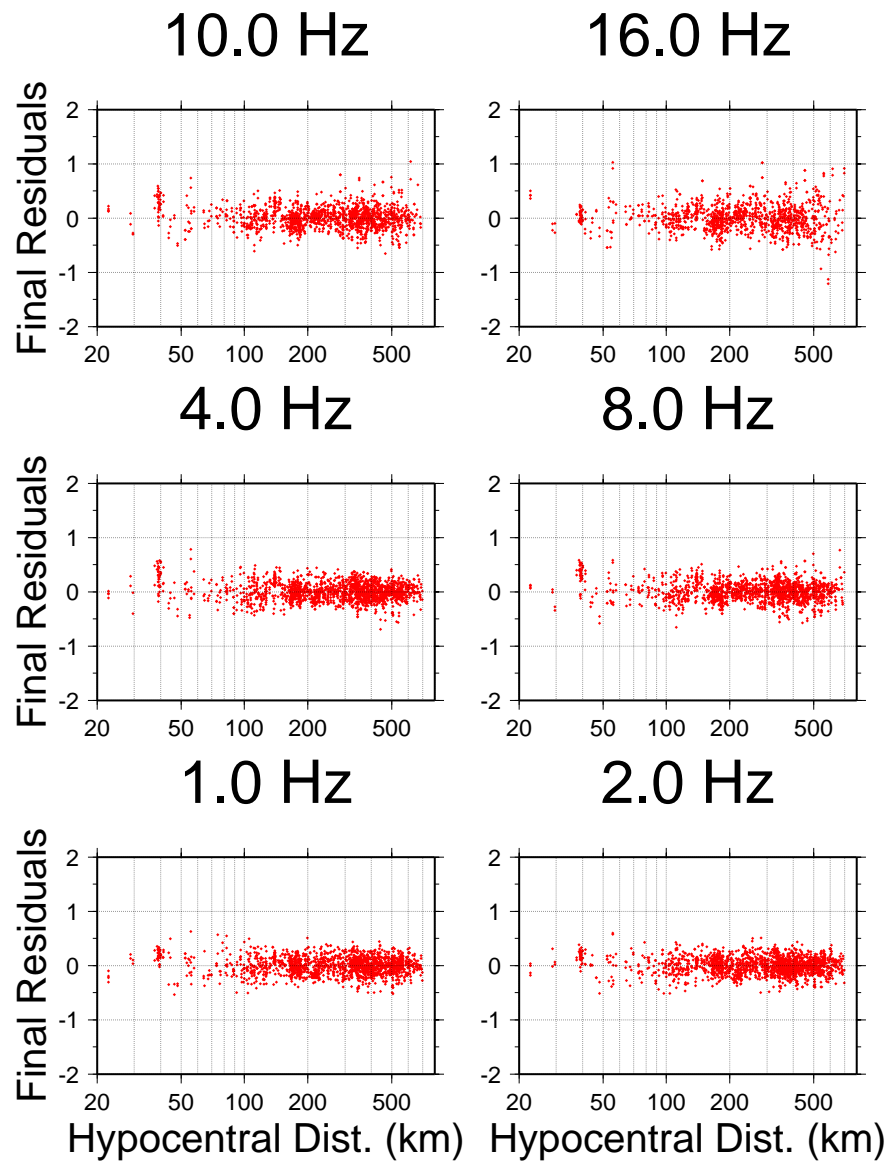
Figure 5.12: Final residuals computed at the sampling frequencies of 1.0, 2.0, 3.0, 4.0, 5.0, 6.0, 8.0 10.0, 12.0, 14.0, 16.0 Hz (filtered velocities).
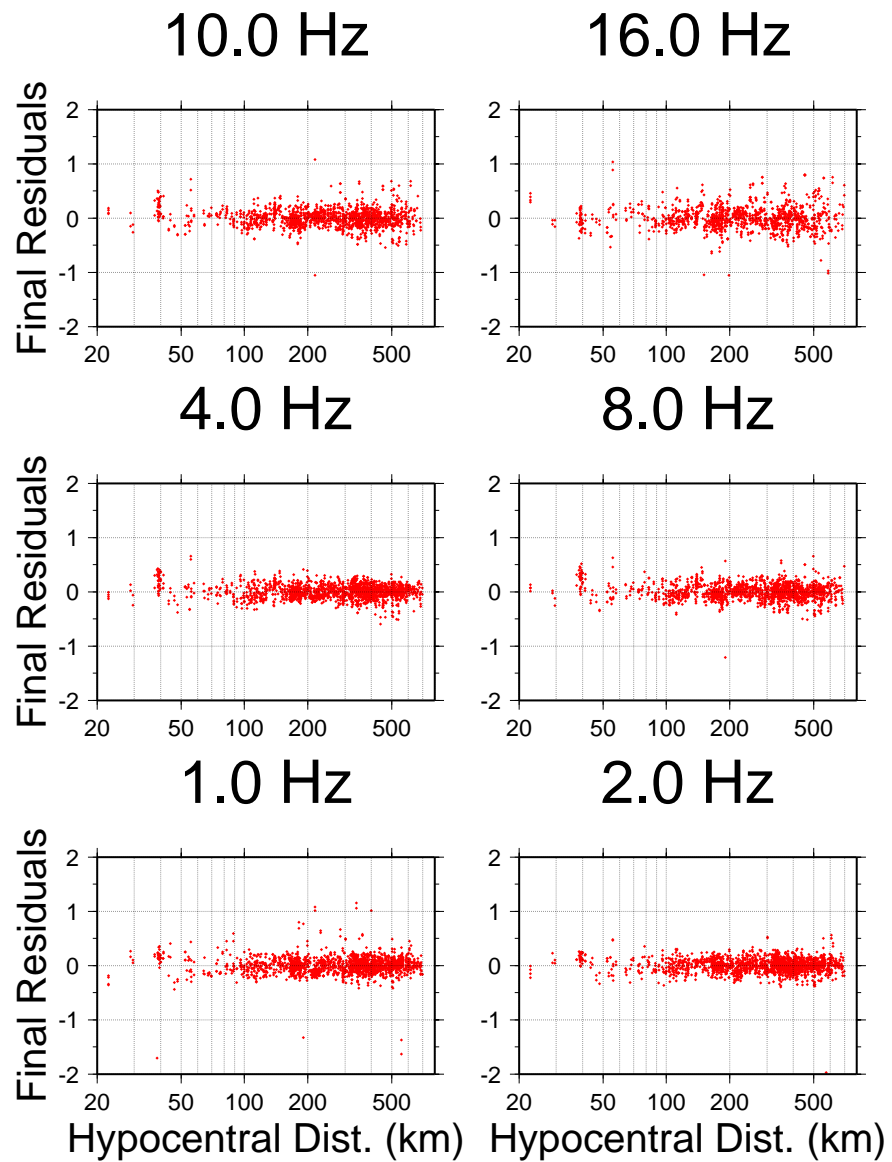
Figure 5.13: Final residuals computed at the sampling frequencies of 1.0, 2.0, 3.0, 4.0, 5.0, 6.0, 8.0 10.0, 12.0, 14.0, 16.0 Hz (Fourier amplitudes).
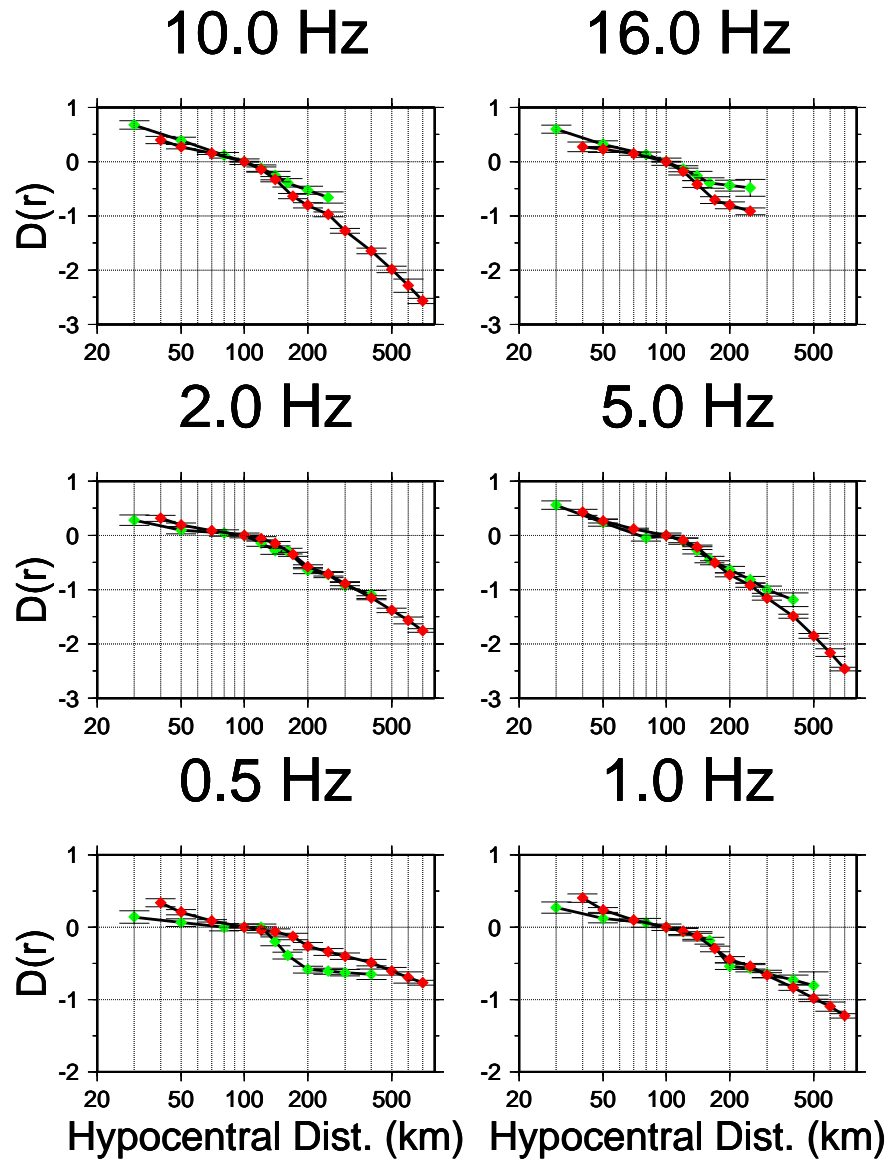
Figure 5.14: Comparison between the attenuation functional obtained from the general regression on the filtered peak amplitudes (red -dark gray- diamonds), and its estimate computed by using the coda normalization technique (green -light gray- diamonds). The six frames in this picture show the comparison at the frequencies of: 1.0, 2.0, 4.0, 8.0, 10.0 and 16.0 Hz.

10.0 Hz

16.0 Hz

2.0 Hz

5.0 Hz

0.5 Hz

1.0 Hz

Hypocentral Dist. (km) Hypocentral Dist. (km)
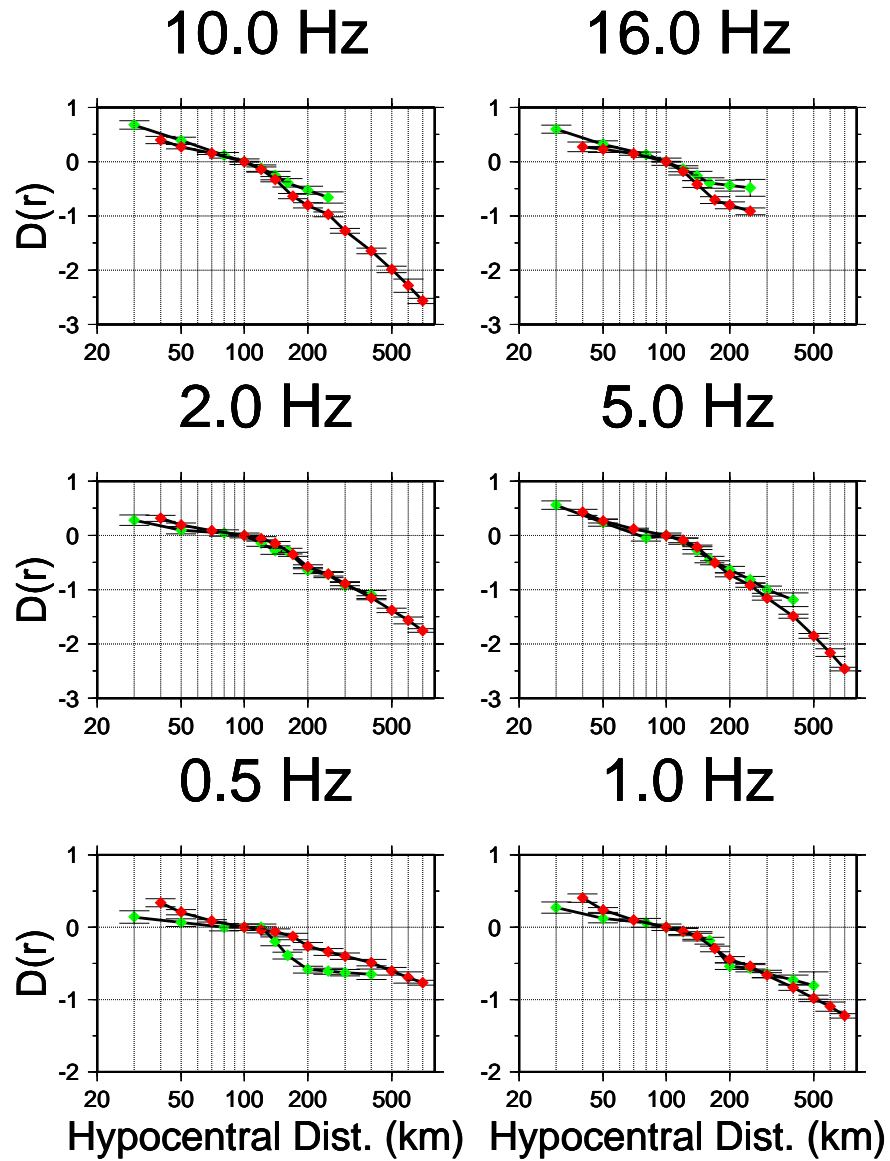
Figure 5.15: Comparison between the attenuation functional obtained from the general regression on the Fourier spectral components (red -dark gray-diamonds), and its estimate computed by using the coda normalization technique (green -light gray- diamonds). The six frames in this picture show the comparison at the frequencies of: 1.0, 2.0, 4.0, 8.0, 10.0 and 16.0 Hz.

Germany FILT Attenuation Functional									
f (Hz)	r (km)	$D(r, f)$	σ	Nobs	f (Hz)	r (km)	$D(r, f)$	σ	Nobs
	40.000	0.403	0.567E-01	6.970		40.000	0.317	0.562E-01	6.970
	50.000	0.239	0.342E-01	20.465		50.000	0.195	0.339E-01	20.465
	70.000	0.099	0.172E-01	34.269		70.000	0.086	0.170E-01	34.269
	100.000	0.000	0.444E-01	67.438		100.000	0.000	0.431E-01	67.438
	120.000	-0.056	0.419E-01	73.794		120.000	-0.060	0.405E-01	73.794
	140.000	-0.125	0.407E-01	88.262		140.000	-0.151	0.392E-01	88.262
1.0	170.000	-0.298	0.395E-01	204.623	2.0	170.000	-0.346	0.380E-01	204.623
	200.000	-0.447	0.396E-01	156.433		200.000	-0.576	0.377E-01	167.379
	250.000	-0.539	0.380E-01	135.247		250.000	-0.715	0.361E-01	155.606
	300.000	-0.664	0.375E-01	259.584		300.000	-0.887	0.356E-01	290.886
	400.000	-0.836	0.374E-01	365.784		400.000	-1.149	0.360E-01	389.657
	500.000	-0.985	0.434E-01	254.388		500.000	-1.380	0.420E-01	262.287
	600.000	-1.096	0.631E-01	131.002		600.000	-1.565	0.631E-01	133.174

Table 5.2: Attenuation functional at 1.0 and 2.0 Hz. The columns give values of frequency (first and sixth columns), hypocentral distance (second and seventh columns), attenuation (third and eighth columns), associated error bar (fourth and nineth columns), and number of observations (fifth and tenth columns).

Germany FILT Attenuation Functional									
f (Hz)	r (km)	$D(r,f)$	σ	Nobs	f (Hz)	r (km)	$D(r,f)$	σ	Nobs
	40.000	0.394	0.574E-01	6.970		40.000	0.409	0.580E-01	6.970
	50.000	0.244	0.346E-01	20.465		50.000	0.261	0.350E-01	20.465
	70.000	0.107	0.173E-01	34.269		70.000	0.119	0.176E-01	34.269
	100.000	0.000	0.439E-01	67.438		100.000	0.000	0.448E-01	67.438
	120.000	-0.068	0.413E-01	73.794		120.000	-0.085	0.418E-01	73.794
	140.000	-0.169	0.400E-01	88.262		140.000	-0.202	0.406E-01	88.262
3.0	170.000	-0.395	0.389E-01	204.623	4.0	170.000	-0.467	0.393E-01	204.623
	200.000	-0.630	0.384E-01	166.226		200.000	-0.690	0.391E-01	165.338
	250.000	-0.808	0.368E-01	157.532		250.000	-0.876	0.372E-01	153.153
	300.000	-1.003	0.362E-01	289.390		300.000	-1.096	0.364E-01	288.002
	400.000	-1.299	0.368E-01	386.072		400.000	-1.417	0.373E-01	386.185
	500.000	-1.599	0.435E-01	257.644		500.000	-1.754	0.445E-01	249.410
	600.000	-1.842	0.659E-01	126.510		600.000	-2.035	0.687E-01	115.245
	40.000	0.426	0.573E-01	6.970		40.000	0.454	0.579E-01	6.970
	50.000	0.266	0.345E-01	20.465		50.000	0.289	0.349E-01	21.253
	70.000	0.119	0.174E-01	34.269		70.000	0.136	0.175E-01	34.481
	100.000	0.000	0.436E-01	67.438		100.000	0.000	0.443E-01	67.438
	120.000	-0.091	0.411E-01	73.794		120.000	-0.106	0.417E-01	73.794
	140.000	-0.217	0.399E-01	88.262		140.000	-0.237	0.406E-01	88.262
5.0	170.000	-0.503	0.386E-01	204.623	6.0	170.000	-0.533	0.393E-01	204.623
	200.000	-0.725	0.385E-01	166.942		200.000	-0.753	0.392E-01	165.226
	250.000	-0.916	0.367E-01	151.823		250.000	-0.942	0.373E-01	150.438
	300.000	-1.155	0.360E-01	281.006		300.000	-1.207	0.368E-01	275.824
	400.000	-1.491	0.373E-01	379.016		400.000	-1.563	0.389E-01	366.695
	500.000	-1.850	0.448E-01	230.097		500.000	-1.930	0.464E-01	213.770
	600.000	-2.161	0.714E-01	105.744		600.000	-2.248	0.768E-01	96.903

Table 5.3: Attenuation functional at 3.0, 4.0, 5.0 and 6.0 Hz. The columns give values of frequency (first and sixth columns), hypocentral distance (second and seventh columns), attenuation (third and eighth columns), associated error bar (fourth and nineth columns), and number of observations (fifth and tenth columns).

Germany FILT Attenuation Functional									
f (Hz)	r (km)	$D(r,f)$	σ	Nobs	f (Hz)	r (km)	$D(r,f)$	σ	Nobs
8.0	40.000	0.450	0.620E-01	6.970	10.0	40.000	0.401	0.687E-01	6.970
	50.000	0.296	0.374E-01	21.253		50.000	0.275	0.414E-01	21.253
	70.000	0.149	0.187E-01	34.481		70.000	0.152	0.207E-01	34.481
	100.000	0.000	0.478E-01	67.438		100.000	0.000	0.531E-01	67.438
	120.000	-0.130	0.449E-01	73.794		120.000	-0.144	0.497E-01	73.794
	140.000	-0.286	0.439E-01	88.262		140.000	-0.324	0.490E-01	88.262
	170.000	-0.586	0.423E-01	204.623		170.000	-0.635	0.472E-01	204.623
	200.000	-0.778	0.425E-01	163.346		200.000	-0.804	0.476E-01	160.884
	250.000	-0.964	0.404E-01	147.515		250.000	-0.972	0.452E-01	141.173
	300.000	-1.253	0.402E-01	265.677		300.000	-1.276	0.454E-01	246.186
	400.000	-1.633	0.434E-01	334.261		400.000	-1.644	0.493E-01	297.295
	500.000	-2.012	0.520E-01	187.006		500.000	-1.985	0.600E-01	153.749
	600.000	-2.308	0.865E-01	85.801		600.000	-2.283	0.121E+00	66.539
12.0	40.000	0.305	0.755E-01	6.970	14.0	40.000	0.304	0.827E-01	6.970
	50.000	0.230	0.454E-01	21.253		50.000	0.236	0.498E-01	21.253
	70.000	0.141	0.228E-01	34.481		70.000	0.147	0.249E-01	34.481
	100.000	0.000	0.576E-01	67.438		100.000	0.000	0.630E-01	67.438
	120.000	-0.151	0.544E-01	73.794		120.000	-0.163	0.593E-01	73.794
	140.000	-0.355	0.536E-01	88.262		140.000	-0.381	0.591E-01	88.262
	170.000	-0.680	0.520E-01	204.623		170.000	-0.698	0.568E-01	204.623
	200.000	-0.819	0.521E-01	152.791		200.000	-0.819	0.575E-01	147.976
	250.000	-0.962	0.499E-01	134.807		250.000	-0.950	0.555E-01	126.737

Table 5.4: Attenuation functional at 8.0, 10.0, 12.0 and 14.0 Hz. The columns give values of frequency (first and sixth columns), hypocentral distance (second and seventh columns), attenuation (third and eighth columns), associated error bar (fourth and nineth columns), and number of observations (fifth and tenth columns).

Germany FILT Attenuation Functional				
f (Hz)	r (km)	$D(r,f)$	σ	Nobs
16.0	40.000	0.274	0.880E-01	6.970
	50.000	0.227	0.530E-01	21.253
	70.000	0.148	0.264E-01	34.481
	100.000	0.000	0.682E-01	67.438
	120.000	-0.180	0.636E-01	73.794
	140.000	-0.414	0.636E-01	88.262
	170.000	-0.708	0.614E-01	204.623
	200.000	-0.802	0.623E-01	144.550
	250.000	-0.913	0.612E-01	122.972

Table 5.5: Attenuation functional 16 Hz. The columns give values of frequency (first column), hypocentral distance (second column), attenuation (third column), associated error bar (fourth column), and number of observations (fifth column).

Germany FFT Attenuation Functional									
f (Hz)	r (km)	$D(r, f)$	σ	Nobs	f (Hz)	r (km)	$D(r, f)$	σ	Nobs
	40.000	0.361	0.725E-01	6.970		40.000	0.286	0.500E-01	6.970
	50.000	0.212	0.440E-01	20.465		50.000	0.171	0.302E-01	20.465
	70.000	0.088	0.213E-01	34.269		70.000	0.072	0.150E-01	34.269
	100.000	0.000	0.583E-01	67.438		100.000	0.000	0.382E-01	67.438
	120.000	-0.053	0.546E-01	73.794		120.000	-0.040	0.360E-01	73.794
	140.000	-0.098	0.528E-01	88.262		140.000	-0.098	0.349E-01	88.262
1.0	170.000	-0.219	0.511E-01	204.623	2.0	170.000	-0.237	0.339E-01	204.623
	200.000	-0.339	0.516E-01	156.433		200.000	-0.422	0.335E-01	167.379
	250.000	-0.415	0.493E-01	135.247		250.000	-0.543	0.322E-01	155.606
	300.000	-0.518	0.488E-01	260.079		300.000	-0.687	0.318E-01	291.381
	400.000	-0.671	0.484E-01	366.288		400.000	-0.906	0.321E-01	390.162
	500.000	-0.826	0.570E-01	254.388		500.000	-1.121	0.374E-01	262.287
	600.000	-0.942	0.812E-01	131.002		600.000	-1.303	0.563E-01	133.174

Table 5.6: Attenuation functional at 1.0 and 2.0 Hz. The columns give values of frequency (first and sixth columns), hypocentral distance (second and seventh columns), attenuation (third and eighth columns), associated error bar (fourth and nineth columns), and number of observations (fifth and tenth columns).

Germany FFT Attenuation Functional									
f (Hz)	r (km)	$D(r,f)$	σ	Nobs	f (Hz)	r (km)	$D(r,f)$	σ	Nobs
	40.000	0.364	0.487E-01	6.970		40.000	0.389	0.449E-01	6.970
	50.000	0.229	0.295E-01	20.465		50.000	0.249	0.271E-01	20.465
	70.000	0.103	0.147E-01	34.269		70.000	0.114	0.135E-01	34.269
	100.000	0.000	0.373E-01	67.438		100.000	0.000	0.343E-01	67.438
	120.000	-0.056	0.352E-01	73.794		120.000	-0.065	0.323E-01	73.794
	140.000	-0.123	0.341E-01	88.262		140.000	-0.148	0.313E-01	88.262
3.0	170.000	-0.280	0.331E-01	204.623	4.0	170.000	-0.345	0.304E-01	204.623
	200.000	-0.460	0.326E-01	166.226		200.000	-0.518	0.302E-01	165.338
	250.000	-0.613	0.313E-01	157.532		250.000	-0.677	0.288E-01	153.153
	300.000	-0.791	0.308E-01	290.381		300.000	-0.882	0.282E-01	288.993
	400.000	-1.048	0.313E-01	387.081		400.000	-1.156	0.288E-01	387.194
	500.000	-1.318	0.366E-01	257.644		500.000	-1.453	0.344E-01	249.410
	600.000	-1.551	0.569E-01	126.510		600.000	-1.717	0.529E-01	115.245
	40.000	0.396	0.457E-01	6.970		40.000	0.413	0.490E-01	6.970
	50.000	0.254	0.277E-01	20.465		50.000	0.268	0.296E-01	21.253
	70.000	0.119	0.138E-01	34.269		70.000	0.129	0.147E-01	34.481
	100.000	0.000	0.349E-01	67.438		100.000	0.000	0.374E-01	67.438
	120.000	-0.076	0.329E-01	73.794		120.000	-0.086	0.354E-01	73.794
	140.000	-0.171	0.320E-01	88.262		140.000	-0.186	0.344E-01	88.262
5.0	170.000	-0.390	0.308E-01	204.623	6.0	170.000	-0.421	0.332E-01	204.623
	200.000	-0.565	0.308E-01	166.942		200.000	-0.598	0.331E-01	165.226
	250.000	-0.720	0.294E-01	151.823		250.000	-0.750	0.317E-01	150.438
	300.000	-0.944	0.288E-01	281.997		300.000	-0.991	0.312E-01	276.815
	400.000	-1.237	0.299E-01	380.025		400.000	-1.301	0.329E-01	367.704
	500.000	-1.555	0.358E-01	230.097		500.000	-1.626	0.391E-01	213.770
	600.000	-1.841	0.569E-01	105.744		600.000	-1.910	0.647E-01	96.903

Table 5.7: Attenuation functional at 3.0, 4.0, 5.0 and 6.0 Hz. The columns give values of frequency (first and sixth columns), hypocentral distance (second and seventh columns), attenuation (third and eighth columns), associated error bar (fourth and nineth columns), and number of observations (fifth and tenth columns).

Germany FFT Attenuation Functional									
f (Hz)	r (km)	$D(r,f)$	σ	Nobs	f (Hz)	r (km)	$D(r,f)$	σ	Nobs
8.0	40.000	0.390	0.511E-01	6.970	10.0	40.000	0.374	0.581E-01	6.970
	50.000	0.260	0.308E-01	21.253		50.000	0.259	0.351E-01	21.253
	70.000	0.135	0.153E-01	34.481		70.000	0.142	0.173E-01	34.481
	100.000	0.000	0.392E-01	67.438		100.000	0.000	0.450E-01	67.438
	120.000	-0.111	0.369E-01	73.794		120.000	-0.124	0.421E-01	73.794
	140.000	-0.240	0.361E-01	88.262		140.000	-0.276	0.415E-01	88.262
	170.000	-0.475	0.348E-01	204.623		170.000	-0.506	0.399E-01	204.623
	200.000	-0.622	0.349E-01	163.346		200.000	-0.630	0.403E-01	160.884
	250.000	-0.779	0.333E-01	147.515		250.000	-0.778	0.383E-01	141.173
	300.000	-1.049	0.331E-01	267.136		300.000	-1.066	0.386E-01	247.149
	400.000	-1.382	0.356E-01	335.801		400.000	-1.395	0.418E-01	298.331
	500.000	-1.711	0.427E-01	187.006		500.000	-1.694	0.507E-01	153.749
	600.000	-1.988	0.708E-01	85.801		600.000	-1.976	0.102E+00	66.539
12.0	40.000	0.324	0.640E-01	6.970	14.0	40.000	0.308	0.705E-01	6.970
	50.000	0.239	0.386E-01	21.253		50.000	0.237	0.426E-01	21.253
	70.000	0.140	0.191E-01	34.481		70.000	0.143	0.209E-01	34.481
	100.000	0.000	0.490E-01	67.438		100.000	0.000	0.544E-01	67.438
	120.000	-0.132	0.462E-01	73.794		120.000	-0.144	0.512E-01	73.794
	140.000	-0.303	0.456E-01	88.262		140.000	-0.323	0.510E-01	88.262
	170.000	-0.534	0.440E-01	204.623		170.000	-0.546	0.489E-01	204.623
	200.000	-0.635	0.441E-01	152.791		200.000	-0.634	0.495E-01	147.976
	250.000	-0.768	0.424E-01	134.807		250.000	-0.754	0.479E-01	126.737

Table 5.8: Attenuation functional at 8.0, 10.0, 12.0 and 14.0 Hz. The columns give values of frequency (first and sixth columns), hypocentral distance (second and seventh columns), attenuation (third and eighth columns), associated error bar (fourth and nineth columns), and number of observations (fifth and tenth columns).

Germany FFT Attenuation Functional				
f (Hz)	r (km)	$D(r,f)$	σ	Nobs
	40.000	0.255	0.772E-01	6.970
	50.000	0.213	0.467E-01	21.253
	70.000	0.138	0.228E-01	34.481
	100.000	0.000	0.611E-01	67.438
16.0	120.000	-0.161	0.569E-01	73.794
	140.000	-0.359	0.568E-01	88.262
	170.000	-0.562	0.548E-01	204.623
	200.000	-0.635	0.556E-01	144.550
	250.000	-0.746	0.548E-01	122.972

Table 5.9: Attenuation functional at 16 Hz. The columns give values of frequency (first column), hypocentral distance (second column), attenuation (third column), associated error bar (fourth column), and number of observations (fifth column).

5.4 Conclusions

We obtained the attenuation relationships for the region monitored by the German Regional Seismic Network (GRSN) by performing regressions over the peak amplitudes of narrowly bandpass filtered ground velocities and over the amplitudes of the ground velocity Fourier spectra.

These regressions allowed us to obtain a predictive model for the attenuation functional in the German region, written in terms of a product between a geometrical spreading and an anelastic attenuation function. The parameters of the attenuation functional for the German region are as follows:

$$Q(f) = 400 \cdot f^{0.42}$$

$$g(r) = \begin{cases} r^{-0.8} & r \leq 140 \text{ km} \\ r^{-1.5} & 140 \leq r \leq 180 \text{ km} \\ r^{0} & 180 \leq r \leq 220 \text{ km} \\ r^{-0.5} & r \geq 220 \text{ km} \end{cases}$$

$$\kappa_0 = 0.08$$

The extremely high value of the parameter κ_0 trades off with the spectral model used to predict the high-frequency content of the computed ground motion. The source model used here is suitable for southern California earthquakes (Boore and Joyner, 1997), and cannot match the low-energy frequency content that characterizes mining strip blasts. The latter represents about 50% of the events in our data set.

In order to use the RVT to build a predictive model for the peak filtered velocities, the following, frequency-independent duration function was used:

$$T(r) = \begin{cases} 2.5 \ \mathbf{s} & r = 50 \ \mathbf{km} \\ 4.0 \ \mathbf{s} & r = 100 \ \mathbf{km} \\ 6.5 \ \mathbf{s} & r = 170 \ \mathbf{km} \\ 9.0 \ \mathbf{s} & r = 200 \ \mathbf{km} \\ 12.5 \ \mathbf{s} & r = 400 \ \mathbf{km} \\ 16.0 \ \mathbf{s} & r = 700 \ \mathbf{km} \end{cases}$$

Independent studies must be carried out in this region of the world to investigate the source parameters, as well as the regional value of κ_0 for S-waves.

6. Conclusions

We produced the relationships describing the regional ground motion scaling in a seismically active region of the world (the Apennines, Italy, presented in Chapters 3 and 4), as well as in a more stable one (Germany, discussed in Chapter 5). In Italy, the need of a modern reevaluation of the seismic hazard is an urgent task to accomplish, whereas in Germany the calibration of the regional path response can have important implications in monitoring underground explosions.

The scaling relationships in the two regions were evaluated over broad frequency bands (0.25 - 16 Hz for the Italian region, 0.5 - 16 Hz for Germany). In Italy we did so by regressing data from the regional background seismicity, whereas the German data set comprised earthquakes, blasts and strip-mine explosions. On the German data, it was possible to perform regressions over the Fourier amplitudes at a set of different frequencies. For both regions, the same regressions were performed in the time domain, over the peak amplitudes obtained from time histories that have been bandpass filtered around the same set of sampling frequencies used for the analysis of the Fourier amplitudes.

The empirical attenuation relationships are modeled in terms of a simple mathematical model, which is completely defined in the frequency domain by three parameters (Q_0, η and κ_0), and by a complex geometrical

spreading function ($g(r)$):

$$D(r, f) = \log \left[g(r) \exp \left(\frac{-\pi f r}{V Q_0 f^\eta} \right) \exp \left(-\pi \kappa_0 f \right) \right]$$

$g(r)$ is given as a multi-linear function in a log log space. Multiple crossover distances are necessary in order to describe the transition between direct- and surface-waves geometrical spreadings. The attenuation of the peak values of the filtered time histories is also described by the same propagation term, but a duration function is also needed to take into account for the effects induced by the focusing of seismic radiation. The latter are due to the appearance of supercritical reflections, as well as by changes in the dispersion characteristics of the seismic signals at increasing hypocentral distances. Although the functional form used to model the crustal attenuation of seismic waves probably oversimplifies reality, in the cases shown in this study it effectively describes the empirical estimates of the ground motion scaling.

Random Vibration Theory (RVT) is used to obtain estimates of the peak ground motion in the time domain, given the Fourier amplitude spectrum and the duration of the seismic signal. Duration is defined as the time window that brackets the $5\% - 75\%$ of the seismic energy that follows the onset of the S-waves. Duration was computed for each available time history, and an L_1-norm minimization was used to empirically define duration as a function of frequency and distance for the entire Apennines. The L_1-norm is used because large outliers characterize the data distributions. The same procedure could not be applied to the German region.

6.1 Results

Our results indicate that the crust beneath the Apennines is characterized by a very high anelastic attenuation of the seismic energy within the studied frequency range. This results in relatively small areas of intense damage, even for the occurrence of earthquakes of moderate magnitude ($M \sim 7$).

If we compared the extension of the damaged areas for events of similar sizes in the two regions, or between Italy and other regions of the world where the crustal propagation is more efficient (e.g., central United States), we would see that the Apennines would suffer much smaller areas of severe ground shaking, although the vulnerability of the Italian historical cities to strong ground motion is extremely high. Seismic shear waves in the same frequency range in the German region attenuate less severely. The functional form needed to predict the observed attenuation in Germany is quite complex, involving a quadri-linear geometrical spreading (in a log log space).

Previous attenuation relationships were available for the Apennines (Sabetta and Pugliese, 1987, 1996), and the results of this study represent a significant improvement of them, in terms of the ability of accurately predicting the seismic spectra at increasing distances from the source. Sabetta and Pugliese obtained their attenuation relationships by regressing a small number of strong-motion accelerometric recordings taken from different geological and tectonic environments: eastern Alps, Apennines and Sicily. An important difference in our study is that, since we used mostly velocity recordings from the background seismicity, we were able to col-

lect a large set of recordings from the Apennines region. The total number of Italian horizontal component digital seismograms used in the analysis was over 6,000. During the process of collecting and analyzing data, we noticed that stable results were obtained only after adding the last 2,000 horizontal component recordings to the regional data set.

In their regressions, Sabetta and Pugliese did not include anelasticity, nor did they use a variable geometrical spreading with distance. We demonstrated that the high level of anelastic attenuation of the Apennines' crust plays a major role in reducing the ground motion amplitudes during earthquakes, and also that a variable geometrical spreading is needed in both regions in order to predict the details of the attenuation functional.

A much smaller number of horizontal component time histories (2700) was necessary in order to obtain high-quality empirical attenuation relationships for the German region. The availability of a permanent regional network allowed an efficient selection of the data set. The objective was to obtain an even distribution of the source-receiver distances, in the range of interest for our regional study. The fact that the German data were collected by a single regional network, whereas five different seismic networks were used to put together the Italian data set, is reflected in a more efficient achievement of the German results.

By using a source spectral model, our attenuation relationships and the RVT statistical tool, we were able to model the empirical attenuation functionals of both the investigated regions, within the entire distance and frequency ranges where data were available. It is important to keep in mind, however, that the use of a source spectral model that has not been calibrated in the regions of interest automatically introduces a bias in some

of the parameters of our theoretical attenuation functionals.

It is interesting to note that the duration of the ground motion along the Apennines is characterized by a significant dependence on frequency. On the other side of the Alps, the duration of the ground motion in the German region is almost frequency-independent.

The regional attenuation of the ground motion in the Apennines is well described by the following quantities:

- Geometrical spreading:

$$g(r) = \begin{cases} r^{-0.9} & r \leq 30\text{km} \\ r^0 & 30 \leq r \leq 80\text{km} \\ r^{-0.5} & r \geq 80\text{km} \end{cases}$$

- Anelastic attenuation:

  - $Q(f) = 130 \cdot f^{0.10}$

  - $\kappa_0 = 0.00$ **s**.

Although the spectral model of Rovelli et al. (1988), described in Chapter 3, was available for events in the Apennines, the large discrepancy found in the frequency dependence of the crustal $Q(f)$ between this and their studies prevented us from using it. Rovelli et al. (1988) used the following functional dependence for the quality factor:

$$Q(f) = 100 \cdot f.$$

We found that the linear increase of the parameter $Q(f)$ with frequency is excessive for this region. The consequence of this was probably a large bias on their high-frequency parameter, κ_0, toward a quite extreme value,

$$\kappa_0 = 0.07 \pm 0.02 \text{ s}.$$

Our estimate of κ_0 in the Apennines is obtained by using the southern California spectral model (Boore and Joyner, 1997) and our attenuation relationships. Our estimate is

$$\kappa_0 = 0.00 \text{ s}$$

which is very low, when compared to the ones independently obtained by analyzing broadband data of recent earthquakes that have occurred in different seismogenic areas along the Italian mountain belt ($\kappa_0 = 0.04 - 0.06$ s, Di Bona, personal communication). This indicates that the southern California model (single corner frequency, 70 bar stress drop, see Appendic C) is not a good approximation for the seismic sources in the Apennines. It seems that the spectral model is depleted in high frequencies, requiring the use of a null effective attenuation parameter κ_0 to match the observed excitation terms. Because of the choice of the parameters describing the source spectra in the Apennines and in Germany, our estimates of κ_0 in the two regions represent effective numbers, to be used together with the southern California spectral model. Independent studies are needed in order to provide estimates (or new estimates) of κ_0 and/or of the source spectral parameters.

The 70 bar stress drop seems to be too low for earthquakes occurred along the Apennines, and too high for the average event of the German data set. The value of stress-drop suggested by Rovelli et al. (1988) for events in the Apennines,

$$\Delta\sigma = 190 \pm 64 \text{ bar,}$$

probably represents a better choice for the Italian region.

The region covered by the German Regional Seismic Network (GRSN) shows a less severe anelastic attenuation than the Apennines. The attenuation functional for Germany is well described, both for the peak filtered velocities and the Fourier amplitudes, by the following quantities:

- Geometrical spreading:

$$
g(r) = \begin{cases}
r^{-0.8} & r \leq 140 \text{ km} \\
r^{-1.5} & 140 \leq r \leq 180 \text{ km} \\
r^{0} & 180 \leq r \leq 220 \text{ km} \\
r^{-0.5} & r \geq 220 \text{ km}
\end{cases}
$$

- Anelastic attenuation:

  - $Q(f) = 400 \cdot f^{0.42}$

  - $\kappa_0 = 0.08$ s.

The complex geometrical spreading function needed to reproduce the empirical attenuation functional in this region may reflect features of the vertical crustal structure, which in Germany is characterized by a well-developed Conrad discontinuity that sharply separates the upper from the lower crust, and by a laminated, highly reflective lower crust. None of the mentioned properties of the German crust, however, can be directly associated to a specific signature in the attenuation functional. The scarcity of large earthquakes in Germany shifts the interest on the regional attenuation functional on applications different from the seismic hazard assessment, even though a recent study by Newmann et al. (1999) on the New Madrid intra-cratonic seismic zone hypothesizes the erratic occurrence of large earthquakes even within otherwise stable continental shields.

The lack of information on the source spectral parameters in Germany, as well as on the high-frequency parameter κ_0, makes the obtained regional attenuation functional an effective estimate that combines both source and site uncertainties. The stress-drop parameter of the Boore and Joyner (1997) source model is probably too high for the average event in the German data set. This results in an extreme value for the effective high-frequency parameter $\kappa_0 = 0.08$ s.

6.2 Tradeoffs

We already pointed out that tradeoffs can affect the parameters of our empirical predictive model. In particular, the crustal attenuation function $Q(f) = Q_0 \cdot f^\eta$ (mostly the parameter Q_0), trades off with the geometrical spreading function $g(r)$ because of the limited distance range. Also, since in the Apennines we were not able to obtain information of good quality on the decay of the Fourier amplitude spectra as a function of distance, our estimate of the crustal attenuation parameter in that region was computed only over the peak values of the filtered time histories. In such a case, $Q(f)$ trades off also with the estimated duration function, although for the Apennines we were able to obtain an objective estimate of the duration as a function of frequency and hypocentral distance. The German data set, on the other hand, allowed the attenuation analysis to be carried out also on the Fourier amplitude spectra, and the modeling of the Fourier amplitudes only requires the use of a geometrical spreading function, and of the anelastic attenuation parameters.

Since the definition of a duration function is not necessary for the com-

putation of theoretical seismic spectra, the number of interacting parameters in the functional used to model the crustal propagation term in the frequency domain is reduced to three attenuation parameters (Q_0, η, κ_0), N crossover distances in the geometrical spreading function ($N = 1$ or 2 in most cases; $N = 2$ for the Apennines; $N = 3$ for Germany), and $N + 1$ exponents defining the steepnesses of the segments of the multi-linear (in a log log space) geometrical spreading.

We must be aware of the tradeoff between the source model and the parameters of our theoretical attenuation relationships. Specifically, the fact that the source model was not calibrated on the investigated regions introduced a bias on the high-frequency parameters κ_0 obtained in this study. The parameters Q_0 and η also trade off with the source spectral model, although the least significative bias is probably experienced by the frequency exponent in the quality factor formula, η, since the attenuation functionals show a strong sensitivity on this parameter alone.

6.3 Compared Crustal Attenuation Parameters, and their Physical Significance

After the discussion on the tradeoffs existing between the parameters of our attenuation models, it is clear that the crustal parameter $Q(f)$ obtained with our approach is of value only when compared to results of the same analysis obtained in other regions, but again the tradeoff between $Q(f)$ and $g(r)$, due to the limited distance range, must be taken into account.

6.3.1 Comparison

The only definite comparison between regions is obtained by looking at the observed $D(r, f)$ functionals, since this avoids subjective tradeoffs between Q and $g(r)$. A direct comparison between the $D(r, f)$ observed for the Apennines and the one observed in southern California has been done in Chapter 3, suggesting similar attenuation characteristics at low frequencies in the two regions, although more severe fall-offs characterize the spectral (and peak) amplitudes at high frequency ($f > 1$ Hz) for seismic waves traveling through the crust beneath the Apennines.

The same comparison has not been performed between the Apennines and Germany. However, by looking at the two sets of numbers used to match the observed attenuation functionals in the two regions, we see that the crustal propagation of seismic waves in Germany is much more efficient that along the Apennines.

6.3.2 Physical Interpretation

Even though the physical processes of anelastic attenuation in the Earth's crust are fairly well understood, simple quantitative relationships are not available to relate the value of the parameter $Q(f)$ to the complex phenomena that are responsible for the attenuation of seismic waves, and in particular to the geological characteristics of the region investigated. Thus, we can provide only a qualitative interpretation of the attenuation coefficients, $Q(f)$, in the two regions. The values found for the Apennines ($Q(f) = 130 f^{0.10}$) are typical for an active region, where we observe high attenuation at all frequencies. Germany, on the other hand, is a more sta-

ble region, characterized by a relatively old history of crustal deformation, and by a less severe crustal attenuation ($Q(f) = 400\,f^{0.42}$).

Attenuation processes are generally described by the relaxation model, where the viscous fluids (water and/or other volatiles) that permeate the cracks of the crustal rocks play the dominant role in dissipating the seismic energy. An important work on the relaxation model was the one by O'Connell and Budiansky (1977), which provided a representation of the broad-band attenuation behavior of a fluid-saturated cracked solid by means of the superposition of absorption peaks of individual relaxation mechanisms. The prototype of a fluid-saturated cracked solid tried to fit the idea, very fashionable in the 1970s, of a frequency-independent Q in the whole frequency band of seismic waves.

The relaxation model can also describe the anelastic attenuation observed in partially molten polycristalline aggregates, in which the melt is distributed as thin films along the grain boundaries. Other models of absorption in viscoelastic media were also developed, which require the superposition of absorption peaks of individual mechanisms (e.g. Liu et al., 1976, although they did not try to predict a constant Q over a very broad range of frequencies).

In more recent years, the picture given by O'Connell and Budiansky (1974, 1977) of an Earth permeated by cracks saturated with viscous fluids has been changed. We do not observe a constant Q over a broad range of frequencies, and evidence from deep borehole samples demonstrate that the presence of water in the lower crust is less abundant than what was thought before (Yardley and Valley, 1994). Nevertheless, the presence of volatiles percolating through the crust even in microscopic amounts is

enough to dramatically increase the attenuation of elastic waves. In most cases we can safely state that an abrupt change in the Q value in the crust is to be related to variations in the presence of fluids in the rocks. Thus, the different concentration of fluids in the crustal rocks (associated with variations in crack density and heat flow) is probably the reason for the strong differences in the attenuation parameter $Q(f)$ seen between the Apennines and Germany.

6.4 Final Considerations

Because of the nature of the data sets used in this study, individual S-wave arrivals cannot be isolated, and detailed crustal maps of Q cannot be determined from the observation of individual rays. Our goal was to provide the attenuation characteristics of the average shear-wave.

In this work we also demonstrated that the coda normalization technique yields very good estimates of the empirical attenuation functionals. In the past, the main problem with this technique was represented by its sensitivity to the presence of the numerous, large outliers that characterize the distribution of the reduced amplitudes in most cases. The problem has been solved in this study by implementing a more robust, L_1-norm minimization in the computer code that performs the coda normalization. This result is very important, since it tells us that even poorly calibrated recordings can contribute to the empirical definition of the ground motion scaling in a region. In one case only (the Apennines), the same L_1-minimization algorithm was successfully used to obtain an empirical estimate of the functional describing the duration of the ground shaking as a

function of frequency and hypocentral distance.

This study has demonstrated that the background seismicity of an active region can be used to predict ground motion spectra and peak values of ground motion, even for an earthquake of larger size ($M \sim 7$). We did so by comparing our prediction of the peak horizontal accelerations and velocities as a function of distance, with the empirical curves by Sabetta and Pugliese (1987).

For the Umbria-Marche seismic sequence of 1997, the comparison between the theoretical and the observed excitation terms showed an interesting fact: that is, it looks that the source scaling of the large 1997 events may differ from that of smaller events. We feel that all the issues raised by this work about the source characteristics in the Apennines deserve a dedicate effort for a proper reevaluation.

6.5 Future Developments

In future years, the results described in this dissertation will be used to obtain maps of the seismic hazard for Italy. The next step toward this accomplishment will be a thorough revision of the Italian catalog of instrumental seismicity, in the light of the results given in Chapter 3 about the estimation of the duration magnitudes. The integration of the information available on the regional attenuation relationships with the one available on the seismicity will produce the desired results.

Studies on the attenuation relationships in Sicily and in northern Italy (with a special attention to eastern Sicily and the eastern Alps) will be initiated shortly, since we expect to observe attenuation properties that are

different from the ones of the Apennines. The reevaluation of the high-frequency source parameters in the Apennines must be performed also, since our estimate of the crustal $Q(f)$ is very different from the one previously available. Similar source studies must be planned also in Germany.

The long list of future developments of this work, needed in the light of our results, makes this effort particularly valuable for the understanding of both the seismic source and the propagation phenomena along the Apennines and within the German region.

Appendix A - Probabilistic Seismic Hazard Analysis (PSHA)

We can summarize the procedure for a PSHA in the following four steps (from Kramer, 1996):

- i) locate and characterize the earthquake sources;

- ii) characterize the magnitude-time distribution of the seismicity;

- iii) use the predictive relationships to determine the ground motion produced at a specific site by an earthquake of a given magnitude occurred at a given location;

- iv) associate the proper uncertainties to locations, magnitudes and other parameters; compute the probability of having a certain threshold of ground motion exceeded within a given time window.

Step i) requires the definition of the spatial probability distribution $f_R(r)$ of earthquakes in each seismogenic area. Step ii) requires, for each seismogenic zone, the estimate of the maximum expected magnitude and of the coefficients in the Gutenberg-Richter relationship. If the characteristic earthquake model is to be applied, additional information on the maximum magnitude and the corresponding recurrence time is needed.

If λ_m is defined as the mean annual rate of exceedance of the magnitude threshold m then

$$\lambda_m = 10^{a-bm} = \exp(\alpha - \beta m)$$

where $\alpha = 2.303a$, $\beta = 2.303b$. If we are interested only in earthquakes of magnitude larger than a minimum threshold m_0 of engineering interest then

$$\lambda_m = \exp\left[\alpha - \beta m + \beta m_0 - \beta m_0\right]$$

$$= \exp\left[\alpha - \beta m_0\right]\exp\left[-\beta(m - m_0)\right]$$

$$= \nu \exp\left[-\beta(m - m_0)\right]$$

and

$$\nu = \exp\left[\alpha - \beta m_0\right].$$

The cumulative probability distribution is

$$F_M(m) = P\left[M < m | M > m_0\right] = \frac{\lambda_{m_0} - \lambda_m}{\lambda_{m_0}}$$

$$F_M(m) = 1 - \exp\left[-\beta(m - m_0)\right]$$

then the probability distribution function will be

$$f_M(m) = \frac{d}{dm}F_M(m)$$

$$f_M(m) = \beta \exp\left[-\beta(m - m_0)\right]$$

To obtain $F_M(m)$, we just write the number of events *per annum* with magnitude M such that

$$m_0 < M < m$$

and normalize it by the number of events exceeding m_0.

If we can associate a maximum magnitude to the earthquakes occurring in a specific seismogenic zone, we can write the rate of excedance for earthquakes with magnitudes M such that $m_0 < M < m_{max}$:

$$\lambda_{m_{bounded}} = \nu \frac{\exp\left[-\beta(m - m_0)\right] - \exp\left[-\beta(m_{max} - m_0)\right]}{1 - \exp\left[-\beta(m_{max} - m_0)\right]}$$

Again

$$F_M(m) = P\left[M > m | m_0 < m < m_{max}\right] =$$

$$= \nu \frac{\lambda_{m_{0bounded}} - \lambda_{m_{bounded}}}{\lambda_{m_{0bounded}}} = \nu \frac{1 - \exp\left[-\beta(m - m_0)\right]}{1 - \exp\left[-\beta(m_{max} - m_0)\right]}$$

The "$_{bounded}$" subscript means that the integration is performed from m_0 up to m_{max}, instead of from $m = 0$ to $m = \infty$.

Proceeding with step iii), we now want to write the probability *per annum* that a ground motion threshold would be exceeded (for example 0.1 g for the ground acceleration). In the following formulas, "A" will represent the observed quantity, and "a" the threshold:

$$P\left[A > a\right] = \int_r \int_m P\left[A > a | m, r\right] f_M(m) f_R(r) dm dr$$

From the predictive relationship:

$$\ln\left[A(M|R)\right] = C_1 + C_2 M - C_3 \ln(R + R_0) - C_4(R + R_0) + \epsilon.$$

If the ground motion prediction error $\epsilon = 0$, then $A > a$ if

$$m > m_0$$

where
$$m_0 = \frac{\ln a - C_1 + C_3 \ln(R + R_0) + C_4(R + R_0)}{C_2}$$

and

$$P\left[A > a\right] = \int_r \int_{m_0}^{m_{max}} \nu P\left[A > a | m, r\right] \beta \exp\left[-\beta(m - m_0)\right] f_R(r) dm dr.$$

Appendix B - Deterministic Seismic Hazard Analysis (DSHA)

A Deterministic Seismic Hazard Analysis can be summarized by steps i) and iii) from the previous paragraph, with the difference that the characterization of the seismogenic zone will be done in terms of the maximum expected magnitude and minimum distance from the site of interest.

Given the maximum expected magnitude for each seismogenic area capable of affecting our site, we will proceed in our DSHA by using the regional predictive relationships. The analysis will give an estimate of the largest peak ground motion expected for each site in the region. If more than one seismogenic area is active in the region, step i) and ii) will be repeated by using a calibrated set of parameters for each area. In the frequency band of engineering interest, the DSHA will give the highest estimate of maximum expected peak ground motion.

The deterministic approach gives the most conservative estimate of seismic hazard, since it does not take into account the specific likelihood of occurrence of the earthquake, but only the maximum magnitude expected in each seismogenic zone. It seems reasonable to perform a DSHA before designing nuclear power plants, or other dangerous structures. On the other hand, it is not economical to use DSHA's to define or update residential building codes.

Appendix C - Source Fourier Amplitude Spectra

A possible way to estimate the characteristics of the seismic Fourier amplitude spectra at a certain distance from the source is by performing a regression on a large set of strong-motion recordings (Trifunac, 1976; McGuire et al., 1984; Trifunac and Lee, 1987; Castro et al., 1990). Another way of predicting the S-waves amplitude spectra makes use of the Brune's (1970; 1971) theoretical spectrum generated by the instantaneous slip of a circular fracture. Using this tool, McGuire and Hanks (1980), Boore (1983) and others have defined the source Fourier amplitude spectra

$$|A(f)| = \left[CM_0 \frac{f^2}{1 + (f/f_c)^2} \right].$$

In order to account for the anelastic loss of energy due to the combined effects of the crustal propagation and of the increase of anelastic dissipation at shallow depth, we multiply the Brune spectrum by

$$g(r) \exp\left(-\pi \kappa_0 f\right) \exp\left(-\frac{\pi f r}{Q(f) v_s}\right)$$

The first high-frequency exponential term is independent of the source-receiver hypocentral distance, and reflects the attenuation experienced by the seismic waves immediately below the recording sites, due to the presence of weathered rocks or loose sediments. The second exponential term accounts for the attenuation experienced by the seismic waves travelling through the crust. $g(r)$ is the geometrical spreading; for body-waves is

expressed by

$$g(r) = \frac{1}{r}.$$

A different way to describe the high-frequency attenuation induced by the shallow geology is obtained by substituting the term $\exp(-\pi \kappa_0 f)$ in the equation above, by the f_{max} filter:

$$\left[\frac{1}{\sqrt{1 + (f/f_{max})^8}} \right].$$

Both f_{max} or κ_0 are to be estimated regionally; the former was introduced by Hanks (1982), and the latter by Anderson and Hough (1984). Boore and Joyner (1997) multiplied the Brune spectrum by a general amplification factor, $V(f)$, related to the variation in seismic impedance at shallow depths.

The constant C in the equation above is defined as

$$C = \frac{R_{\theta\phi}FV}{4\pi \rho v_s^3}$$

where $R_{\theta\phi}$ accounts for the radiation pattern (average value = 0.55); F is the free-surface term (vertically incident S-waves: $F = 2$), and V represents the energy partition in the two horizontal components ($V = \sqrt{2}/2$). The corner frequency in the Brune spectral model can be written as

$$f_c = 4.9 \times 10^6 v_s \left(\frac{\Delta\sigma}{M_0} \right)^{1/3}$$

where v_s is the shear-wave velocity in km/s; M_0 is the scalar moment in dyne-cm, and $\Delta\sigma$ is the stress parameter (stress-drop) in bars. $\Delta\sigma$ represents the difference in shear stress on the fault surface immediately before and after the earthquake. Stress parameters of 50 and 100 bars are used, respectively, for the western and the eastern US (Kramer, 1996). Rovelli

et al. (1988) suggested a value of 200 bars for the average stress parame-
ter along the Apennines, although they observe a large variability of this
parameter throughout the region.

The model used in this study to produce the earthquake spectral am-
plitudes in the studied regions is the one proposed by Boore and Joyner
(1997) for Southern California. This spectral model is characterized by the
parameters

$$\Delta\sigma = 70 \text{ bar}$$

$$\kappa_0 = 0.04 \text{ s}$$

In all our computations, the parameter κ_0 was varied in order to match the
observed excitation spectra in the investigated regions. The other param-
eters of the described spectral model were left unchanged.

References

Aki, K. (1980). Attenuation of shear waves in the lithosphere for frequencies from 0.05 to 25 Hz, *Phys. Earth Planet. Inter.*, 21, 50-60.

Aki, K., and B. Chouet (1975). Origin of the coda waves: source, attenuation and scattering effects, *J. Geophys. Res.*, 80, 3322-3342.

Amato, A., R. Azzara, A. Basili, C. Chiarabba, G.B. Cimini, M. Di Bona and G. Selvaggi (1994a). GeoModAp: a teleseismic transect across the Northern Apennines (Italy), *EOS 1994 Fall meeting*, S01-48.

Amato, A., R. Azzara, A. Basili, C. Chiarabba, G.B. Cimini, M. Di Bona, L. Margheriti, C. Nostro and G. Selvaggi (1994b). The Northern Apennines Teleseismic Transect (1994), *Istituto Nazionale di Geofisica*, technical report.

Amato, A., R. Azzara, A. Basili, C. Chiarabba, G.B. Cimini, M. Di Bona, F.P. Lucente, L. Margheriti, C. Nostro, G. Selvaggi, (1995a). The Central Apennines Teleseismic Transect (1995), *Istituto Nazionale di Geofisica*, technical report.

Amato, A., C. Chiarabba, G.B. Cimini, M. Di Bona, L. Margheriti, C. Nostro and G. Selvagi (1995b). Deep structure beneath the Northern Apennines (Italy) from passive seismological studies. *IUGG XXI Assembly*, July 2-14, 1995.

Amato, A., L. Margheriti, R. Azzara, A. Basili, C. Chiarabba, M.G. Ciaccio, G.B. Cimini, M. Di Bona, A. Frepoli, F.P. Lucente, , C. Nostro and G. Selvaggi (1998a). Passive seismology and deep structure in central Italy, *Pure appl. geophys.*, 151, 479-493.

Amato, A., R. Azzara, C. Chiarabba, G.B. Cimini, M. Cocco, M. Di Bona, L. Margheriti, S. Mazza, F. Mele, G. Selvaggi, A. Basili, E. Boschi, F. Courboulex, A. Deschamps, S. Gaffet, G. Bittarelli, L. Chiaraluce, D. Piccinini and M. Ripepe (1998b). The 1997 Umbria-Marche, Italy, earthquake sequence: a first look at the main shocks and aftershocks, *Geophys. Res. Lett.*, 25, 2861-2864.

Anderson, J.G. and S.E. Hough (1984). A model for the shape of the Fourier amplitude spectrum of acceleration at high frequencies, *Bull. Seism. Soc. Am.*, 74, 1969-1993.

Anderson, H. and J. Jackson (1987). Active tectonics of the Adriatic region, *Geophys. J. R. Astr. Soc.*, 91, 613-637.

Atkinson, G.M. (1993). Earthquake source spectra and attenuation in southeastern Canada, *University of Western Ontario, London, Ontario*, Ph.D. thesis.

Atkinson, G.M. and D.M. Boore (1995). Ground-motion relations for eastern North America, *Bull. Seism. Soc. Am.*, 85, 17-30.

Atkinson, G.M. and D.M. Boore (1998). Evaluation of models for earthquake source spectra in Eastern North America, *Bull. Seism. Soc. Am.*, 88, 917-934.

Atkinson, G.M. and Silva (1997). An empirical study on earthquake source spectra, *Bull. Seism. Soc. Am.*, 87, 97-113.

Bard, P.-Y. and M. Bouchon (1985). The two-dimensional resonance of sediment-filled valleys, *Bull. Seism. Soc. Am.*, 75, 519-541.

Bartels, R.H. and A.R. Conn (1980). Overdetermined systems of linear equations in the L1 sense, with or without linear constraints, *ACM TOMS*, 6, 609-614.

Beresnev, I., E.K. Field, K. Van Den Abeele and P.A. Johnson (1988). Magnitude of nonlinear sediment response in Los Angeles Basin during the 1994 Northridge, California, earthquake, *Bull. Seism. Soc. Am.*, 88, 1079-1084.

Bisztricsany, E. (1958). A new method for the determination of the magnitude of earthquakes, *Geofiz. Kozlemen*, 7, 69-96.

Boore, D.M. (1983). Stochastic simulation of high-frequency ground motion based on seismological models of the radiated spectra, *Bull. Seism. Soc. Am.*, 73, 1865-1894.

Boore, D.M. (1986). Short-period P- and S-wave radiation from large earthquakes: implication for spectral scaling relations, *Bull. Seism. Soc. Am.*, 76, 43-64.

Boore, D.M. and W.B. Joyner (1997). Site amplification for generic rock sites, *Bull. Seism. Soc. Am.*, 87, 327-341.

Boore, D.M., Joyner, W.B. and T.E. Fumal (1993). Estimation of response spectra and peak acceleration from western North America earthquakes: An interim report, *Open-file report 93-509, U.S. Geological Survey, Reston, Virginia*, 72 pp.

Borcherdt, R.D. (1970). Effects of local geology on ground motion near San Francisco Bay, *Bull. Seism. Soc. Am.*, 60, 29-61.

Boschi, E., A. Caserta, C. Conti, M. Di Bona, R. Funiciello, L. Malagnini, F. Marra, G. Martines, A. Rovelli and S. Salvi (1995). Resonance of subsurface sediments: an unforeseen complication for designers of roman columns, *Bull. Seism. Soc. Am.* 85, 320-324.

Brune, J.N. (1970). Tectonic stress and the spectra of seismic shear waves from earthquakes, *J. Geophys. Res.*, 75, 4997-5009.

Brune, J.N. (1971). Correction, *J. Geophys. Res.*, 76, 5002.

Building Seismic Safety Council (BSSC) (1994). NEHRP recommended provisions for seismic regulations for new buildings, Part 1 - Provisions, FEMA 222A, Federal Emergency Management Agency, 290 pp.

Campbell, K.W. and Y. Bozorgnia (1994). Near-source attenuation of peak horizontal acceleration from worldwide accelerograms recorded from 1957 to 1993, *Proceedings of the Fifth U.S. National Conference on Earthquake Engineering, E.E.R.I., Berkeley, California*, Vol. 1, 283-292.

Cartwright, D.E. and M.S. Longuet-Higgins (1956). The statistical distribution of the maxima of a random function, *Proc. Roy. Soc. London*, Ser. A237, 212-232.

Castro, R.R., J.G. Anderson and S.K. Singh (1990). Site response, attenuation and source spectra of S-waves along the Guerrero, Mexico, subduction zone, *Bull. Seism. Soc. Am.*, 80, 1489-1523.

Castro, R.R., M. Mucciarelli, G. Monachesi, F. Pacor and R. Berardi (1999). A review of nonparametric attenuation functions computed for different regions of Italy, *Annali di Geofisica*, in press.

Console, R., B. De Simoni and A. Di Sanza (1988). Riesame della relazione magnitudo-durata, *Atti del 7° Convegno Annuale del Gruppo Nazionale di Geofisica della Terra Solida, Roma, November 30 - December 2, 1988*, 51 - 62.

Crosson, R.S. (1972). Small earthquakes, structure, and tectonics of the Puget Sound region, *Bull. Seism. Soc. Am.*, 62, 1133-1171.

Deichmann, N. and J. Ansorge (1983). Evidence for lamination in the lower continental crust beneath the Black Forest (Southwestern Germany), *J. Geophys.*, 52, 109-118.

Del Pezzo, E., A. Rovelli and G. Zonno (1985). Seismic Q and site effects on local earthquakes in the Ancona region (Central Italy), *Ann. Geophys.*, 3, 629-636.

Edel, J.B., K. Fuchs, C. Gelbke and C. Prodehl (1975). Deep structure of the southern Rhinegraben area from seismic refraction investigations, *J. Geophys.*, 41, 333-353.

Ekström, G., A. Morelli, E. Boschi and A. Dziewonski (1998). Moment tensor analysis of the Central Italy earthquake sequence of September-October 1997, *Geophys. Res. Lett.*, 25, 1971-1974.

Frankel, A., A. McGarr, J. Bicknell, J. Mori, L. Seeber and E. Cranswick (1990). Attenuation of high-frequency shear waves in the crust: measurements from New York state, South Africa, and Southern California, *J. Geophys. Res.*, 95, 17441-17457.

Gajewski, D. and C. Prodehl (1987). Seismic refraction investigation of the Black Forest, *Tectonophysics*, 142, 27-48.

Geiss, E. (1987). A new compilation of crustal thickness in the Mediterranean area, *Ann. Geophys.*, 5B(6), 623-630.

Giardini, D., M. di Donato and E. Boschi (1997). Calibration of magnitude scales for earthquakes of the Mediterranean, *J. of Seismology*, 1, 161-180.

Gutenberg, B. (1957). Effects of ground on earthquake motion, *Bull. Seism. Soc. Am.*, 47, 221-250.

Hanka, W. (1991). The German Regional Broad-Band Seismic Network (GRN) project, in: Boschi, E, D.Giardini, A.Morelli (eds.): *I. Workshop on MedNet: The broad-band seismic network for the Mediterranean, Il Cigno Galileo Galilei*, CCSEM, Erice, Sep. 10-14, 1990, 83-95.

Hanks, T.C. (1982). f_{max}, *Bull. Seism. Soc. Am.*, 72, 1867-1879.

Hanks, T.C. and H. Kanamori (1979). A moment magnitude scale, *J. Geophys. Res.*, 84, 2348-2350.

Harjes, H.-P. and D.Seidl (1978). Digital recording and analysis of broadband seismic data at the Gräfenberg (GRF)-array, *J. Geophys.*, 44, 511-521.

Harjes, H.-P. (1990). Design and siting of a new regional array in Central Europe, *Bull. Seism. Soc. Am.*, 80, 1801-1817.

Herrmann, R.B. (1975). The use of duration as a measure of seismic moment and magnitude, *Bull. Seism. Soc. Am.*, 65, 899-913.

Hoshiba, M. (1991). Simulation of multiple-scattered coda wave excitation based on the energy conservation law, *Phys. Earth Planet. Inter.*, 67, 123-136.

Idriss, I.M. and H.B. Seed (1968). An analysis of ground motion during the 1957 San Fransisco earthquake, *Bull. Seism. Soc. Am.*, 58, 2013-2032.

Johnson, L.R. and W. Silva (1981). The effects of unconsolidated sediments upon the ground motion during local earthquakes, *Bull. Seism. Soc. Am.*, 71, 127-142.

Joyner, W.B., and A.T.F. Chen (1975). Calculation of nonlinear ground response in earthquakes, *Bull. Seism. Soc. Am.*, 65, 1315-1336.

Kanai, K. (1952). Relation between the nature of surface layer and the amplitude of earthquake motions, *Bull. Earthquake Res. Inst.*, Tokyo Univ., 30, 31-37.

Kramer, S.L. (1996). Geotechnical earthquake engineering, *Prentice Hall*, Upper Saddle River, NJ 07458, 653.

Lawson, C.L. and R.J. Hanson (1974). Solving Least Squares Problems, *Prentice-Hall, Inc.*, Englewood Cliffs, N.J..

Lay, T. and T.C. Wallace (1995). Modern global seismology, *Vol. 58 of the INTERNATIONAL GEOPHYSICS SERIES, Academic Press*, 521 pp.

Lee, W.H.K., R.E. Bennet and K.L. Meagher (1972). A method of estimating magnitude of local earthquakes from signal duration, *U.S. Geological Survey Open File Report*.

Liu, H.P., D. Anderson and H. Kanamori (1976). Velocity dispersion due to anelasticity ; implications for seismology and mantle composition, *Geophys. J. R.A.S.*, 47, 41-58.

Lüschen, E., F. Wenzel, K.,-J. Sandmeier, D. Menges, Th. Rühl, M. Stiller, W. Janoth, F. Keller, W. Söllner, R. Thomas, A. Krohe, R. Stenger, K. Fuchs, H. Wilhelm and G. Eisbacher (1987). Near-vertical and wide-angle seismic surveys in the Black Forest, SW Germany, *J. Geophys.*, 62, 1-30.

Malagnini, L. (1996). Velocity and attenuation structure of very shallow soils: evidences for a frequency-dependent Q, *Bull. Seism. Soc. Am.*, 86, 1471-1486.

Malagnini, L., R.B. Herrmann, G. Biella and R. de Franco (1995). Rayleigh waves in Quaternary alluvium from explosive sources: determination of shear-wave velocity and Q structure, *Bull. Seism. Soc. Am.*, 85 900-922.

Malagnini, L., R.B. Herrmann, A. Mercuri, S.Opice, G. Biella and R. de Franco (1997). Shear-wave velocity structure of sediments from the inversion of explosion-induced Rayleigh waves: comparison with cross-hole measurements, *Bull. Seism. Soc. Am.*, 87, 1413-1421.

McGuire, R.M. and Hanks, T.C. (1980). RMS acceleration and spectral amplitudes of strong ground motion during the San Fernando, California earthquake, *Bull. Seism. Soc. Am.*, 70, 1907-1919.

McGuire, R.K., A.M. Becker and N.C. Donovan (1984). Spectral estimates of seismic shear waves, *Bull. Seism. Soc. Am.*, 74, 1427-1440.

Meissner, R., Th. Wever and R. Flüh (1987). The Moho in Europe - Implications for crustal development, *Ann. Geophys.*, 5B, 356-364.

Moczo, P. and P.-Y. Bard (1993). Wave diffraction, amplification and differential motion near strong lateral discontinuities, *Bull. Seism. Soc. Am.*, 83, 85-106.

Mueller, St., E. Petterschmitt, K. Fuchs and J. Ansorge (1969). Crustal structure beneath the Rhinegraben from seismic refraction and reflection measurements, *Tectonophysics*, 8, 529-542.

Mueller, St., E. Petterschmitt, K. Fuchs, D. Emter and J. Ansorge (1973). Crustal structure of the Rhinegraben area. In: St. Mueller (Editor), Crustal structure based on seismic data, *Tectonophysics*, 20, 381-392.

Newmann, A., S. Stein, J. Weber, J. Engeln, A. Mao and T. Dixon (1999). Slow deformation and lower hazard at the New Madrid seismic zone, *Nature*, 284, 619-621.

O'Connell, R.J. and B. Budiansky (1974). Seismic velocities in dry and saturated cracked solids, *J. Geophys. Res.*, 79, 5412-5426.

Plenefisch, T., S. Faber and K.-P. Bonjer (1994). Investigations of S_n and P_n phases in the area of the upper Rhine Graben and northern Switzerland, *Geophys. J.*, 119, 402-420.

O'Connell, R.J. and B. Budiansky (1977). Viscoelastic properties of fluid-saturated cracked solids, *J. Geophys. Res.*, 82, 5719-5735.

Raoof, M., R.B. Herrmann and L. Malagnini (1999). Attenuation and excitation of three-component ground motion in Southern California, *Bull. Seism. Soc. Am.*, in press.

Real, C.R. and T. Teng (1973). Local Richter magnitude and total signal duration in southern California, *Bull. Seism. Soc. Am.*, 63, 1809-1827.

Rogers, A. M., J. C. Tinsley and R. D. Borcherdt (1985). Predicting relative ground response, *U.S. Geol. Surv. Prof. Paper 1360*, 221-248.

Russell, D.R. (1987). Multichannel processing of dispersed surface waves, *Ph.D. dissertation*, Saint Louis University.

Rovelli, A., O. Bonamassa, M. Cocco, M. Di Bona and S. Mazza (1988). Scaling laws and spectral parameters of the ground motion in active extensional areas in Italy, *Bull. Seism. Soc. Am.*, 78, 530-560.

Sabetta, F. and A. Pugliese (1987). Attenuation of peak horizontal acceleration and velocity from Italian strong-motion records, *Bull. Seism. Soc. Am.*, 77, 1491-1511.

Sabetta, F. and A. Pugliese (1996). Estimation of response spectra and simulation of nonstationary earthquake ground motion, *Bull. Seism. Soc. Am.*, 86, 337-352.

Sanchez-Sesma, F. (1985). Diffraction of elastic SH-waves by wedges, *Bull. Seism. Soc. Am.*, 75, 1435-1446.

Seed, H.B. and I.M. Idriss (1969). Influence of soil conditions on ground motion during earthquakes, *Proc. ASCE*, 95(SM1), 99-137.

Selvaggi, G. and A. Amato (1992). Subcrustal earthquakes in the northern Apennines (Italy): evidence for a still active subduction?, *Geophys. Res. Lett.*, 19, 2127-2130.

Shin, T.-C. and R.B. Herrmann (1987). L_g attenuation studies using the 1982 Miramichi data, *Bull. Seism. Soc. Am.*, 77, 384-397.

Silva, W.J. and R.B. Darragh (1995). Engineering characterization of strong ground motion recorded at rock sites, *Electric Power Research Institute*, Palo Alto California, Report No. TR-102262.

Sole'vev, S.L. (1965). Seismicity of Sakalin, *Bull. Earthquake Res. Inst., Tokyo Univ.*, 43, 95-102.

Steidl, J.H., A.G. Tumarkin and R.J. Archuleta (1996). What is a reference site? *Bull. Seism. Soc. Am.*, 86, 1733-1748.

Trifunac, M.D. (1976). Preliminary empirical model for scaling Fourier amplitude spectra of strong ground motion acceleration in terms of earthquake magnitude, source-to-station distance, and recording site conditions, *Bull. Seism. Soc. Am.*, 66, 1343-1373.

Trifunac, M.D. and A.G. Brady (1975). On the correlation of seismic intensities with the peaks of recorded strong ground motion, *Bull. Seism. Soc. Am.*, 65, 139-162.

Trifunac, M.D. and A.G. Brady (1976). Correlation of peak acceleration, velocity and displacement with earthquake magnitude, distance and site conditions, *Earthquake Eng. Struct. Dynamics*, 4, 455-471.

Trifunac, M.D. and V.W. Lee (1987). Frequency dependent attenuation of strong earthquake ground motion, in: *Selection of Earthquake-Resistant Design Criteria for Nuclear Power Plants: Methodology and Technical cases*, Report NUREG/CR-4903, Vol. 1, Nuclear Regulatory Commission, Washington D.C..

Tsumura, K. (1967). Determination of earthquake magnitude from total duration of oscillation, *Bull. Earthquake Res. Inst., Tokyo Univ.*, 15, 7-18.

Wever, T.H., R. Meissner, P. Sadowiak and the DEKORP Group (1990). *Tectonophysics*, 176, 87-101.

Wood, H.O. (1908). Distribution of apparent intensity in San Francisco, in *The California Earthquake of April 18, 1906, Report of the State Earthquake Investigation Commission*, Carnegie Inst. Wash., Publ. 87, Washington, D.C., 220-245.

Wu, R.-S. (1985). Multiple scattering and energy transfer of seismic waves - separation of scattering effect from intrinsic attenuation - I. Theoretical modeling, *Geophys. J. R. astr. Soc.*, 82, 57-80.

Yardley, B.W.D. and J.W. Valley (1994). Geochemistry; how wet is the Earth's crust?, *Nature*, 371 (6494), 205-206.

Yazd, M.R.S. (1993). Ground motion studies in the Southern Great Basin of Nevada and California, *Saint Louis University*, Ph.D. thesis.

Zeis, St., D. Gajewski and C. Prodehl (1990). Crustal structure of southern Germany from seismic refraction data, *Tectonophysics*, 176, 59-86.

Zucca, J.J. (1984). The crustal structure of the southern Rhinegraben from re-interpretation of seismic refraction data, *J. Geophys.*, 55, 13-22.

Vita Auctoris

Luca Malagnini was born in Verona (Italy) on 16 May 1961. He moved to Rome in 1971, where he enrolled in the Physics program of the "Università di Roma, La Sapienza" in the summer of 1980.

During his academic career he approached different branches of Physics before deciding that he was fascinated the most by seismology. He was also distracted by two other major interests: music and sport. He studied the flute for many years, and was an active kayaker at an old-fashioned rowing club in Rome. He was awarded the title of "Dottore in Fisica" in 1988. During his defense, his mother was asked to leave the room by the chair of the Department because she could not help talking all the time. His advisor, Prof. Renato Funiciello, forgot he had to show up that day. Another member of his committee, Dr. Antonio Rovelli, had left for a long weekend in Gargano. The only member who was present was Prof. Carlo Bernardini, a theoretical physicist who was in the committee only because of some rules of the University. He had no clue what Malagnini's thesis was about, and he barely knew his face. The Candidate, however, made it through the unfortunate situation.

He soon after started working for free at the "Istituto Nazionale di Geofisica" of Rome (ING) on a number of projects. During those years, his only income was provided by the kayak team he belonged to and coached.

On January 1, 1990, Malagnini was hired by ING. He worked at Columbia University as a visiting scholar in the winter of 1991. In 1992, he started his

collaboration with Prof. Robert B. Herrmann on various topics. Since August 1996, he has been pursuing his Doctor of Philosophy in Geophysics at Saint Louis University.

His career as an athlete started in 1974, with the kayak team of the "Circolo Canottieri Aniene," in Rome. He struggled at a low or mediocre level until the summer of 1981, when he unexpectedly got his first national title, in the K2 10,000 meters. After that fortunate event, he won a number of other competitions on the marathon, half-marathon, 10K, and speed distances. In recent years he was still trying to compete: in 1995, with the training of an amateur and a lot of pain, he reached the finals in all the solo (K1) and double (K2) speed competitions at the Nationals, finishing 4th in the K2 500 meters. His career abruptly ended in the summer of 1997, when, with his friend, psychiatrist and former Olympian, Massimo Moriconi, he participated to a painful race for over-35 on the K2 20-km, and finished last.

Malagnini is a member of the Seismological Society of America and of the American Geophysical Union.